Energy transfer to dopant molecules in polyfluorene films

Lyons, Benjamin Paul

Benjamin Paul Lyons
Energy transfer to dopant molecules in polyfluorene films

ABSTRACT

Polyfluorene is a promising material for applications such as polymeric light-emitting diodes. Upon optical or electrical excitation it exhibits efficient blue fluorescence and is easily made into thin films by spin-coating from solution. Incorporating suitable dopant molecules in these films changes the emission colour. The energy transfer processes taking place have been investigated here by steady-state and time resolved fluorescence measurements.

To assist in the analysis of these measurements, the optical constants of polyfluorene were found by ellipsometry. Both unaligned and aligned films exhibit uniaxial anisotropy. Unaligned films have their optical axis normal to the film surface and are optically negative. Aligned films have their optical axis oriented in plane, parallel to the rubbing direction and are optically positive. In aligned films, light polarized in the alignment direction experiences absorption twice as high as light incident on unaligned films.

Temperature dependent steady-state measurements were made on polyfluorene films doped with tetraphenyl porphyrin. Energy transfer in such systems is usually described in terms of Förster transfer but it is shown here that exciton migration must also occur. A new model is developed to include this process. Diffusion lengths of 11 +/- 2 nm at low temperature and 20 +/- 2 nm at room temperature are found.

Energy transfer was also investigated by fluorescence polarization anisotropy. It is shown that even at low temperature, excitons migrate far enough to depolarize the fluorescence. However, the emission is not completely depolarized and it is suggested that some excitons are trapped immediately after excitation.

Polarized luminescence from dicyanomethylene in aligned polyfluorene films is observed. These molecules align themselves at least partially with the polymer chains. Although the polarization ratio not sufficient for use in a device, this is a viable method of achieving polarized fluorescence with a range of colours.

Energy transfer to dopant molecules in polyfluorene films

Benjamin Paul Lyons

Submitted to the Faculty of Science, University of Durham,
for the degree of Doctor of Philosophy

Department of Physics
University of Durham

August 2005

DECLARATION

Except where specific reference is made, all material in this dissertation is the result of my own work. This dissertation has not been submitted in whole or in part for the award of a higher degree at this or any other university.

ACKNOWLEDGEMENTS

I have been very fortunate to have had such a great supervisor, Professor Andy Monkman. His enthusiasm and advice have encouraged me enormously throughout my PhD and I am very grateful to him for always finding the time to discuss my work.

Many thanks go to all the members of the OEM research group past and present, for their advice and help with polymer-related things, and company during tea-breaks and adventures overseas.

Much of this work required new components being built and old ones being fixed. I would like to thank everyone in the mechanical and electronics workshop for their expertise, and for putting up with me and the strange designs I had them build. Thanks also must go to the condensed matter group's technicians, Norman and Davy, who somehow always manage to get things to work.

I am very grateful to Sony Europe Plc for providing me with a CASE Studentship. I visited their labs in Stuttgart on two occasions, and I would particularly like to thank Tzenka Miteva for all her assistance while I was there.

I would like to thank my parents Ray and Anita, my brother Tom and my sister Sophie. Many thanks also to my friends in Durham, with whom I have enjoyed many parties, games of pool and other distractions from physics. Thanks too to my friends in the rest of the country and the rest of the world, for the times when I needed a break from Durham. Finally, I would like to thank Hsin-yu Chang, for all her support and encouragement over the last few years.

Contents

List of Figures

Chapter 1: Introduction

1.1 Introduction

Traditional polymers play a huge role in everyday life. They are cheap, versatile materials, with properties such as low density, flexibility, mechanical strength, ease of fabrication and high resistivity which have found places for them in almost every aspect of consumer society. In the field of electronics, polymers have so far only been useful for their insulating properties. However, it has long been realised that a material combining the low cost and versatility of polymers with the properties of metals and semi-conductors would create a exciting new range of possibilities.

Several discoveries towards the end of the twentieth century brought these possibilities closer to reality. In 1977, it was discovered that polyacetylene exhibited metallic conductivities upon doping with sodium.[1] In 1990, Friend's group in Cambridge reported electroluminescence from devices made of a film of poly(p-phenylenevinylene) between metallic electrodes.[2] These materials are both examples of *conjugated polymers.* These polymers have alternating single and double bonds, creating delocalised excitations which are responsible for their conducting and semi-conducting properties. Progress in this field has proceeded at a remarkable rate. A huge variety of materials has now been synthesized and characterized, the physics of these materials has been intensely investigated experimentally, theoretically and computationally and they have found their way into many applications. These include polymer light-emitting diodes,[3-14] organic solar cells[15-25] and polymer transistors.[26-30] Electrically pumped solid-state lasers have also been proposed.[31-34] Organic materials have possibilities that are not available for inorganic semi-conductors such as silicon, one of the most exciting being that of flexible displays.

A particularly promising conjugated polymer is polyfluorene, an efficient blue-emitting material. A great deal of research has been done into its electronic and physical properties. This includes its use in polymer LEDs[11,35-38] and solar cells,[16-

[18,22,24] orientation of films,[11,39-46] phase morphology[43,47,48] and the behaviour of its excited states.[49-52]

This thesis focuses on fundamental properties of polyfluorene which will be important in optimizing its applications. Its overall theme is the energy transfer and migration of the exciton pseudo-particles responsible for the luminescence. Over the course of these investigations, the optical constants of polyfluorene films, which determine the passage of light through the material, were also measured. The knowledge of these was thought necessary for the proper analysis of the energy transfer results, though their use extends well beyond that.

This thesis is divided into six chapters. This first chapter provides background information on conjugated polymers and optical processes, as well as a review of the physical properties and applications of these materials. Chapter 2 summarises basic methods and materials used throughout this work. Chapter 3 describes measurements made to determine the optical constants of aligned and unaligned polyfluorene films. Chapter 4 describes energy transfer to dopant molecules in polyfluorene films and the influence of exciton migration. Chapter 5 describes further measurements on energy transfer via fluorescence polarization experiments. Chapter 6 contains the conclusions.

1.2 Background

This background is intended to help the reader to understand this thesis and put this work into context. Firstly, conjugated polymers are introduced. Their structure is described in terms of the linear combination of atomic orbitals model, the selection rules regarding electronic transitions are given. This is followed by a section on photophysics, describing the important processes of absorption and luminescence and the factors governing their spectra. The nature of the photoexcitations in conjugated polymers is then discussed. The focus is on the generally accepted exciton model and how this relates to the photophysics of these materials. Applications of conjugated polymers in general, specifically light-emitting diodes and solar cells, are then described. Finally, an introduction to the properties of polyfluorene is given. This includes its basic electronic and photophysical properties, as well as discussions on its use in applications, alignment properties and defect emission.

1.2.1 *Conjugated polymers*

A conjugated polymer is a polymer consisting of a planar or near-planar sequence of alternating single and double bonds along its backbone. This results in the highly delocalised electronic states responsible for their interesting properties.

Bonding in conjugated polymers can be described by the linear combination of atomic orbitals (LCAO).[53] This is a transformation of the atomic basis states, which involves constructing new hybrid states from linear combinations of s, p states on the same atom. These states are written:

$$h_i = N\left(s + \lambda p_i\right) \tag{1.1}$$

where N is the normalisation constant $\left(1+\lambda^2\right)^{-1/2}$. The hybrid states may be constructed such that:

$$\left\langle h_i \middle| h_j \right\rangle = 0; \quad i \neq j \tag{1.2}$$

The p orbital itself is a normalised linear combination of p_x, p_y and p_z orbitals.

The three principal types of s-p hybridization are labelled according to the number of p orbitals mixed with the s orbital. The most relevant type here is sp^2 hybridization, where an s orbital is mixed with two p orbitals, leaving the third p orbital unchanged. Three equivalent hybrid states are formed, lying at 120° to each other in a plane. If we take this to be the x-y plane then the new states are:

$$\begin{aligned} h_1 &= \left(s + 2^{1/2} p_x\right)/3^{1/2} \\ h_2 &= \left(s - \frac{p_x}{2^{1/2}} + \frac{3^{1/2} p_y}{2^{1/2}}\right)\Big/3^{1/2} \\ h_3 &= \left(s - \frac{p_x}{2^{1/2}} - \frac{3^{1/2} p_y}{2^{1/2}}\right)\Big/3^{1/2} \end{aligned} \tag{1.3}$$

Figure 1.1 shows the formation of an sp hybrid and the three possible sp^2 hybrid states.

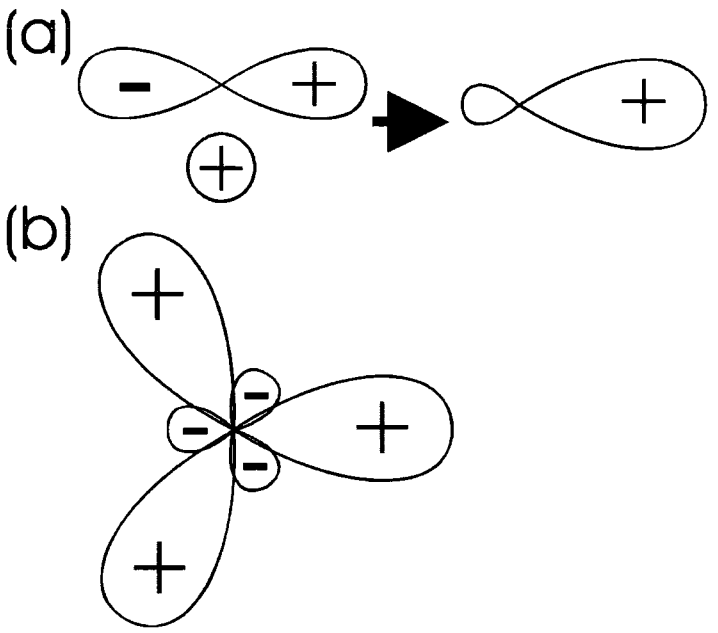

Figure 1.1: (a) combination of s and p orbitals to form an sp orbital (b) sp^2 orbitals

Bonds between the carbon atoms in conjugated polymers may form between the sp^2 hybrids and between the p orbitals. The sp^2 hybrids form bonds with zero angular momentum about the bond axis and are labelled σ bonds. As mentioned earlier, the remaining p_z orbital is unchanged and bonds may also form between these orbitals. These bonds have an angular momentum quantum number of $m = \pm 1$ about the bond axis and are labelled π bonds. Bonding π orbitals and anti-bonding π^* orbitals are shown in Figure 1.2.

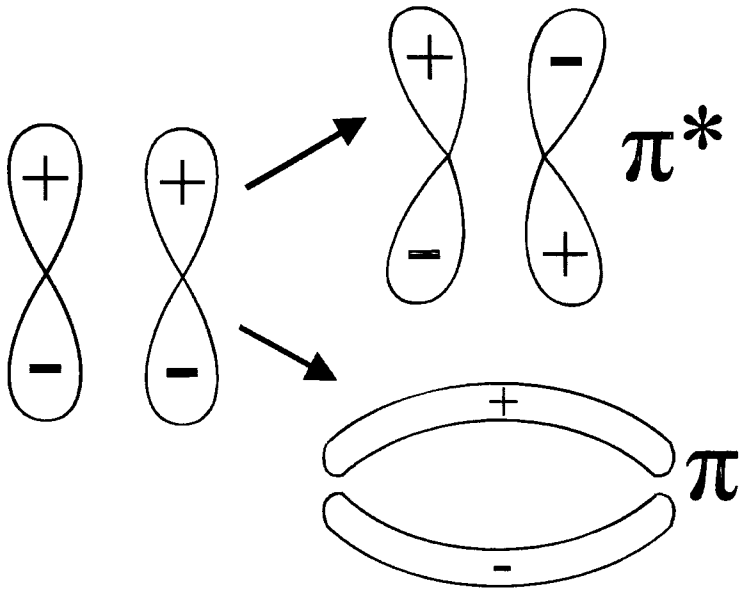

Figure 1.2: p orbitals and the formation of π^* anti-bonding orbitals and π bonding orbitals

In molecules containing heteroatoms, non-bonding orbitals may form. For example, in carbonyl compounds there are two electrons in the non-bonding 2p orbital on the oxygen atom. Absorption of radiation can cause one of these electrons to be promoted to a σ^* or π^* orbital, i.e. an $n \rightarrow \sigma^*$ or $n \rightarrow \pi^*$ transition.

In the ground state, the single bonds in conjugated polymers are σ bonds, while the double bonds consist of a σ bond and a π bond. It is the π bonds which give rise to the interesting properties of these materials. They are delocalised, meaning they may change their position on the molecule and are not confined to forming a bond between any two particular atoms.

Absorption of light in the UV-Vis. range causes a transition from the π bonding orbital to the π^* anti-bonding orbital. This is the transition associated with the first excited state of most conjugated polymers.

Multiplicity

An important property of an electronic state is its multiplicity. Electrons have spin angular momentum, described by a spin quantum number which takes a value $s = \pm \frac{1}{2}$. The algebraic sum of the spins of the electrons in a system is defined as S, and

multiplicity defined as 2S + 1. As a consequence of the Pauli exclusion principle, electrons in the same orbital must have opposite spins i.e. their spins are anti-parallel. Total spin is S = 0 and the multiplicity is therefore 2S + 1 = 1. A state with S = 1 is called a *singlet state*. If one of the electrons is excited into a higher energy state but retains its spin direction, then the multiplicity of the state is unchanged. It is said to be an excited singlet state. A *triplet state* is one in which two electrons have the same spin i.e. their spins are parallel. The multiplicity of this state is 2S + 1 = 3.

Electronic states are labelled according to their multiplicity and their energy level. For example, a singlet ground state is labelled S_0. Excited singlet states and excited triplet states are labelled S_1, S_2 , and T_1, T_2 , respectively, in order of increasing energy.

Selection rules

The overall probability of an electronic transition can be described by a set of conditions called the *selection rules.*[54,55] These relate changes in properties of the electronic state to transition probabilities. The selection rules for polyatomic molecules can be summarized in relation to the oscillator strength f_a of a fully allowed $\pi \rightarrow \pi^*$ transition by the equation

$$f = p_s p_o p_p p_m f_a \tag{1.4}$$

where f is the oscillator strength for the transition and the terms p_s, p_o, p_p and p_m are probability factors taking into account changes in electron spin, orbital symmetry, parity and momentum which occur as a result of the electronic transition. These factors will now be discussed.

Electron spin: p_s

The selection rules predict that transitions in which electron spin changes are not allowed. The consequence of this is that transitions may only take place between states of the same multiplicity i.e. singlet to singlet transitions or triplet to triplet transitions.

A singlet to triplet transition (or vice versa) would require a reversal in spin of an electron and is highly forbidden, with p_s taking a value of the order 10^{-5}. The process is not completely forbidden, as electron spin couples with its orbital angular momentum, with the result that states are not purely singlet or triplet in nature. This *spin-orbit coupling* is stronger in the presence of heavy metal atoms such as indium or platinum.

Orbital symmetry: p_o

This selection rule is related to the spatial properties of the orbitals involved in electronic transitions. If the two orbitals do not possess large amplitudes in the same region of space, then the transitions are said to be overlap forbidden.

Parity: p_p

The wave function of a molecule is termed ungerade (u) if it changes sign on reflection through a centre of symmetry. If it does not change sign then it is termed gerade (g). The parity selection rule states that electronic transitions between states of different parity are allowed, but those between states of the same parity are forbidden.

Momentum: p_m

If a transition results in a large change in the linear or angular momentum of a molecule then it is momentum forbidden.

1.2.2 *Photophysics*

Absorption

If a beam of monochromatic light, intensity I_0 is incident on a sample, e.g. a solution or film of thickness L (cm) then the intensity of the transmitted light is

$$I = I_0 \exp(-\alpha L) \tag{1.5}$$

where α is the absorption coefficient in cm^{-1}. The term αL can also be called the optical density of the sample.[54,55]

The absorption coefficient is a function of the wavelength of the incident light. Plotting absorption coefficient against wavelength gives the *absorption spectrum* for a given material. This carries information about the transitions. As the electronic transitions occur at discrete energies, it might be expected that an absorption spectrum would consist of a series of sharp peaks. However, what is actually observed is an absorption band extending over a range of wavelengths. This is because of coupling to the vibrational and rotational modes which broadens the spectrum.

The total energy of molecule in its electronic ground state is the sum of its electronic, vibrational and rotational energies

$$E_t = E_e + E_v + E_r \tag{1.6}$$

Similarly, the total energy of a molecule in an excited electronic state is

$$E'_t = E'_e + E'_v + E'_r \tag{1.7}$$

If an absorption transition is defined as

$$\Delta E_x = E'_x - E_x \tag{1.8}$$

where $x = t, e, v$ or r, then $\Delta E_r \sim 10$ cm^{-1}, $\Delta E_v \sim 1000$ cm^{-1}, $\Delta E_e \sim 30,000$ cm^{-1}.

In transitions involving ΔE_e, rotational transitions can be neglected in comparison. States involving electronic and vibrational energy are referred to as *vibronic states,* and transitions between two such states are referred to as *vibronic transitions.* Such transitions occur in the visible and ultraviolet regions. Each electronic absorption transition ΔE_e gives rise to an absorption band system, each band of which corresponds to a different value of ΔE_v.

Complex molecules possess many different vibrational modes, though only a small number of these are normally dominant in the electronic absorption spectrum. If we consider a molecule in which only one vibrational mode is dominant, then it approximates to a harmonic oscillator and the total energy in the electronic ground state can be written

$$E_t = E_e + \left(m + \frac{1}{2}\right) E_{tv} \tag{1.9}$$

where the energy of the fundamental vibrational mode in this state is E_{tv} and m = 0, 1, 2, is the vibrational quantum number. Similarly, the total energy in an excited state can be written

$$E'_t = E'_e + \left(n + \frac{1}{2}\right) E'_{tv} \tag{1.10}$$

At room temperature in equilibrium, almost all the molecules are in the lowest vibronic state. A transition to the nth vibrational level of E'_t is the 0 – n vibronic transition. This situation is represented in Figure 1.3.

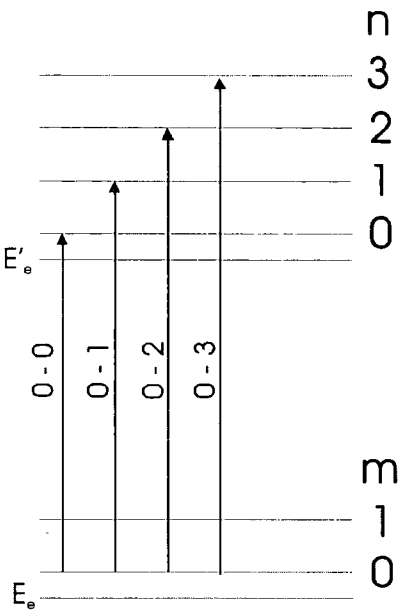

Figure 1.3: Vibronic transitions between the electronic ground state and an excited state of a molecule

Fluorescence

A molecule in an excited state will, after some time, lose its energy and return to the ground state.[56] This de-excitation may occur with or without the emission of a photon, termed radiative and non-radiative decay respectively. The rates at which the radiative and non-radiative decays occur are written k_R and k_{NR} respectively. The total decay rate k is the sum of these individual rates:

$$k = k_R + k_{NR} \tag{1.11}$$

For a system of isolated molecules in their excited state, the intensity of the luminescence should exhibit exponential decay:

$$I = I_0 \exp(-kt) \tag{1.12}$$

where I is the intensity after a time t and I_0 is the intensity at time zero.

Luminescence decay is often described in terms of luminescence lifetime τ rather than decay rate. τ is the reciprocal of k and thus:

$$I = I_0 \exp(-t/\tau) \tag{1.13}$$

Similarly, the radiative and non-radiative decay rates can be written in terms of the natural radiative lifetime and the non-radiative lifetime, τ_R and τ_{NR}. They are equal to the inverse of the respective decay rates. The overall luminescence lifetime is then written:

$$\frac{1}{\tau} = \frac{1}{\tau_R} + \frac{1}{\tau_{NR}} \tag{1.14}$$

Another important quantity is the quantum yield. This can be defined for any process as the number of times that process occurs for every photon absorbed. So, for luminescence it can be written:

$$\phi = \frac{\text{number of photons emitted}}{\text{number of photons absorbed}} \tag{1.15}$$

and this is equivalent to:

$$\phi = \frac{\tau}{\tau_R} = \frac{k_R}{k_R + k_{NR}} \tag{1.16}$$

The same selection rules for electronic transitions governing absorption also apply to emission. Radiative decay is classified as *fluorescence* if it there is no change in multiplicity between the excited and ground states, or as *phosphorescence* otherwise. Fluorescence is brighter and has a shorter lifetime than phosphorescence, as it occurs via an allowed transition as opposed to a forbidden one.

The Born-Oppenheimer approximation

The wavefunction Ψ of a vibronic state can be expressed as the product of the electronic θ and vibrational Φ wavefunctions.[55] This is called the Born-Oppenheimer approximation. The wavefunction of the *m*th vibrational state of a lower electronic state *l* may be written

$$\Psi_{lm} = \theta_l \Phi_{lm} \tag{1.17}$$

and the wavefunction of the *n*th vibrational state of a higher electronic state *u* may be written

$$\Psi_{un} = \theta_u \Phi_{un} \tag{1.18}$$

Transition moments

The strength of the transition between any two states can be calculated from the electric dipole transition moment,[55] defined by the integral

$$\mathbf{M}_{l0\rightarrow un} = e\left\langle \Psi_{l0} \middle| \sum_i z_i \mathbf{r}_i \middle| \Psi_{un} \right\rangle \tag{1.19}$$

where $\mathbf{r}_i$ is the position vector of the *i*th particle of charge $z_i e$ in the molecule. It can be shown that

$$\mathbf{M}_{l0\rightarrow un} = \bar{\mathbf{M}}_{lu} S_{l0,\,un} \tag{1.20}$$

where $\bar{\mathbf{M}}_{lu}$ is the mean value of

$$\mathbf{M}_{lu} = e\left\langle \theta_l \middle| \sum_i \mathbf{r}_i \middle| \theta_u \right\rangle \tag{1.21}$$

and

$$S_{I0,\,un} = \langle \Phi_{I0} | \Phi_{un} \rangle \tag{1.22}$$

Equation (1.22) is the quantum-mechanical statement of the Franck-Condon principle, discussed in the next section.

Franck-Condon principle

The potential energy diagram of a molecule plots the total (electronic & vibrational) energy of a molecule as a function of the positions of its nuclei.[55,57] For simplicity, let us first consider a diatomic molecule. The bond length will have an equilibrium value at which the potential energy of the molecule is a minimum. A plot of bond length versus potential energy gives the potential energy surface.

The potential energy surface can only be represented in two dimensions for a diatomic molecule. Polyatomic molecules require polydimensional plots, with the inter-nuclear separations described in terms of a "configuration co-ordinate" Q.

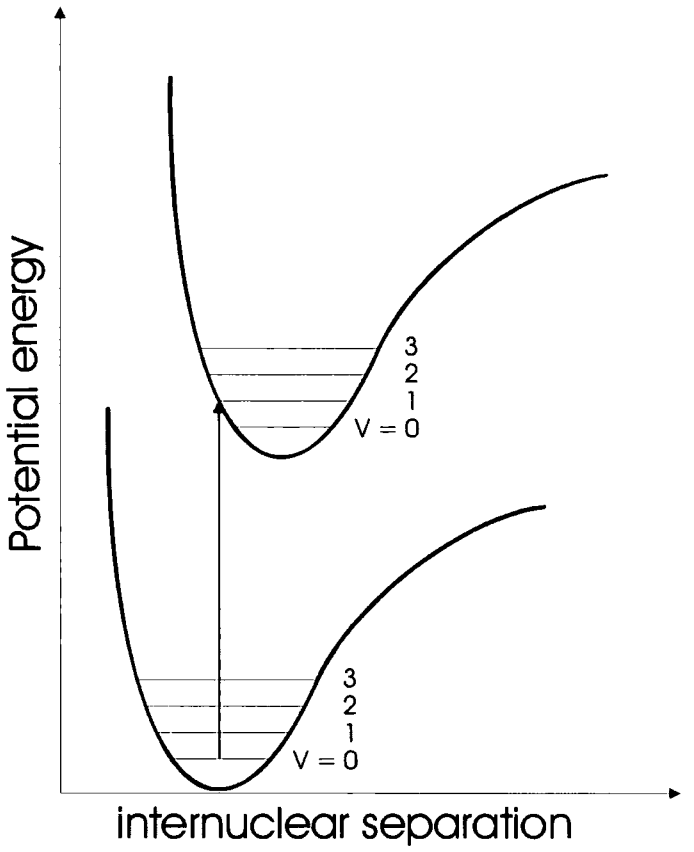

Figure 1.4: Potential energy surfaces for the ground and excited electronic states of a diatomic molecule

The Franck-Condon principle states that because the time required for an electronic transition is negligible compared with that of a nuclear motion, the most probable vibronic transition is one which involves no change in the nuclear co-ordinates. This transition is called the Franck-Condon maximum, represented by a vertical transition on the potential energy diagram. This transition corresponds to maximum overlap between the ground state vibrational wavefunction Φ_{l0} and the excited state vibrational wavefunction Φ_{un} i.e. $S_{l0,\,un}$ is at a maximum. The envelope of the vibronic bands of an absorption band system is referred to as the Franck-Condon envelope.

If the most intense vibronic state is the 0 – 0 transition, then the nuclear configuration of the excited electronic state is similar to that of the ground state. If the Franck-Condon maximum is displaced relative to the 0 – 0 transition, this means that

the nuclear configuration of the excited state is displaced relative to that of the ground state.

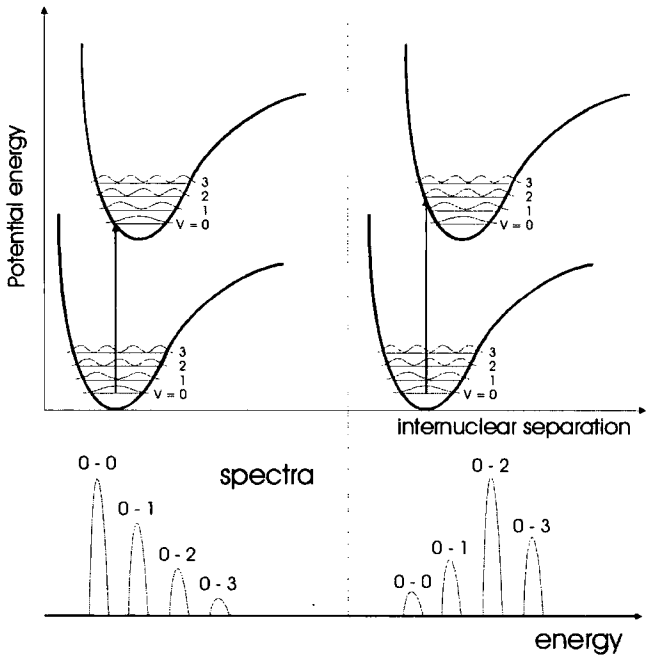

Figure 1.5: Relationship between relative positions of ground and excited state potential energy curves for a diatomic molecule and its absorption spectra

Within a particular electronic state, rapid vibrational relaxation can occur. This means that transitions tend to occur from close to the minimum of the vibrational potential. Therefore, the transition is between the lowest vibrational level of the initial state into any vibrational level of the final state. If the spacings of the vibrational levels in the excited state are similar to those in the ground state there will be an approximate 'mirror image' relationship between the absorption and fluorescence spectra. This is shown for absorption and emission processes in Figure 1.6.

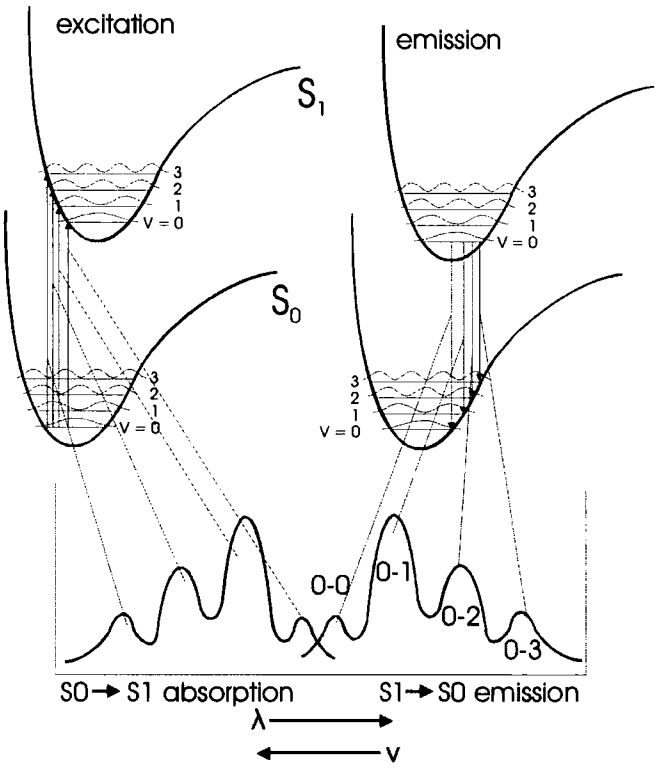

Figure 1.6: Origin of vibrational structure in absorption and emission

Though the 0 – 0 absorption transition and the 0 – 0 fluorescence transition might be expected to have the same energy, this is not necessarily the case. This is because the excited state may relax once populated, and hence the 0 – 0 fluorescence transition would have a lower energy. This gives rise to the observed red-shift in emission of the 0 – 0 peak compared to the 0 – 0 absorption peak.

In general, any red-shift in emission is referred to as a *Stoke's shift*. There are several different processes which may contribute to this shift.

Huang-Rhys parameter

The strength of the overlap between vibrational modes and the intensity of the vibrational peaks in the absorption and emission spectra can be described in terms of the Huang-Rhys parameter *S*:

$$S = \frac{M\omega}{2\hbar}(\Delta Q)^2 \tag{1.23}$$

Where M is the reduced mass of a harmonic oscillator, ω is its angular frequency and ΔQ is the change in configuration coordinate.[47,58] The intensity of the nth peak is then calculated as:

$$I_n = \frac{S^n e^{-S}}{n!} \tag{1.24}$$

In a system in which there are many vibrational modes, each one is described by its own Huang-Rhys parameter, S_i.

1.2.3 *Photoexcitations in conjugated polymers*

There has been much controversy over the description of the excitations created by optical absorption in conjugated polymers.[59] Are these excitations best described in terms of a semiconductor band model involving mobile charge carriers (charged polarons), or as bound electron-hole pairs (neutral excitons)? The main issue is the strength of the electron-electron interactions. Strong electron-electron interaction is equivalent to electron-hole attraction and leads to the creation of localised excitons. This is the case in molecular crystals such as anthracene. Weak interaction on the other hand is more appropriately described in terms of a band picture, as in inorganic semiconductors.

Su, Schrieffer and Heeger developed a model to describe the electronic structure of conjugated polymers, the so-called SSH theory.[60,61] In this model, π-electrons are coupled to distortions in the polymer backbone. Electron-electron interactions are explicitly disregarded and photoexcitation across the $\pi - \pi^*$ band creates solitons (in degenerate ground state systems), polarons and bipolarons. Neglecting the electron-electron interactions has proven to be incorrect. For example, in polydiacetylenes, it has been shown that these interactions are dominant and that neutral excitons are the lowest energy excitations. As a further example, although SSH theory had been used to

describe absorption in PPV reasonably well, for a time the value of the exciton binding energy in this material was not clearly known. Early measurements, including optical absorption and photoconductivity measurements and photo-induced charged transfer in polymer-C_{60} mixtures, implied a low value (< 0.1 eV) for the binding energy.[62,63] This would suggest the formation of charged polarons rather than neutral excitons and hence a band model would be more applicable. However, subsequent measurements have revealed a higher binding energy,[64,65] of the order 0.3 – 0.4 eV, supporting the exciton model.

The exciton model[66,67] has now become commonly accepted in this field. Although conjugated polymers are obviously long molecules, excitations are not delocalised over the entire length of the chain. In these materials, the conjugation is expected to be broken along the chain, forming spectroscopic units on which excitations are localized.[68-70] The breaks in conjugation are often attributed to structural and chemical defects such as kinks and torsions in the polymer backbone. However, it has been shown that in polythiophene, these kinks and torsions do not result in significant localization of excited states.[71] Instead, dynamic localization of excitations, occurring as a result of interaction between the nuclear and electronic degrees of freedom, causes the formation of spectroscopic units. In any case, the notion of these spectroscopic units appears to be sound and conjugated polymer chains can be considered to consist of segments over which the conjugation is unbroken. The length is these segments is typically 5-10 nm, about 6-12 repeat units,[72,73] though it varies from polymer to polymer. Each of these segments forms a site on which an excitation is localised. The energy of an excitation residing on a particular site depends upon the conjugation length: the shorter the length, the higher the energy.[74]

Photoexcitation of these polymers results in a $\pi - \pi^*$ transition of an electron, which is localised on a conjugation segment and leaves behind a hole state. There is a Coulombic interaction between the electron in the excited state and this hole, and they may form a neutral bound state – an exciton. Since there is negligible spin-orbit coupling in these organic materials, these excitons can be labelled according to their total spin. The dominant optical transition is from the singlet ground state to the first excited singlet state. Triplet states also exist, though these may not be populated by

direct optical excitation. Instead, triplet states may be formed by intersystem crossing from the singlet states. In an extended system, the lowest triplet and singlet excitations would be degenerate.[75] However, when the excitations are localised to conjugation segments, electron-electron correlations remove this degeneracy. Singlet states have higher energies than the corresponding triplet states because of greater electron repulsion in the singlet state.[54]

Types of exciton

Excitons can be discussed in limiting approximations, according to their spatial extent and strength of binding.[76]

Frenkel excitons

These are tightly bound excitons, localised on a single atom. This excitation may hop between atoms due to the coupling between neighbours. The Frenkel exciton travels as a wave through a crystal, with the hole remaining close to the electron.

Mott-Wannier excitons

These are weakly bound excitons, with the electron-hole distance extending over a distance large in comparison to a lattice constant. The electron and hole are attracted by the Coulomb potential:

$$U(r) = -\frac{e^2}{\varepsilon r} \tag{1.25}$$

where ε is the dielectric constant.

The energy levels of a Mott-Wannier electron follow a hydrogenic spectrum, given by a modified Rydberg equation:

$$E_n = E_g - \frac{\mu e^4}{2\hbar^2 \varepsilon^2 n^2} \tag{1.26}$$

where E_g is the energy gap.

Charge transfer excitons

Charge transfer excitons are formed when one of the charges is transferred to a neighbouring molecule. The electron is excited to a particular site and not free to orbit the hole, unlike in the Mott-Wannier and Frenkel excitons.

Free carriers in conjugated polymers

Introducing a hole or electron onto a polymer distorts the chain, causing a change in the conjugation phase. This deformation is mobile, and the charge carrier and bond defect together create a pseudo-particle known as a polaron.[77] Polarons may be formed directly by the injection of charge carriers at electrodes, as in polymer LEDs.[78] The operation of polymer LEDs will be described in more detail later.

Absorption and emission in conjugated polymers

In conjugated polymers, interpretation of the absorption and emission spectra is not as straightforward as described in the section on photophysics. A polymer sample is made up of sites with a range of conjugation lengths over which excitations may be delocalised. These sites have a range of transition energies, giving rise to a number of features observed in absorption and emission spectra.

Absorption spectra for conjugated polymers are generally featureless; that is, the peaks in absorption from vibrational coupling described earlier are not actually observed. Since excitations can be created on sites with a distribution of energies, the spectra are broadened and smooth absorption bands are seen instead. There are

exceptions; for example ladder polymer, MeLPPP exhibits peaks in absorption due to its rigid structure and extended conjugation.[79-81]

Emission spectra, on the other hand, exhibit strong peaks in steady-state fluorescence measurements. This is because over their lifetime, excitations will tend to migrate to sites with lower energies. Emission occurs solely from these sites. There is little broadening of the spectra and so vibrational coupling can be observed. This migration to low energy sites is also responsible for some red-shift in the spectra. Excitation migration in conjugated polymers will be described in greater detail later.

An important point to note is that the fact that vibronic peaks are observed indicates a readjustment in bond lengths upon excitation. If there were no change, then only a single spectral line corresponding to the 0 – 0 transition would be observed, as other transitions would be forbidden due to the orthogonality of the vibrational wavefunctions. The vibronic progression also indicates localisation of the excitations: if excitations were highly delocalised, then this would lead to less coupling as changes in bond length would be distributed over a longer conjugation length.[82]

Exciton migration

Excitons may migrate through a polymer by hopping from site to site. For a polymer in solution only intra-chain migration is possible. In films both intra- and inter-chain migration may occur. There is no barrier to hopping to a site with equal or less energy. However, hopping to a site with greater energy (uphill migration) requires interaction with a molecular vibration. These are dependent on temperature and thus exciton migration is more efficient at higher temperatures. At low temperatures, molecular vibrations are frozen out and only downhill migration (i.e. only migration to sites of lower energy) may take place.

Hopping also depends on the energy of the exciton. For an exciton created with high energy there will be many sites of equal or lower energy within hopping range. As exciton energy decreases however, the density of available sites also decreases and further migration becomes less and less likely. Thus, the mobility of the exciton decreases with time. Dynamics of this kind is referred to as *dispersive*.[83,84]

So it has been established that exciton migration is both a function of energy and temperature. Several predictions can be made from this. Firstly, consider a polymer at room temperature excited well away from its low energy absorption band edge. At very short times the emission spectrum from a conjugated polymer will be featureless. This is for the same reasons absorption spectra are featureless – emission is occurring from sites with a range of energies as the excitons have not had time to migrate to the lowest energy sites. As time progresses, the spectrum evolves into that seen in steady-state – there is a red-shift with time and vibrational peaks appear.[85,86]

Now consider a polymer at low temperature, excited deep into its absorption band edge. There is little or no change in the spectrum with time, as there are no lower energy sites for the excitons to migrate to and uphill migration is not possible.

Excitation under intermediate conditions results in the following observations. The lower the excitation energy, the longer it takes excitons to make the first jump. There exists a localisation energy below which the concentration of lower energy sites is so low that the excitons are stationary at low temperature. It is therefore possible to selectively excite a subset of the chains. At higher temperatures, uphill migration prevents this.[87]

As the above processes are so fast, experimental observation requires excitation of polymers with femtosecond pulses and detection of the luminescence with a streak camera or the technique of up-conversion. Excitation energies may be controlled by site-selective spectroscopy, where the wavelength of the excitation pulse is tuned. Temperature may be easily controlled by mounting the sample in a cryostat. Results from experiments performed on PPV and PF follow the above behaviour well.[86,88]

In attempts to analyse the data in more detail and extract information such as hopping rate and energy distribution width, Monte Carlo simulations have been performed to make predictions of the model above.[51,52,88] These simulations generally approximate the distribution of site energies as a Gaussian density of states (DOS). The population of a site of a particular energy is governed by a master equation which takes into account hopping to the site, hopping away from the site and excitation decay.

$$\frac{dn_i}{dt} = -\sum W_{ij} n_i(t) + \sum W_{ji} n_j(t) - \frac{n_i}{\tau_0} \tag{1.27}$$

where n_i is the occupational density of site i characterised by position R_i and energy ε_i. The following form is taken for the hopping rate:

$$\begin{aligned} W_{ij} &= k_0 \chi_{ij} \exp\left[-\frac{\varepsilon_j - \varepsilon_i}{kT}\right] \quad \text{if } \varepsilon_j > \varepsilon_i \\ W_{ij} &= k_0 \chi_{ij} \qquad\qquad\qquad\qquad\quad \text{if } \varepsilon_j < \varepsilon_i \end{aligned} \tag{1.28}$$

Hopping to sites of equal or lower energy is only dependent on the distance between sites. The energy dependence of hopping to sites with higher energies can be modelled by a Boltzmann factor. The distance dependence of the interaction is characteristic of the nature of the excitations. For triplets and charge carriers:

$$\chi_{ij}(R) = \exp\left(-2\gamma R_{ij}\right) \tag{1.29}$$

while for singlet excitons, it follows a Förster-type dependence:

$$\chi_{ij}(R) = \left(R_0/R\right)^6 \tag{1.30}$$

In the Monte Carlo simulations, the medium is modelled as a regular cubic lattice of chromophoric units, and the excited state energies of the sites are statistically distributed according to a Gaussian distribution, providing energetic disorder. An excitation is 'created' at the centre of the lattice and its motion followed over time. For each time increment, its movements are decided by using a random number generator to choose one step out of all possible steps, with each movement waited by its probability. This is repeated for a large number of excitations and the results averaged.

The values calculated for properties such as mean energy, the width of the energy distribution and the temporal behaviour are not so accurate. However, these are complicated systems and the model employed is a rather ideal one. Qualitatively, the

predictions of these Monte Carlo simulations generally match the experimental observations outlined above. It has also been shown experimentally that triplet excitons in polyfluorene obey dispersive dynamics in a Gaussian density of states very well.[50]

1.2.4 *Applications of conjugated polymers*

Electroluminescence and polymer LEDs

Excitons may also be created in conjugated polymers via electronic excitation. This is the property which makes conjugated polymers so attractive for research and gives rise to their most promising application – polymer light-emitting diodes (LEDs).

The simplest polymer LED consists of a thin (~ 100 nm) film of a conjugated polymer sandwiched between two electrodes. One of these is semi-transparent, typically indium-tin oxide (ITO), which forms the anode. Upon application of a bias, electron-polarons are injected from the cathode and hole-polarons from the anode. These drift through the polymer layer under the action of the applied field, and may combine to form excitons. According to simple spin statistics, 75 % of the excitons are expected to form as triplet and 25 % as singlets. There has been some evidence to suggest that the singlet formation ratio is actually higher than this because of a spin-dependent formation cross-section for excitons,[5,89-93] however the picture is still unclear. The excitons which are formed as singlets may then decay radiatively, giving out light which is observed through the transparent electrode. Recombination of the triplet excitons is a spin-forbidden process and hence phosphorescence is very weak.

Usually, either calcium or aluminium is used to make the cathode. Calcium has the advantage of having a lower work function, making for easier charge injection into the device. However, it is highly reactive and requires capping with aluminium to prevent oxidation.

An alternative structure for polymer LEDs is that of a two layer device. For example, a hole transporting layer may be incorporated between the anode and the conjugated polymer, or an electron transporting layer between the cathode and the conjugated polymer. These layers will reduce the barrier for carrier injection and may help to improve the efficiency of the device.

Electroluminescence from conjugated polymers was first demonstrated by Burroughes et al in 1990.[2] Their device used poly(p-phenylenevinylene), PPV as the single semiconductor layer between metallic electrodes. The electroluminescence observed from these devices was green and rather weak. The following year, Alan Heeger's group confirmed this discovery,[14] making their own devices with MEH-PPV, a derivative of PPV with side groups which make the polymer soluble and allow easier film formation by spin-coating. Since then, devices have been fabricated from many conjugated polymers and derivatives. Devices emitting light across the entire colour spectrum have been made using suitable copolymers. Another route to making organic LEDs with different emission colours is to add dopant molecules. Excitations may transfer from the host polymer to these dopants, which then emit at lower energies.

That only 25 % of the excitons may form as singlets is a potential major limiting factor to the efficiency of polymer devices. The use of *phosphorescent* dopants is one possible way to overcome this problem. Phosphorescent dopants contain heavy metal atoms which provide spin-orbit coupling, mixing the singlet and triplet states with the result that phosphorescence is no longer forbidden. Hence, the energy of the triplet excitons in the material can be harvested. Devices employing phosphorescent dopants have exhibited high efficiencies.[94-98]

Light-emitting devices based on polyfluorene are described in more detail later.

Other applications

There are other potential applications for conjugated polymers besides LEDs. These include polymer photovoltaic devices (e.g. solar cells), polymer transistors and electrically-pumped solid state lasers.

Polymer photovoltaic devices are similar in structure to polymer LEDs, but the physical processes occur in reverse. The idea is that light is absorbed in the polymer, creating singlet excitons. These excitons then dissociate into electrons and holes which are transported through the device to the electrodes, giving a current in the external circuit. Because the excitons are so strongly bound, in single-layer devices they will tend to decay radiatively or non-radiatively rather than dissociate into separate charge carriers. One way to improve efficiency is to have the exciton diffuse to a boundary

between polymers with different electron affinities. Then, an electron may gain sufficient energy by moving onto the second material to overcome the coulombic binding energy holding the exciton together. Thus, charge separation will occur. Devices based on polyfluorene are described later.

1.2.5 *Polyfluorene*

The subject of this thesis is the conjugated polymer polyfluorene. This polymer is currently the subject of intense research interest as it appears to be very promising for use in applications such as polymer light-emitting diodes, organic solar cells and electrically-pumped solid state lasers.

The electronic and physical properties of polyfluorene will now be summarized. This will be followed by detailed description of some of the most important applications and features of polyfluorene – its use in polymer LEDs and solar cells, the formation of aligned films and the origin of the low energy emission band sometimes observed.

Electronic and physical properties

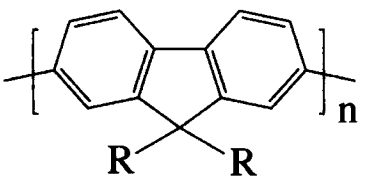

Figure 1.7: Molecular structure of polyfluorene. R represents the side-groups attached to the 9-position on the polymer unit.

The generic structure of polyfluorene is shown above in Figure 1.7. Excitation with ultraviolet light causes a π- π^* transition and formation of a singlet exciton. Emission occurs in the blue region of the spectrum with a high fluorescence quantum yield. Thin films of polyfluorene are easily fabricated via spin-coating from solution. Electrical excitation of these films causes the injection of holes and electrons which may combine

to form excitons. Since the spins of the electron and hole are uncorrelated, both singlet and triplet excitons may be formed. The singlets give rise to strong fluorescence. The phosphorescence from the triplets is weaker as this is a forbidden process.

Polyfluorenes have been synthesized with a variety of side-chains, two of which are shown in Figure 1.8. The absorption and fluorescence spectra of PF2/6, are shown in Figure 1.9. The side-chains are added to improve the solubility of the polyfluorene, though they also have effects on the phase behaviour and morphology of the polymer. For example, it is possible to induce so-called β-phase in poly(9,9-dioctylfluorene) (PFO) in which the polyfluorene chains have extended conjugation and adopt a planar 2_1 helix conformation.[99,100] The optical properties of β-phase PFO are similar to those of the rigid ladder-type conjugated polymer MeLPPP. The absorption spectrum of this phase displays a vibronic progression and there is only a small Stokes shift between the 0-0 absorption and the photoluminescence peak. The β-phase is not present in poly(9,9-diethylhexylfluorene) PF2/6. Polyfluorenes have been synthesized with molecules added to the end of the chains – so-called end-capping. The purpose of this is to restrict the formation of excimers, which impair the efficiency of polyfluorene LEDs.

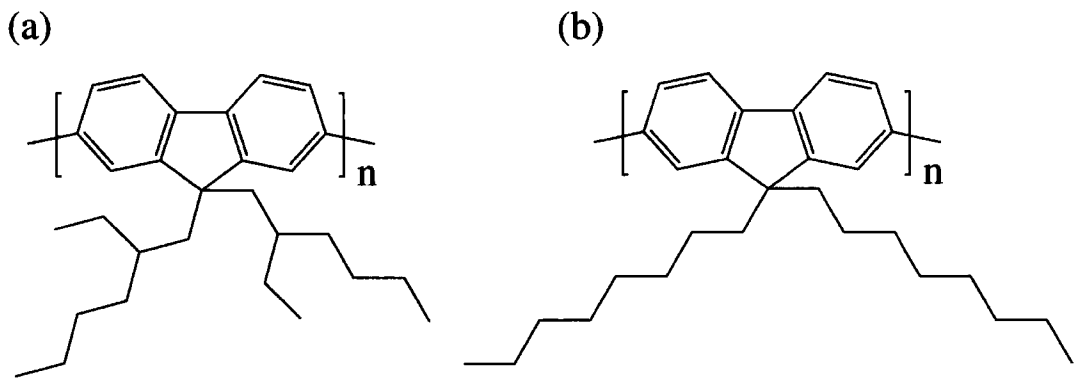

Figure 1.8: Molecular structures of (a) PF2/6 and (b) PFO

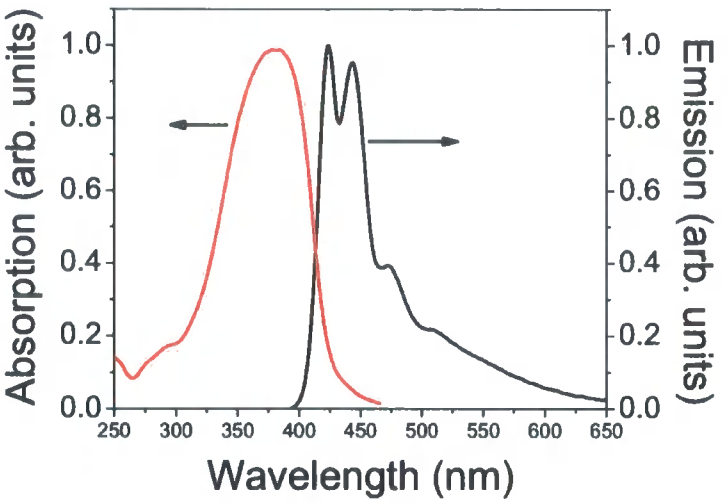

Figure 1.9: Absorption and fluorescence spectra of PF2/6

Polyfluorenes have also been synthesized with a large range of molecular weights, including single fluorene units and oligomers. Oligofluorenes have been used to investigate the size of excitons on polymer chains, through comparison of absorption and emission spectra.

Polyfluorene LEDs

Electroluminescence from polyfluorene was first reported by Ohmori et al in 1991.[101] Their device was a single layer LED consisting of an ITO anode, a 100-200 nm layer of poly(9,9-dihexylfluorene-2,7-diyl) and a Mg:In cathode. It had a broad emission spectrum and was blue in colour. More devices based on polyfluorene and its derivatives followed.[102,103] A frequently encountered problem in these devices was that of stability. In particular, devices exhibited a green emission band which is not normally present in photoluminescence. This green emission band has been attributed to excimer states and chemical defects. Its origin is discussed in more detail below.

The electroluminescence properties of polyfluorene devices vary greatly depending upon factors such as the polyfluorene derivative and the use of electron or hole transporting layers. Device brightness in cd/m^2 can range from around 25 to values in

the thousands.[11,104,105] As a guide, a typical computer display has a brightness of 100 cd/m^2.[106]

Much of the recent work on polyfluorene LEDs has been on achieving emission colours across the entire visible range and improving device stability. Methods of tuning the emission colour include fabricating fluorene-based co-polymers, blending polyfluorene with other polymers or with molecular dopants and chemically attaching emissive moieties. Co-polymers emitting blue, green, yellow and red light have been fabricated.[107-111]

Adding molecular dopants is a popular way of altering the emission colour. Popular dopants for polyfluorene systems include porphyrins.[112-115] For example, tetraphenyl porphyrin and porphyrins containing heavy metal atoms such as platinum or palladium have been used to achieve red emission from polyfluorene films. These dopants act as electron or hole traps, so that carrier recombination occurs at the dopant site. The problem with simply blending the polymer and dopant together is that of device stability – device operation may result in phase separation and a subsequent change in emission colour. Chemically attaching the dopant molecules to the polymer will remove this problem and there are several examples of this.[116-119]

As opposed to making devices with red, green and blue emission, the above techniques can also be used to achieve pure white emission.[6,116,120] Co-polymers of fluorene and fluorenone have been used in this way. This is interesting since the fluorenone moieties are often the cause of device degradation (keto defect formation) as described later. White emission has also been reported from a device employing a homojunction.[121] This homojunction was formed by two layers of poly(9,9-dioctylfluorene-2,7-diyl), though each layer was blended with a small amount of other polymers.

On the issue of device stability, the most important thing seems to be achieving stable emission colours by preventing emission from excimers and/or chemical defects. These are described in more detail below. Many workers have produced spiro-functionalised polyfluorenes which satisfy this requirement.[104,122-124] These rigid spiro groups prevent intermolecular interactions between polymer chains and preserve the

molecular rigidity of the polymer. This leads to high glass transition temperatures and improved thermal and spectral stability.

Solar cells

Polyfluorene derivatives have been used with some success as materials for photovoltaic devices such as solar cells. Solar cells made from single layers of organic yield give disappointing results, with composite systems proving much more successful. It is necessary for the system to contain both electron donating and electron accepting components.[125] Solar cells are much more efficient when absorbing monochromatic light than solar light. Power conversion efficiencies of almost 10 % reported for devices absorbing at infrared wavelengths, whereas anything above 2 % is considered good for solar light. Types of composite systems include simple blends of polyfluorene derivatives and dopants such as fullerenes,[16,23,126] or blends of a polyfluorene derivative and an electron-accepting conjugated polymer.[127-129]

Power conversion quantum yield has been found to be strongly composition dependent, indicating that charge transport is the limiting factor in device performance.[129] Hence, the phase morphology of the device is critical. The most efficient devices are those exhibiting fine-scale phase separation. The structure of the device is important as only those charges created close to the electrodes can be collected.[130] A novel way of controlling phase separation is by making nano-particles of polymers or polymer blends.[127,131] Films made from these nano-particles can be insoluble in the usual solvents, allowing the build-up of multilayer structures of originally soluble polymers.[132]

Aligned polyfluorene films

One interesting property of polyfluorene is its ability to form oriented films – films in which the chain backbones have a preferred orientation. This was first demonstrated by Grell et al[133], who found that PFO has a liquid-crystalline (LC) transition at 170°C. They deposited the PFO on an alignment layer of unidirectionally rubbed polyimide, heated it above its LC transition temperature and then either quenched the film or cooled it slowly. The quenched films formed oriented glassy structures, while the slowly cooled films formed oriented crystalline structures. These layers exhibited

absorption dichroic ratios of 6.6 and 6.4 respectively. (Absorption dichroic ratio is defined as the strength of the absorption parallel to the orientation to that perpendicular to the orientation – see chapter 3).

It was later found by the same workers that PF2/6 gave more highly aligned films than PFO, exhibiting an absorption dichroic ratio of around 11[41]. This was achieved by reducing the chain diameter – PFO has long, linear chains whereas PF2/6, a so-called 'hairy-rod' polymer, has branched chains. PF2/6 was their polymer of choice for making LEDs with polarized electroluminescence. It was necessary to dope the polyimide with a hole-conducting molecule (a starburst amine) to form the alignment layer, as pure polyimide is an insulator. The devices had a polarization ratio of 15, though were not particularly bright (45 cd/m^2 at a turn-on voltage of 19 V).

These devices were later improved upon by Miteva et al,[45] who used a slightly different layer structure (ITO/starburst amine/NPD-doped polyimide/PF/Ca). This created a step-wise barrier for hole-injection and resulted in a device which could operate at lower electric fields and gave polarized emission with a polarization ratio of 21. They later improved the devices still further by using end-capped polyfluorene.[11] The end-capping molecules were hole-trapping moieties. Using these materials increased the EL intensity of the devices as well as reducing unwanted low-energy emission from the layers. Polarized LEDs were optimized for an end-capper concentration of 9 % w/w and had a polarization ratio of 22 at 200 cd/m^2 or 15 at 800 cd/m^2, depending upon the composition of the alignment layer. Efficiencies of up to 0.25 cd/A could be achieved.

Polyimide is not the only material which can be used to make alignment layers. Whitehead et al showed that rubbed PPV layers can also serve this purpose.[46] PFO aligned on these layers had a dichroic ratio of 7 in absorption and about 10 in photoluminescence. This indicates that the PPV is as good an alignment layer as rubbed polyimide. In emission the 0-0 peak was weaker and the peaks less well resolved. This was attributed to absorption by the PPV. LEDs were also made using these layers. They had a lower efficiency than those made with polyimide layers, but exhibited a higher brightness. The integrated dichroism in emission was 19.

One point to note from the work described above is that the polarization ratio in electroluminescence is higher than that in photoluminescence. One explanation for this is that that the PF is expected to be better aligned closer to the alignment layer, and that is where recombination is expected to take place.

Work has also been done to elucidate the structure of aligned PF films. Lieser et al found that in aligned layers of PF2/6, molecules were segregated with respect to their chain length.[134] The chains formed into lamella, with end groups assembled in inter-lamellar regions. Electron diffraction patterns of the film and x-ray diffraction measurements on fibres showed that the polymer molecules adopt a helical (5/q) conformation, packing in a trigonal unit cell. Molecular modelling calculations were more in favour of a 5/2 than a 5/1 helix, as the 5/2 helix would match the observed packing and give a plausibly low torsion angle. Knaapila et al later examined similar aligned PF2/6 films using grazing incidence x-ray diffraction and found that two distinct orientation types form.[135] Both are hexagonal, one with its crystal axis perpendicular to the surface (Type I) and the other with its crystal axis parallel to the surface (Type II). A greater proportion are in type I, particularly in the thinner films which also show higher alignment. The amount of type II increases with prolonged annealing. Computational models fit to the data also suggested 5/2-helicity and gave a mean inter-chain distance of 13 Å.

Factors affecting the alignment of PF films have been found to include the spinning solvent used and the molecular weight of the polymer. Banach et al investigated a polyfluorene-based copolymer, F8BT, which exhibits fast electron transport.[39] They found that spin-coating from aromatic solvents with high boiling points gave the most highly aligned films (dichroic ratio in excess of 10), spin-coating from aromatic solvents with lower boiling points gave lower dichroic ratios (around 5) and that chlorinated solvents gave very low alignment. It was also found that 'wet alignment' (spin-coating from films containing residual solvent) gave the most highly aligned films, which was suggested to be due to increased mobility of the polymer chains.

The same workers found that increasing the F8BT molecular weight increased the melting temperature and reduced the speed at which it aligned to a rubbed surface.[40] It also limited the degree of alignment possible. The larger molecular weight polymers

had an inability to reorient to the rubbing direction and retained multi-domain structure. This would hinder the charge transport properties. Dichroic ratios of up to 29 were possible with the lower molecular weight polymers. The effects of molecular weight on the alignment and structure of PF films have been investigated in detail by Knaapila et al.[42,43] Their measurements showed that low molecular weight (LMW) PF exhibits nematic structure in alignment, rather than the hexagonal structure of high molecular weight (HMW) PF. To be more specific, there is a threshold molecular weight of M_n = 10000. Below this threshold (the LMW region), the PF shows a nematic phase at all temperatures. Above it (the HMW region), the PF shows a hexagonal phase and a nematic phase at low and high temperatures respectively. The degree of alignment increases linearly with molecular weight in the LMW region. In the HMW region, the degree of alignment decreases exponentially with molecular weight. These observations are in agreement with a theory based on free-energy considerations. The LMW PF still exhibited 5-helicity, in agreement with molecular-mechanics-calculated structure. The dichroism in absorption did not depend strongly on the thickness of the film.

Low energy emission from polyfluorene films

A low energy emission band has been observed in polyfluorene films. This wide band is centred around 550 nm. This low energy emission is generally observed after polyfluorene films have been excited optically or electrically – photoinduced degradation and electrical degradation respectively. It is undesired for this emission to develop as it shifts the colour of emission from deep blue to green-yellow and also decreases the overall emission intensity.

Initially, most observations of low energy emission in polyfluorene were described in terms of excimers. Excimer is short for excited dimer, a state forming between two identical chromophores. One of these chromophores is initially in an excited state and the other in its ground state. It was believed that excimers could form by localized molecular motions, particularly in electroluminescence.[35] With this in mind, polyfluorenes were fabricated with end-capping molecules.[136] These were intended to increase the steric hindrance of the polymer chains, thus preventing excimer formation.

Opinion on the origin of this low energy emission has now shifted in favour of on-chain defects. These on-chain defects are keto defects – carbonyl groups forming at the 9-position of the fluorene, creating a fluorenone unit. Fluorenone has its emission in the same position as the PF low energy emission, immediately making it a likely candidate. To begin with, Gaal et al observed low energy emission from polyfluorene films that had been heated in air but not from those heated in inert conditions, i.e. oxidation is responsible.[137] Zojer et al performed quantum-chemical calculations on polyfluorene chains containing fluorenone moieties which back up this hypothesis, assigning the emission to a charge-transfer state.[138] List et al found that difunctionalization (having two side-chains) at the 9-position on the fluorene unit was more efficient than monofunctionalization (having only one side-chain) at preventing the low-energy emission band forming.[139] Polyfluorene samples with only a single side-chain showed a strong C=O vibration in infra-red absorption spectra, indicating the formation of carbonyl groups. After illumination in air however, the PF with two side-chains exhibited the same low-energy brand and C=O signal. Panozzo et al have suggested that the emission is actually from fluorenone excimers.[140] Fluorene-fluorenone copolymers show more intense low energy emission than photodegraded polyfluorene containing similar amounts of fluorenone. This could be explained by efficient stacking of fluorenone moieties when copolymer films are fabricated. In a photodegraded polymer reorganisation cannot take place and excimers cannot form. The amount of fluorenone in photodegraded polymers is enough to quench the polymer fluorescence however. This attribution of the green emission band to fluorenone excimers rather than localised fluorenone π- π^* transitions has been supported by Sims et al.[141]

The assignment of keto emission to a charge-transfer state is supported by measurements by Hintschich et al, who investigated the energy transfer mechanisms to keto defects.[142] They found that excitations initially created on polyfluorene can migrate to the defect sites. This process is much less efficient in solutions than in films due to the absence of inter-chain energy transfer. The energy transfer process in photoluminescence was identified as Förster transfer by Gong et al.[143] In electroluminescence, they found that charge trapping on the keto defect sites increased the low energy emission still further.[6] Although this is a problem in PF-based LEDs

where deep blue emission is desired, it can be exploited to fabricate LEDs with different emission colours. For example, the same authors made white-emitting organic LEDs by using a fluorene-fluorenone copolymer doped with an iridium complex.

1.3 Summary

Some of the main areas of research into PF have been described above. These are all of relevance to practical applications. This thesis will describe investigations into some of the basic physical processes that are of importance in these areas.

Perhaps the most important potential application of PF is the polymer LED. These have the promise of being cheap, easy to fabricate and may even be used in flexible displays. LEDs using aligned films emit polarized luminescence and may be used as backlights in LCDs. The emission intensity from films and devices depends upon the angle at which they are viewed. This directionality is important, as it is obviously preferential for a display to be clearly visible from as wide an angle as possible. Calculating the emission intensity as a function of direction requires knowledge of the optical constants of PF. These are important properties of any material and also affect fundamental processes such as energy transfer and the spatial extent of excitations. Chapter 3 is devoted to calculating these for unaligned and aligned PF films through the technique of variable angle spectroscopic ellipsometry.

Also of great importance is the process of exciton migration. Excitons are the emissive excitations in polymer LEDs and they are created upon photo-excitation in solar cells, so knowledge of their properties is obviously desired when it comes to optimizing these devices. Exciton migration to keto defects reduces the luminescence efficiency of polyfluorene films, and so understanding how they move will help to overcome this problem. Chapter 4 considers exciton migration by looking at energy transfer to a fluorescent probe molecule in PF films.

Chapter 5 takes the results from the earlier chapters and applies them to further measurements. In particular, the optical constants are used to investigate the emission intensity as a function of angle from unaligned and aligned films. Polarized fluorescence measurements are also employed to provide further information on

exciton migration in PF. Finally, energy transfer and aligned films are combined to investigate the possibility of achieving polarized luminescence with a range of colours. This would not only have practical applications but may also elucidate the process of energy transfer in these materials.

Chapter 2: Materials and methods

2.1 Introduction

This chapter briefly describes some of the practical aspects of the work described in this thesis. Firstly, the materials used are described. Then, the basics of the fabrication techniques are described. Finally, the more common measurement instruments are discussed.

2.2 Materials

2.2.1 *Polyfluorene*

The polyfluorene used in this work was poly(9,9-diethylhexyl fluorene). The molecular structure is shown in Figure 2.1. The polyfluorene was kindly provided by Professor Ulli Scherf and co-workers at the University of Wuppertal. Its synthesis and purification are described elsewhere.[144] Details of the molecular weight of the polyfluorene used can be found in each chapter.

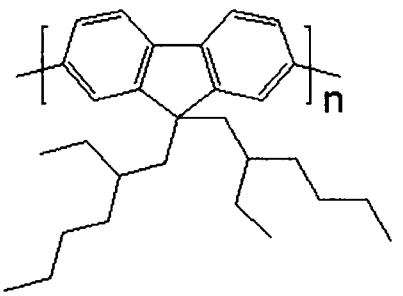

Figure 2.1: Molecular structure of poly(9,9-diethylhexyl fluorene)

2.2.2 *Tetraphenyl porphyrin*

TPP is a red-emitting dye. Its molecular structure is shown in Figure 2.2. It was purchased from Porphyrin Products, Inc. and used without further purification.

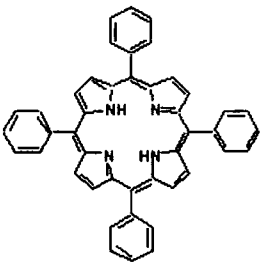

Figure 2.2: Molecular structure of tetraphenyl porphyrin

2.2.3 *DCM*

4-(dicyanomethylene)-2-methyl-6-(p-dimethylaminostyryl)-4H-pyran (DCM) is an orange-emitting laser dye. Its molecular structure is shown in Figure 2.3. It was purchased from Exciton, Inc. and used without further purification.

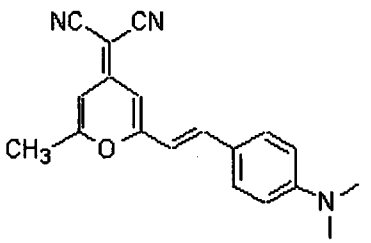

Figure 2.3: Molecular structure of 4-(dicyanomethylene)-2-methyl-6-(p-dimethylaminostyryl)-4H-pyran

2.2.4 *Spectrosil*

Film samples were generally fabricated on Spectrosil discs. Spectrosil is the commercial name for this material, which is UV-grade quartz and can transmit light down to wavelengths of 179 nm.

2.2.5 *Silicon wafers*

For the ellipsometry measurements, film samples were fabricated on silicon wafers. These silicon wafers had oxide layers of various thicknesses. Further details are given in Chapter 3. These substrates were kindly provided by Andrew Gallant of the Department of Engineering, Durham University.

2.2.6 *LCD cells*

For the fabrication of aligned films on transparent substrates, it was convenient to use LCD cells. These LCD cells consist of two glass substrates glued together with a small spacing between them. On top of the glass substrates is a layer of ITO, followed by a layer of rubbed polyimide. This rubbed polyimide provides the alignment surface. By splitting the LCD cell, two alignment substrates can be obtained. The LCD cells were purchased from E.H.C. Co., Ltd (Japan).

2.3 Fabrication

2.3.1 *Spin-coating*

Film samples were generally fabricated by the process of spin-coating.[145] This process involves first placing an excess amount of polymer solution on a substrate. This substrate is then rotated at high speed, thus spreading the fluid. As the substrate is rotated, the fluid is spun off its edges. The solvent is usually volatile, providing for its simultaneous evaporation. The thickness of the films can be controlled by the solution concentration, spinning speed and time.

In the case of polyfluorene here, a reasonably concentrated solution of the polymer (about 10 mg/ml) was generally used. The substrate would be spun at typically 2500 rpm for 60 seconds. Film thickness was in the order of tens of nanometres.

2.4 Measurement instruments

2.4.1 *Spectrofluorimeter*

The spectrofluorimeter used was a Fluoromax 3 spectrofluorimeter from Jobin Yvon. Along the optical path its components are a Xenon arc lamp, excitation monochromator, sample component, emission monochromator and finally the signal detector. The monochromators consist of a reflection grating and adjustable slit. The signal detector is a photomultiplier tube. There is also a silicon photodiode reference detector sitting just before the sample compartment which can be used to monitor and correct for the wavelength response of the lamp as well as for fluctuations in the lamp power supply. Both the reference and signal detectors have correction factor files in order to correct for the wavelength dependencies of the optical components of each monochromator and the detectors themselves.

For fluorescence polarization anisotropy measurements, Glan-Thomson polarizers were placed in the excitation and emission beam paths of the spectrofluorimeter. As described later, these measurements require correction for the polarization response of the instrument. This response is taken into account by the G-factor,[56] which is the ratio of the recorded intensities of vertically and horizontally polarized light of equal actual intensity. This was found as using a series of dyes in solution. These solutions were excited with horizontally polarized light and the emission recorded vertically and horizontally. Since the emission intensity is expected to be the same for both HH and HV this allows calculation of the G-factor. The fluorescence of the dyes covered the whole spectral region from 400 nm to 760 nm, the region of interest in these experiments. Overlap between the calculated G-factors for each dye was good, hence the G-factor found was repeatable. The collated results are shown in Figure 2.4. These results are rather noisy, and it was desired to find a G-factor that was a smooth function of wavelength. This was performed by fitting polynomial curves to the results. This fit is given by the red line in the figure, which is seen to pass through the data very well.

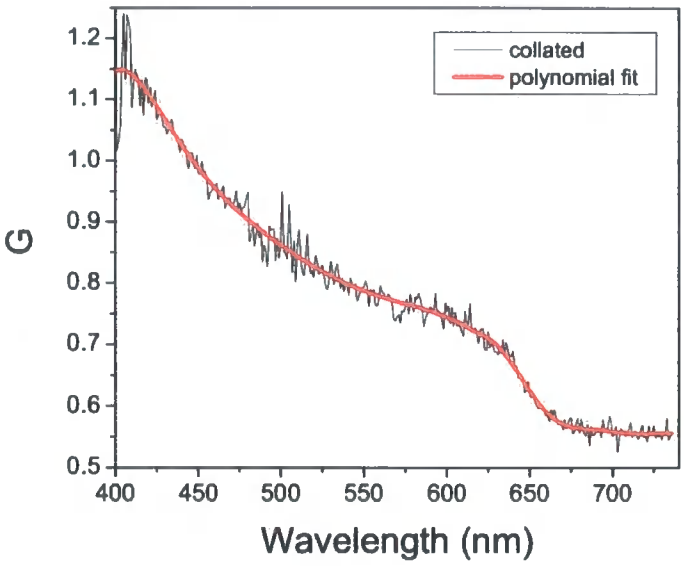

Figure 2.4: The emission G-factor for the Jobin-Yvon Fluoromax spectrofluorimeter. The black line is the G-factor calculated for each wavelength, from a series of dyes in solution. The red line is a polynomial fit to these data, to give the G-factor as a smooth function of wavelength.

The G-factor for the excitation beam can be found in a similar way. The emission polarizer is set to the horizontal position and intensity measured with the excitation polarizer set both horizontally and vertically. The intensity should be identical in each configuration, so the measured intensity allows the correction factor to be calculated. It was found that over the wavelength range of interest (300 – 400 nm) the excitation G-factor I_{VH}/I_{HH} was approximately 0.7.

2.4.2 *Time-correlated single photon counting (TCSPC)*

Time-correlated single photon counting is a technique for measuring luminescence decay profiles.[56] The basic idea is that a sample is excited with a pulsed laser. Following this excitation, the sample will emit photons. Less than one photon for every hundred pulses will be detected, for reasons explained later. The arrival time of each photon relative to the pulse is measured. As the photons are detected, a histogram is built up, showing the number of photons collected versus arrival time. For a sufficiently large number of photons this recovers the luminescence decay profile.

This measured luminescence decay profile is not the intensity decay of the sample. We wish to find the impulse response function – the intensity decay of the sample following a δ-function excitation. The laser pulse is not a δ-function, but will rather have a finite width. It can be considered as a series of δ-functions with different amplitudes. Each of these δ-functions excites an impulse response from the sample, with an intensity proportional to the amplitude of the δ-function. The measured luminescence decay is the sum of these impulse responses, which have different amplitudes and starting times. This is called the *convolution* of the lamp profile and sample impulse response.

Recovering the impulse response function involves the *deconvolution* of the measured luminescence decay. A form for the impulse response function is guessed, usually an exponential or sum of exponentials, containing amplitudes and decay times as variable parameters. This function is convoluted with the measured lamp profile and the best fit to the measured luminescence decay found. In this work, software provided by George Striker[146] was used for the deconvolution of TCSPC data.

The specifics of the single photon counting system used here are as follows: A pulsed diode laser (Picoquant) was used to excite the samples at 390 nm with 75 ps pulses (FWHM). Emission was collected by a first lens and focused by a second lens onto a monochromator slit. The detector was a Peltier-cooled MCP (Hamamatsu). Single photon counting was performed by a Becker & Hickl electronics board and software.

For analysis of fluorescence polarization anisotropy measurements, the G-factor of the TCSPC system was found. This was done here using the method of tail matching. This method assumes that at long times, rotation of dye molecules in solution will completely depolarize the fluorescence. Therefore, the emission intensity should be equal for horizontally and vertically polarized fluorescence. Any difference in the measured intensities will be due to the polarization response of the system.

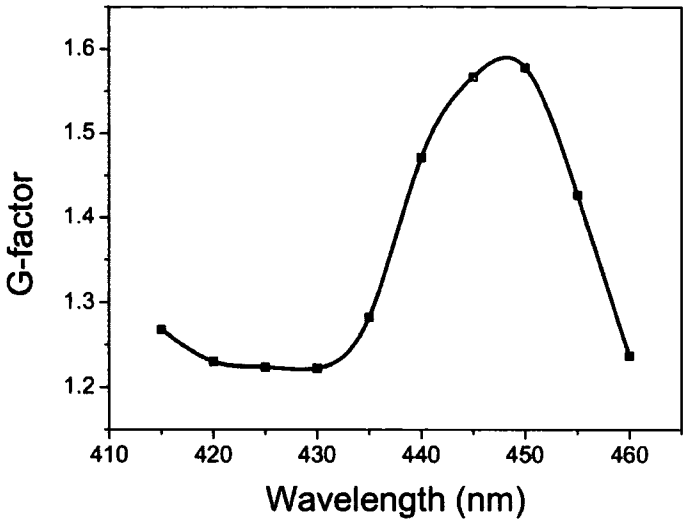

Figure 2.5: G-factor for TCSPC system, found by tail-matching.

2.4.3 *VASE Ellipsometer*

The ellipsometer used was a Variable Angle Spectroscopic Ellipsometer from J.A. Woollam Co. Inc. Its operation is described in detail in Chapter 3.

Chapter 3: Optical constants of polyfluorene films

3.1 Introduction

The fundamental properties of any material include its optical constants – refractive index and absorption coefficient. These describe the passage of light both through the material and at boundaries between different materials. When it comes to investigating photo- and electroluminescence from thin films, the optical constants are obviously of particular importance since they affect the path that luminescence takes and hence how it is actually seen. The intensity of the light from a polymer film viewed at a particular angle depends upon its transmission at the film boundary. The amount of light transmitted is described by the Fresnel transmission coefficients, which are functions of both angle of incidence and the wavelength of the light. The relationship between the light generated in the polymer and the light leaving the film is called the out-coupling. In photoluminescence experiments, proper analysis of the data may require correction for these effects. In electroluminescence, the optimization of devices will require knowledge of these constants. For example, since the out-coupling is a function of wavelength, the colour of a display will appear different depending on which angle it is viewed at. This determines the viewing angle – the largest angle at which a display can clearly be viewed. Therefore, the determination of the optical constants is a necessary task.

A standard technique for determining the optical constants of thin films is that of ellipsometry.[112,147-149] This method involves reflecting light off a sample and measuring the change in its polarization state. It is an indirect method and the experimental results must be compared with those predicted by a theoretical model, which is then optimized to provide a good description of the sample.

The samples investigated here were films of unaligned and aligned polyfluorene. Unaligned films, formed by simple spin-coating with no further treatment, give rise to unpolarized emission upon optical or electrical excitation. This is because there is no

preferred orientation of the polymer chains within the plane of the film. It is possible to make aligned films in which the chains do have a preferred orientation and the emission from these can be highly polarized. One of the main aims in making aligned films is the fabrication of polymer LEDs emitting polarized light. These could be used as backlights for liquid crystal displays which would remove the need for an initial polarizer, therefore increasing brightness and efficiency. Aligned films have also been used in polymer transistors which exploit the improved mobility of charge carriers through the layer.

Since the polymer chains are arranged in different ways in unaligned and aligned polymer layers, the optical constants will be different and must be determined separately. Also, both kinds of films are expected to exhibit optical anisotropy – different optical constants in different directions. This adds an extra level of difficulty to their determination.

This chapter is structured as follows: firstly, the meaning of the optical constants and anisotropy is discussed. Secondly, the technique of ellipsometry is described. Thirdly, the experimental details are given. Fourthly, the results and their analysis are presented, and then finally the conclusions.

3.2 Background – optical constants and anisotropy

3.2.1 *Optical properties of a dielectric*

To begin to understand the origin of the refractive index and absorption coefficient, we will consider an isotropic dielectric material – one containing no free charges, whose properties are independent of direction. There are positive charges in the material, associated with nuclei and negative charges associated with electrons. These charges will move in response to an electric field with the effect that the negative charge distribution moves in a direction opposite to the electric field. This results in a dipole moment due to the displaced charge, given by the product of the charge q and the effective separation y of the positive and negative charge in the dipole:

$$\mathbf{P} = -q\mathbf{y} = -ne\mathbf{y} \tag{3.1}$$

where n is the number density of the electrons. Now consider a quantum system of two levels separated by $\hbar\omega_T$ interacting with light of a frequency ω. The equation of motion is that of a damped, driven harmonic oscillator:

$$m\frac{d^2y}{dt^2} = -eE - m\omega_T{}^2 - \frac{m}{\tau}\frac{dy}{dt} \tag{3.2}$$

y represents the displacement of electronic charge, m is the free electron mass and the damping is represented by relaxation time τ. When driven by an applied field $E = E_0 e^{-i\omega t}$ the solution is $y = y_0 e^{-i\omega t}$ with:

$$y_0 = \frac{eE_o/m}{\omega_T{}^2 - \omega^2 - i\omega/\tau} \tag{3.3}$$

y_0 increases dramatically as ω approaches the resonant frequency ω_T. The polarization therefore is:

$$\mathbf{P} = \frac{ne^2/m}{\omega_T{}^2 - \omega^2 - i\omega/\tau}\mathbf{E} \tag{3.4}$$

Macroscopic polarization is given by the equation:

$$\mathbf{P} = \varepsilon_0 \chi \mathbf{E} \tag{3.5}$$

With:

$$\varepsilon_r = 1 + \chi \tag{3.6}$$

Where χ is the susceptibility of the dielectric and ε_r is its dielectric constant. These describe its polarization in response to an applied field.

With this expression for the polarization, we can now use Maxwell's equations to find how light propagates in a dielectric medium. In the most general form, Maxwell's equations can be written:

$$\nabla \cdot \mathbf{E} = \frac{\rho}{\varepsilon_0} \tag{3.7}$$

$$\nabla \cdot \mathbf{B} = 0 \tag{3.8}$$

$$c^2 \nabla \times \mathbf{B} = \frac{\partial \mathbf{E}}{\partial t} + \frac{\mathbf{J}}{\varepsilon_0} \tag{3.9}$$

$$\nabla \times \mathbf{E} = -\frac{\partial \mathbf{B}}{\partial t} \tag{3.10}$$

B is the magnetic induction, **E** is the electric field, **J** is the current density and ρ is the electric charge density.

For a dielectric, it can be shown that $\rho = -\nabla.\mathbf{P}$ and $\mathbf{J} = \partial \mathbf{P}/\partial t$. This leads to the Maxwell equations for a dielectric:

$$\nabla \cdot \mathbf{E} = \frac{-\nabla \cdot \mathbf{P}}{\varepsilon_0} \tag{3.11}$$

$$\nabla \cdot \mathbf{B} = 0 \tag{3.12}$$

$$c^2 \nabla \times \mathbf{B} = \frac{\partial \mathbf{E}}{\partial t} + \frac{1}{\varepsilon_0}\frac{\partial \mathbf{P}}{\partial t} \tag{3.13}$$

$$\nabla \times \mathbf{E} = -\frac{\partial \mathbf{B}}{\partial t} \tag{3.14}$$

Combining these equations the following expression can be reached:

$$c^2 \nabla^2 \mathbf{E} = \left[1 + \frac{ne^2}{m\varepsilon_0\left(\omega_o^2 - \omega^2 - i\omega\gamma\right)}\right]\frac{\partial^2 \mathbf{E}}{\partial t^2} \tag{3.15}$$

The solution of this equation is a plane wave $\mathbf{E} = \mathbf{E}_0 e^{i(ky-\omega t)}$, with:

$$k^2 = \frac{\omega^2}{c^2}\left[1 + \frac{ne^2}{m\varepsilon_0\left(\omega_o^2 - \omega^2 - i\omega\gamma\right)}\right] \tag{3.16}$$

This can be separated into a real and an imaginary part and thus the plane wave becomes:

$$\mathbf{E} = \mathbf{E}_0 e^{i(k_R y + ik_I y - \omega t)} = \mathbf{E}_0 e^{-k_I y} e^{i(k_R y - \omega t)} \tag{3.17}$$

That is, the imaginary part of k gives rise to absorption while the real part represents the harmonic wave. If the wave-vector is complex, then so is the refractive index:

$$k = \left(\frac{\omega}{c}\right) n \tag{3.18}$$

$$k_R + ik_I = \left(\frac{\omega}{c}\right)\left(n_R + in_I\right) \tag{3.19}$$

The real part of the complex refractive index is the usual refractive index describing the change in the velocity of light, whereas the imaginary part describes absorption.

Substituting (3.18) into (3.16) gives:

$$n^2 = 1 + \frac{ne^2}{m\varepsilon_0\left(\omega_o^2 - \omega^2 - i\omega\gamma\right)} \tag{3.20}$$

From (3.5), (3.6) and (3.20), we have:

$$\varepsilon_r = n^2 \tag{3.21}$$

The dielectric constant of the material is therefore also a complex quantity. For the Lorentz oscillator model considered above, the real and imaginary parts of the complex refractive index will take the form shown in Figure 3.1.

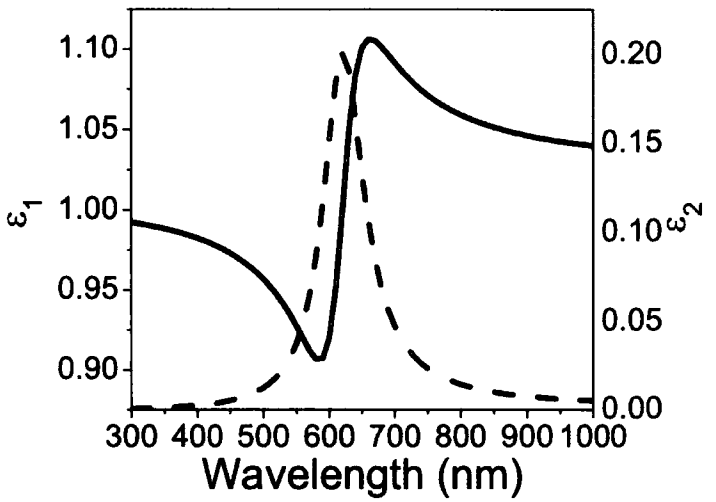

Figure 3.1: Example of the real (solid line) and imaginary (dashed line) parts of the complex refractive index for a Lorentz oscillator model

The real and imaginary parts of the dielectric constant are not independent of each other. They are related via the Kramers-Krönig dispersion relations, which take the following form:

$$n(E)-1=\frac{2}{\pi}P\int_0^{\infty}\frac{E'k(E')}{E'^2-E^2}dE' \tag{3.22}$$

This form explains that absorption at one frequency leads to dispersion in the refractive index at all other frequencies.

3.2.2 *Anisotropy in the optical constants*

The above discussion applied to an isotropic medium – one in which the optical constants do not depend upon the propagation direction of the light. Anisotropic media also exist, in which the optical properties do depend upon the direction. Here, the

induced polarization depends upon the electric field according to the following tensorial relation:

$$\mathbf{P}^{1} = \varepsilon_0 [\chi] \mathbf{E} \tag{3.23}$$

where $[\chi]$ is the first-order electric susceptibility tensor. The electric induction $\mathbf{D}$ is therefore:

$$\mathbf{D} = \varepsilon_0 [\varepsilon] \mathbf{E} \tag{3.24}$$

where $[\varepsilon] = [I] + [\chi]$ is the relative permittivity tensor and $[I]$ is the identity tensor. It is always possible to diagonalize this tensor and write a relation containing only three independent coefficients:

$$\begin{bmatrix} D_x \\ D_y \\ D_z \end{bmatrix} = \varepsilon_0 \begin{bmatrix} \varepsilon_x & 0 & 0 \\ 0 & \varepsilon_y & 0 \\ 0 & 0 & \varepsilon_z \end{bmatrix} \begin{bmatrix} E_x \\ E_y \\ E_z \end{bmatrix} \tag{3.25}$$

There are three classes of optical media, based upon the relative values of these coefficients. If they are all equal, the medium is isotropic. If $\varepsilon_x = \varepsilon_y \neq \varepsilon_z$ then the medium is uniaxial with its optic axis along z. If $\varepsilon_x \neq \varepsilon_y \neq \varepsilon_z$ then the material is biaxial.

The permittivity seen by an electromagnetic wave propagating through an anisotropic material depends upon both its direction of propagation and its polarization. For example, a wave travelling along the z-direction with $\mathbf{E}$ polarized along x will see a permittivity ε_x. If it is polarized along y it will see a permittivity ε_y. A wave propagating along z with some general polarization can be separated into two parts polarized along x and y which can be treated independently.

The situation is more complicated for a wave travelling along an arbitrary direction. Again, the wave can be split into two perpendicularly polarized components. Their

polarizations and the permittivity they see can be found using Maxwell's equations. A simpler way, which is equivalent to solving Maxwell's equations, is that of the index ellipsoid.

The index ellipsoid is defined by

$$\frac{x^2}{\varepsilon_x/\varepsilon_0}+\frac{y^2}{\varepsilon_y/\varepsilon_0}+\frac{z^2}{\varepsilon_z/\varepsilon_0}=1 \tag{3.26}$$

This represents an ellipsoid with principal axes parallel to x, y and z, with lengths $2\sqrt{\varepsilon_x/\varepsilon_0}$, $2\sqrt{\varepsilon_y/\varepsilon_0}$ and $2\sqrt{\varepsilon_z/\varepsilon_0}$. The procedure for finding the allowed solutions for a given direction of propagation is as follows: Take a plane through the origin which is perpendicular to the direction of propagation and find the intersection between this plane and the index ellipsoid. This intersection is an ellipse whose major and minor axis represent the directions of the two allowed polarizations. The lengths of these axes are $2n_1$ and $2n_2$ where n_1 and n_2 are the refractive indices for the two allowed solutions.

Uniaxial anisotropy will be of most relevance to the material discussed in this chapter and so is now described in more detail. The index ellipsoid for a material with uniaxial anisotropy is shown in Figure 3.2:

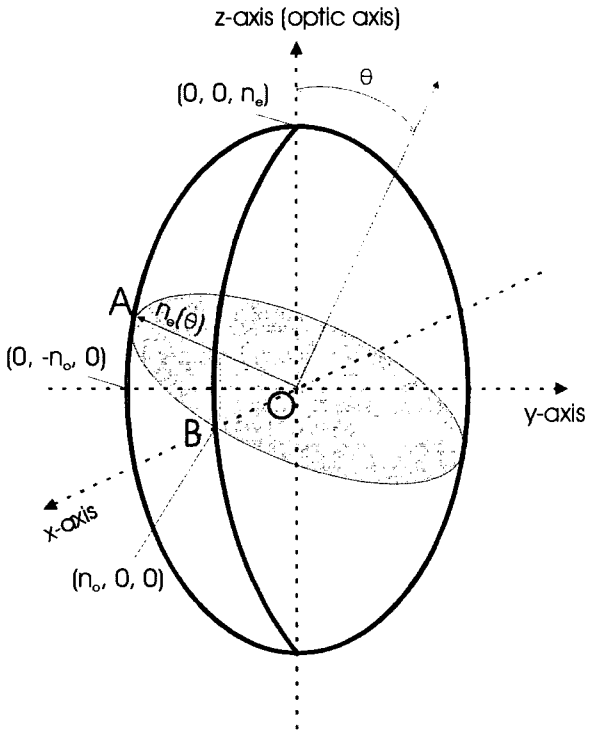

Figure 3.2: Index ellipsoid for a material with uniaxial anisotropy

The ellipsoid has rotational symmetry around *z*. A beam propagating along a general direction, at an angle θ to the z-axis can be split into two components. One of these is called the *ordinary* component and is always polarized along OB with refractive index n_o. The other solution is polarized along OA and can take a refractive index between n_o and n_e. A material is described as being optically positive if $n_e > n_o$ and optically negative if $n_o > n_e$.

It is, of course, not only the refractive index that is anisotropic. Similarly, there will be anisotropy in the absorption coefficient. The absorption coefficient and refractive index along a particular axis in the material are linked by the Kramers-Krönig relation, as described before.

3.3 Background – ellipsometry

A standard method of obtaining optical constants is that of ellipsometry. This is a non-destructive thin film analysis technique. It works by measuring the change in polarization state of light reflected off the surface of a sample. The properties of the sample may not be found directly, instead, an optical model describing the sample is built and used to make predictions of the data. This model is adjusted until the predictions match the experimental values. The properties of the model that we may adjust include refractive index, absorption coefficient and layer thickness. Thus, we may find properties of the sample through the solution of an inverse problem.

This section is structured as follows. Firstly, the basic theory of ellipsometry is presented. Secondly, the experimental set-up is described i.e. the design of the ellipsometer itself. Thirdly, the general fitting procedure is discussed.

3.3.1 *Theory of ellipsometry*

Ellipsometry measures the change in the polarization state of light reflected off the surface of a sample. Consider polarized light incident on a sample, as in Figure 3.3.

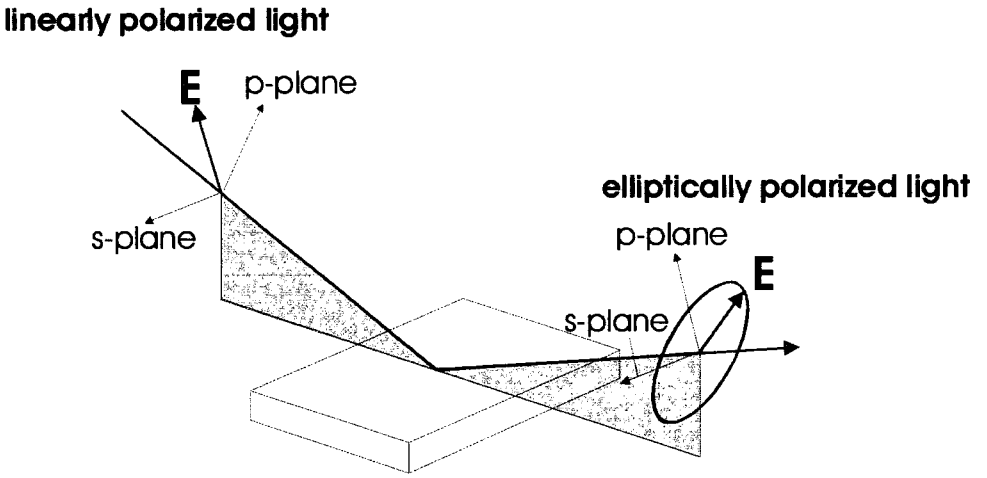

Figure 3.3: A beam of polarized light, reflected of a substrate, showing the p- and s-directions

The light can be separated into two perpendicularly polarized components as shown. One component is polarized in the plane of incidence and is called p-polarized light.

The other component is polarized in the plane of the sample and is called s-polarized light. These components have different Fresnel reflection coefficients R_P and R_S. Ellipsometry measures the ratio of these two values. This is in general complex and can be expressed in terms of an amplitude part ψ and a phase part Δ:

$$\frac{R_P}{R_S} = \tan(\psi)e^{i\Delta} \tag{3.27}$$

It is because ellipsometry measures the ratio of two values that it is a very precise and repeatable technique.

Ellipsometry can be used to determine thin film thickness and thin film optical constants. It is often possible to determine thickness and optical constants for the same film simultaneously. The ellipsometer used here was a Variable Angle Spectroscopic Ellipsometer (VASE). It is *spectroscopic* because it can perform ellipsometry measurements over a range of wavelengths, from ultraviolet to infrared. This is obviously essential where we wish to find the wavelength dispersion of the optical constants for a sample. It is *variable angle* because the angle of incidence of the light may be varied. This is useful for two reasons. Firstly, more data may be acquired from a sample. Secondly, and most importantly, the experiment may be optimized for a given sample.

3.3.2 *Experimental Set-up*

The ellipsometry measurements were made using a J.A. Woollam Co., Inc. Variable Angle Spectroscopic ellipsometer. This is an example of a rotating analyzer ellipsometer, which has the following configuration:

source → polarizer → sample → continuously rotating analyzer → detector

The source is a Xe arc lamp, which is stable and emits over the range from the UV to the NIR. The light from this source is monochromated and coupled to the input

polarizer by an optical fibre. The polarizers used are Glan-Taylor polarizers which are linearly polarized to 1 part in 10^6 and transmit light from 230 to 2200 nm. The analyzer rotates to find the polarization state of the reflected light. The ellipsometer uses a stacked detector unit consisting of silicon and InGaAs photodiodes. These are insensitive to polarization state and linear over a broad range of beam intensities.

Analysis of the ellipsometer operation can be performed using the Jones matrix formalism. Jones vectors describe the polarization of a beam of light.

$$\text{arbitrarily polarized beam: } \mathbf{E} = \begin{bmatrix} \tilde{E}_P \\ \tilde{E}_S \end{bmatrix} \tag{3.28}$$

Here, **E** describes the electric vector of a beam of polarized light, with $\tilde{E}_P$ and $\tilde{E}_S$ representing the p- and s-polarized components respectively. Linearly polarized light is written as $\begin{bmatrix} E_P e^{i\phi} \\ E_S e^{i\phi} \end{bmatrix}$ where the phase angle is identical for both components. P-polarized light and s-polarized light are written $\begin{bmatrix} 1 \\ 0 \end{bmatrix}$ and $\begin{bmatrix} 0 \\ 1 \end{bmatrix}$ respectively. Figure 3.4 shows linearly polarized light

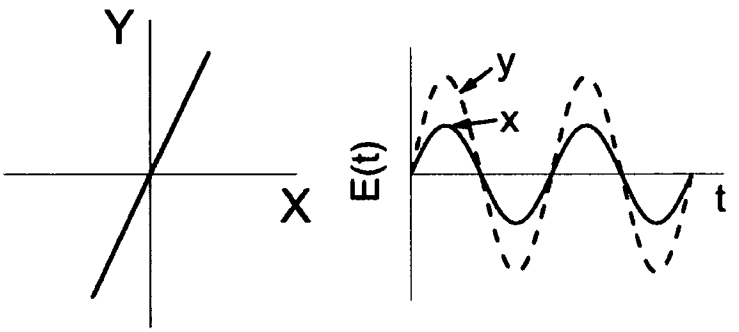

Figure 3.4: The electric vector of linearly polarized light, and the variation of its x- and y-components with time

If the two components have equal magnitude but are 90° out of phase, then the light is called circularly polarized light because in the x-y plane, the tip of the electric vector traces out a circle (Figure 3.5):

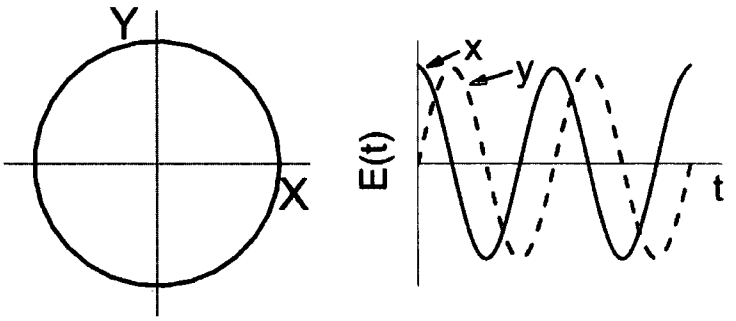

Figure 3.5: The electric vector of circularly polarized light, and the variation of its x- and y-components with time

In general, the magnitude and phase of the two components do not have to have any particular relationship, and the electric vector traces out an ellipse (Figure 3.6):

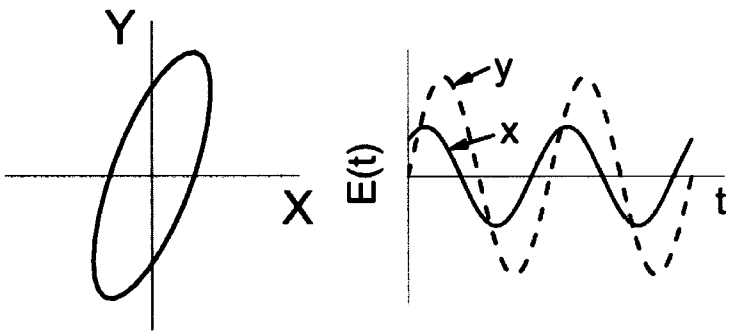

Figure 3.6: The electric vector of elliptically polarized light, and the variation of its x- and y-components with time

Since lines and circles are just special types of ellipse, all polarized light can be described as being elliptically polarized. This is why ellipsometry is so-called – the technique determines the elliptical polarization of the probe beam.

When polarized light meets an optical component, such as a polarizer or a sample, its polarization may be changed. Hence, optical components may be described using Jones matrices. These operate on the Jones vector of the incident light to give the polarization state of the resultant beam.

The intensity measured by the ellipsometer detector is proportional to the magnitude of the beam's electric field squared:

$$I \propto |E_D|^2 \tag{3.29}$$

The electric vector at the detector can be found by tracking the input beam through the components of the system:

$$E_D = [\text{Analyser matrix}][\text{Sample matrix}][\text{Polarizer matrix}][\text{Input beam}] \tag{3.30}$$

For the polarizer matrix, we first rotate the coordinate system so that the axis of the polarizer is parallel to the p-direction. Thus the beam leaving the polarizer is p-polarized. The coordinate system must then be rotated back to the p- and s- coordinates of the ellipsometer. If the angle between the polarizer and ellipsometer was P, then the beam incident on the sample will have the following polarization:

$$\begin{bmatrix} \cos P & -\sin P \\ \sin P & \cos P \end{bmatrix} \cdot \begin{bmatrix} 1 \\ 0 \end{bmatrix} \tag{3.31}$$

If the sample is isotropic and not too rough, then its Jones matrix may be written:

$$\begin{bmatrix} \tilde{R}_P & 0 \\ 0 & \tilde{R}_S \end{bmatrix} \tag{3.32}$$

with no off-diagonal elements. Finally, the beam is incident on the analyzer. The coordinate system is first rotated so that the new p-direction lies along the analyzer p-

direction. It does not need to be rotated back after transmission through the analyzer as we are then only interested in the intensity of the beam at the detector and this is independent of polarization. Writing the angle between the analyzer axis and the plane of incidence as A, the total Jones matrix for the analyzer is:

$$\begin{bmatrix} 1 & 0 \\ 0 & 0 \end{bmatrix} \cdot \begin{bmatrix} \cos A & \sin A \\ -\sin A & \cos A \end{bmatrix} \tag{3.33}$$

The total expression for the electric field at the detector is then:

$$E_D = \begin{bmatrix} 1 & 0 \\ 0 & 0 \end{bmatrix} \cdot \begin{bmatrix} \cos A & \sin A \\ -\sin A & \cos A \end{bmatrix} \cdot \begin{bmatrix} \tilde{R}_P & 0 \\ 0 & \tilde{R}_S \end{bmatrix} \cdot \begin{bmatrix} \cos P & -\sin P \\ \sin P & \cos P \end{bmatrix} \cdot \begin{bmatrix} 1 \\ 0 \end{bmatrix} \tag{3.34}$$

Which can be evaluated as:

$$E_D = \begin{bmatrix} \tilde{R}_P \cos P \cos A + \tilde{R}_S \sin P \sin A \\ 0 \end{bmatrix} \tag{3.35}$$

The intensity of the beam can be calculated to be:

$$I_D \propto 1 + \frac{\left|\frac{\tilde{R}_P}{\tilde{R}_S}\right|^2 - \tan^2 P}{\left|\frac{\tilde{R}_P}{\tilde{R}_S}\right|^2 + \tan^2 P} \cos(2A) + \frac{2\,\mathrm{Re}\left(\frac{\tilde{R}_P}{\tilde{R}_S}\right) - \tan^2 P}{\left|\frac{\tilde{R}_P}{\tilde{R}_S}\right|^2 + \tan^2 P} \sin(2A) \tag{3.36}$$

Substituting in equation (3.27) leads to:

$$I_D \propto 1 + \frac{\tan^2\psi - \tan^2 P}{\tan^2\psi + \tan^2 P} \cos(2A) + \frac{2\tan\psi\cos\Delta\tan P}{\tan^2\psi + \tan^2 P} \sin(2A) \tag{3.37}$$

which has the form of a Fourier series:

$$I_D \propto 1+\alpha\cos(2A)+\beta\sin(2A) \tag{3.38}$$

Since the analyzer is continuously rotating, the angle A is a function of time. If the detector signal is measured as a function of time, and a Fourier transform performed, then the Fourier coefficients α and β will be obtained:

$$\alpha = \frac{\tan^2\psi - \tan^2 P}{\tan^2\psi + \tan^2 P}$$
$$\beta = \frac{2\tan\psi\cos\Delta\tan P}{\tan^2\psi + \tan^2 P} \tag{3.39}$$

These equations can be solved to give ψ and Δ as a function of the Fourier coefficients and the polarizer angle:

$$\tan\psi = \sqrt{\frac{1+\alpha}{1-\alpha}}\left|\tan P\right|$$
$$\cos\Delta = \frac{\beta}{\sqrt{1-\alpha^2}}\cdot\frac{\tan P}{\left|\tan P\right|} \tag{3.40}$$

Many of the samples investigated in this chapter are anisotropic. In this case, the Jones matrix contains off-diagonal elements as follows:

$$\begin{bmatrix} \tilde{R}_{pp} & \tilde{R}_{ps} \\ \tilde{R}_{sp} & \tilde{R}_{ss} \end{bmatrix} \tag{3.41}$$

The above approach can be used again to find α and β. However, there is much more algebra involved and the expressions for α and β are considerably more complicated.

It has so far been shown how the ellipsometer finds ψ and Δ experimentally. Of course, it is not ψ and Δ that we are interested in, but rather the optical constants and thickness of the film. Their relation to the Fresnel reflection coefficients and hence to ψ and Δ can be calculated through application of Maxwell's equations.

3.3.3 *Analysis of the data*

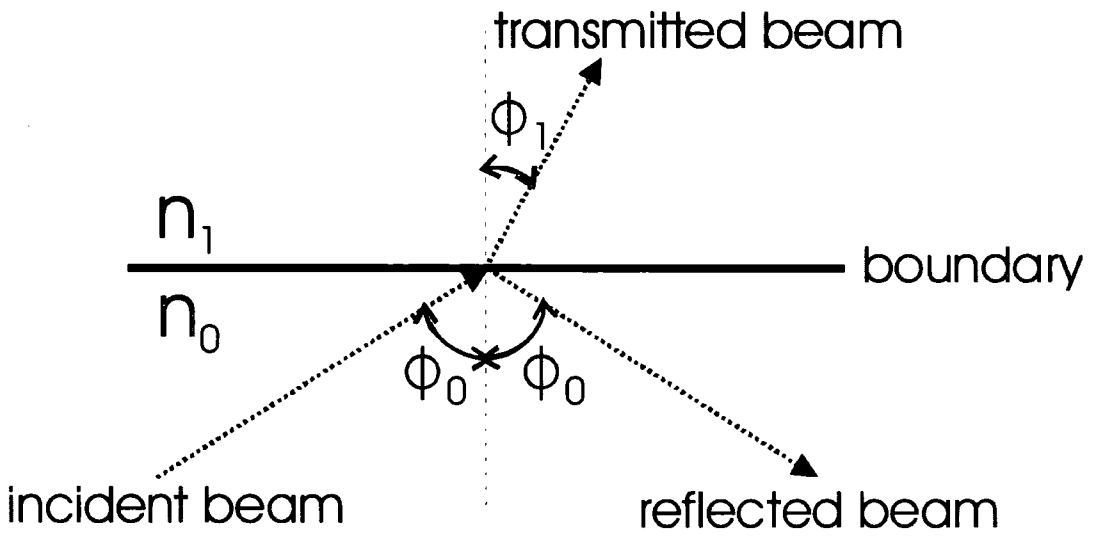

Figure 3.7: Reflection and transmission of light incident on a boundary

When a wave of light is incident on a boundary, there will be a transmitted wave and a reflected wave. The intensity of the waves that are reflected and transmitted depend upon the transmission and reflection coefficients of the boundary. These are functions of the refractive indices of the two media as well as the polarization of the incident light, which can be split up into its p- and s-polarized components, as described earlier.

It can be shown that the reflection coefficients for p- and s-polarized light are:

$$\tilde{r}_p = \frac{\tilde{n}_1 \cos\phi_0 - \tilde{n}_0 \cos\tilde{\phi}_1}{\tilde{n}_1 \cos\phi_0 + \tilde{n}_0 \cos\tilde{\phi}_1} \tag{3.42}$$

$$\tilde{r}_s = \frac{\tilde{n}_0 \cos\phi_0 - \tilde{n}_1 \cos\tilde{\phi}_1}{\tilde{n}_0 \cos\phi_0 + \tilde{n}_1 \cos\tilde{\phi}_1} \tag{3.43}$$

whereas the transmission coefficients are:

$$\tilde{t}_p = \frac{2\tilde{n}_0 \cos\phi_0}{\tilde{n}_1 \cos\phi_0 + \tilde{n}_0 \cos\tilde{\phi}_1} \tag{3.44}$$

$$\tilde{t}_s = \frac{2\tilde{n}_0 \cos\phi_0}{\tilde{n}_0 \cos\phi_0 + \tilde{n}_1 \cos\tilde{\phi}_1} \tag{3.45}$$

With $R_p = \left|\tilde{r}_p\right|^2$, $R_s = \left|\tilde{r}_s\right|^2$, $T_p = \left|\tilde{t}_p\right|^2$, $T_s = \left|\tilde{t}_s\right|^2$.

Calculating the reflection coefficients from the refractive indices is straightforward for a bulk substrate. However, for samples consisting of a film on a substrate, the situation is slightly more complicated due to reflection of the transmitted beam off the film-substrate interface, as shown in Figure 3.8.

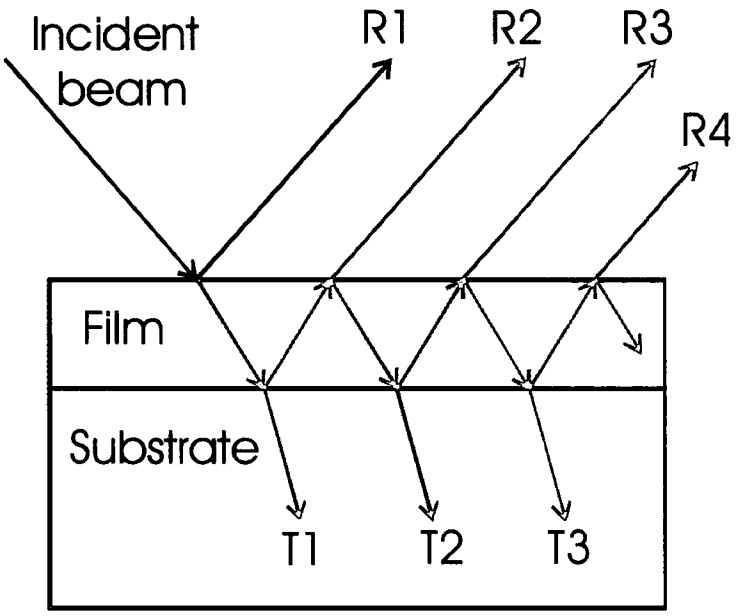

Figure 3.8: A beam of light incident on a film on a substrate, and the multiple reflections and transmissions.

These beams may be summed to find a total reflected beam, and as such find the pseudo-Fresnel reflection coefficients for the sample.

In general, we will be interested in multilayer samples, consisting of up to three films layered on a bulk substrate. The pseudo-reflection coefficients of these samples may be evaluated by summing the multiple reflections, but this becomes dramatically more computationally intensive as the number of layers increases. WVASE32 employs an alternative method involving *characteristic matrices*.[150] These matrices relate the field components at the top of the film to those at the bottom. For a multilayer sample, multiplying the matrices together in order provides valid results for the pseudo-reflection coefficients.

It has been shown how the optical constants of a sample relate to the reflection coefficients, how the reflection coefficients relate to ψ and Δ and how the ellipsometer measures ψ and Δ. This provides the pathway to finding the optical constants and layer thicknesses from the measured ψ and Δ values. This involves the solution of an inverse problem – we want to find the sample properties which result in the experimental

values that are actually measured. The approach is as follows: an optical model is built, consisting of a number of layers on a substrate and parameterized by the optical constants of the various materials and the thickness of the layers. This model is then used to predict experimental data. The model parameters are varied until the predicted data matches the experimental data as closely as possible. The quality of the match between the predicted data and the experimental data is represented by the mean-squared error, defined as follows:

$$MSE = \frac{1}{2N-M}\sum_{i=1}^{N}\left[\left(\frac{\psi_i^{\mathrm{mod}}-\psi_i^{\mathrm{exp}}}{\sigma_{\psi,i}^{\mathrm{exp}}}\right)^2+\left(\frac{\Delta_i^{\mathrm{mod}}-\Delta_i^{\mathrm{exp}}}{\sigma_{\Delta,i}^{\mathrm{exp}}}\right)^2\right] \tag{3.46}$$

where N is the number of (ψ, Δ) pairs, M is the number of variable parameters in the model and σ are the standard deviations on the experimental data points. To provide the best fit between the predicted and experimental data, this MSE must be minimized. WVASE32 performs this minimization using the Levenberg-Marquardt algorithm.

A potential problem with the fitting process is that of parameter correlation, where good fits to the data may be obtained with quite different sets of parameters. One method of circumventing this problem is to use several samples on different substrates. This provides additional constraints when the data are fit simultaneously to provide a unique fit.

3.4 Experimental procedure

The polyfluorene used was poly(9,9-diethylhexyl fluorene) (M_n = 7600 and M_w = 15000). This is a low molecular weight PF of about twenty repeat units and is particularly suitable for alignment. Its synthesis is described elsewhere.[144] Films were produced by spin-coating at 2500 rpm from a 12 mg/ml solution. The solvent used was three parts toluene to one part chloroform. This mixture was used to prevent crystallization.

For the ellipsometry measurements, the substrates used were silicon wafers with oxide layers on top. As stated earlier, we require a range of substrates to reduce

parameter correlation. This was achieved here by having a range of thicknesses for the oxide layers. The layers were formed on the silicon by wet thermal oxidation.[151] Briefly, this technique involves baking the wafers in a furnace through which water vapour is passed. An oxide grows on the surface initially then forms inwards by diffusion. This oxide was then etched back using buffered hydrofluoric acid to achieve the desired thickness.

Unaligned films were made via spin-coating directly onto these wafers, whereas the aligned films were made on wafers that had rubbed polyimide (PI) layers on top. The PI precursor was obtained from Merck KG and the layers were produced as follows: the precursor was spun onto the wafer at 2500 rpm, then heated at 85° C for 20 minutes in air to remove any residual solvent. This was followed by heating for 40 minutes at 300° C in vacuum, after which the film was allowed to cool. This layer was then rubbed unidirectionally with a rayon cloth. After spin coating the PF on this layer, the sample was then annealed at 80° C in an argon atmosphere at low pressure for 10 minutes.

The oxide layers and PI layers were characterized by ellipsometry prior to any further layers being deposited. In particular, the thickness of the oxide layers and the thickness and optical constants of the PI layers were found.

Ellipsometry measurements were made on the PF samples for at least three angles of incidence (from 50° to 70°) over the wavelength range 250-1000 nm. Seven unaligned and seven aligned samples were tested, each one having a different oxide thickness.

For direct measurements of the absorption spectra of PF, films were required to be spun on transparent substrates. Quartz discs were used as the substrates for the unaligned films. The aligned films were spun onto rubbed PI layers on indium tin oxide (ITO) glass substrates and annealed as described earlier. For convenience, LCD cells were obtained from E.H.C. Co., Ltd (Japan) and split in half to provide these alignment substrates.

3.5 Results and analysis

3.5.1 *Silicon oxide and polyimide layers*

The oxide layers were characterized first using a model in which their thickness was the only variable parameter. Literature optical constants were used for this model. Excellent fits to the data were found, with the oxide layers having thicknesses over a range of 100 – 1400 Å. The properties of the PI layers were found a procedure similar to that for the PF, which will be described in more detail later. Briefly, the thickness and refractive index were first found at long wavelengths where the PI is expected to be transparent, using a parametric function for the refractive index. Then, a point-by-point fit was used to find a first approximation to the optical constants in the absorbing region. Finally, more realistic optical constants were obtained using parametric functions. The layers were found to have a mean thickness of 338 ± 33 Å. Figure 3.9 shows an example of the calculated PI optical constants. An example of the ellipsometric data together with the fit is shown in Figure 3.10. These data were for a sample with a PI thickness of 373 Å on a silicon substrate with an oxide thickness of 618 Å.

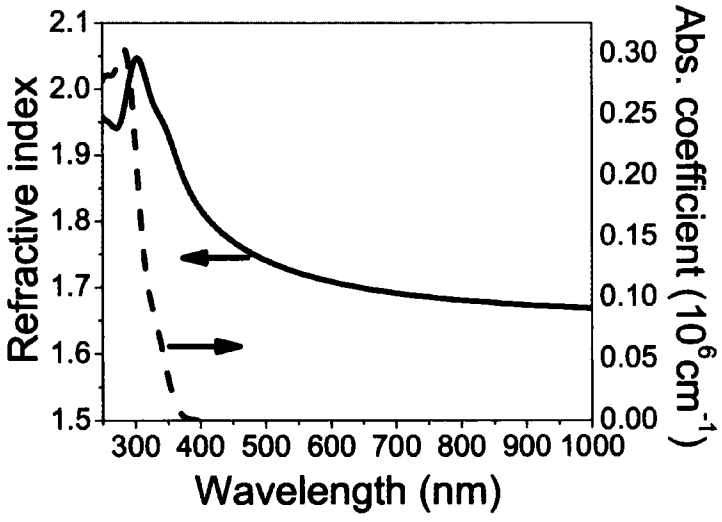

Figure 3.9: Optical constants of a rubbed polyimide film, found by ellipsometry.

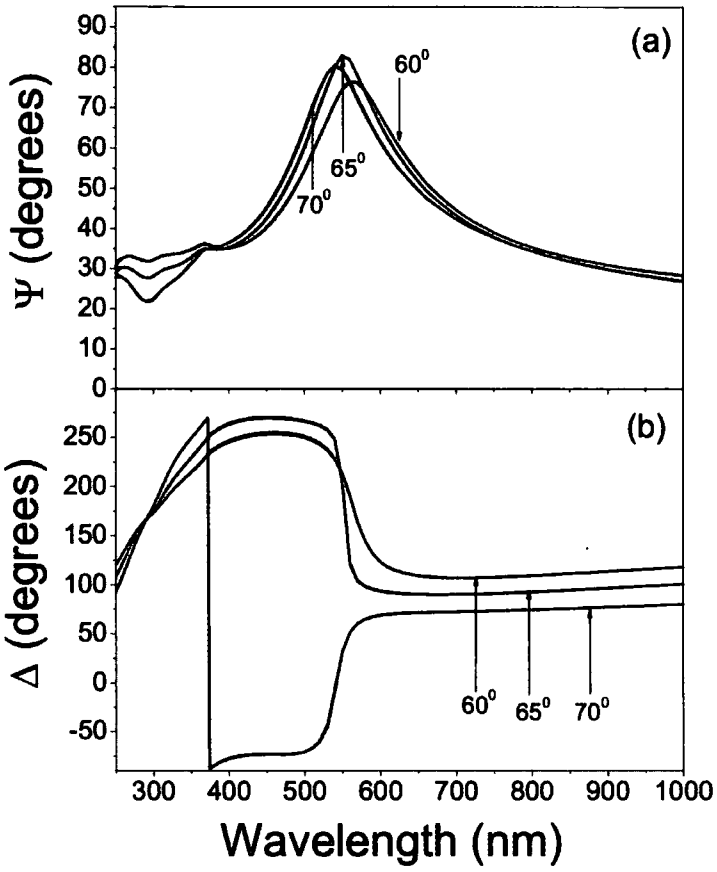

Figure 3.10: Ellipsometric data of a rubbed polyimide film on a silicon/silicon dioxide substrate (black lines) and fit from the model (red lines)

There are several points to note here. Firstly, good fits to the data were achieved using isotropic models. This is in slight contrast to previous measurements on PI, where the film was considered to consist of a bulk isotropic lower layer and a thin anisotropic top layer resulting from the rubbing process.[152] In that work, detailed anisotropic ellipsometric measurements were made at a single wavelength, allowing a more in-depth analysis. In our work, the influence of a thin anisotropic top layer is not noticeable, and the isotropic optical constants found are considered adequate for our purposes.

Secondly, it was found that better fits to the data could be obtained by allowing some non-uniformity in the layer thickness. This may correspond to some roughness

resulting form the rubbing process. The presence of surface non-uniformity is also indicated by the significant depolarization observed and is not too unexpected given the somewhat random way in which the rubbing process imparts striations on the surface of the PI. When a beam of polarized light is incident on an ideal sample, the reflected light will have a single well-defined polarization state. If the sample is non-ideal (e.g. the surface is rough, or the layers are not parallel) then the reflected beam will consist of light of different polarization states, which together form a partially depolarized beam. The VASE system used here is capable of measuring the percentage of the reflected beam not in a well-defined polarization state. A typical depolarization signal is shown in Figure 3.11.

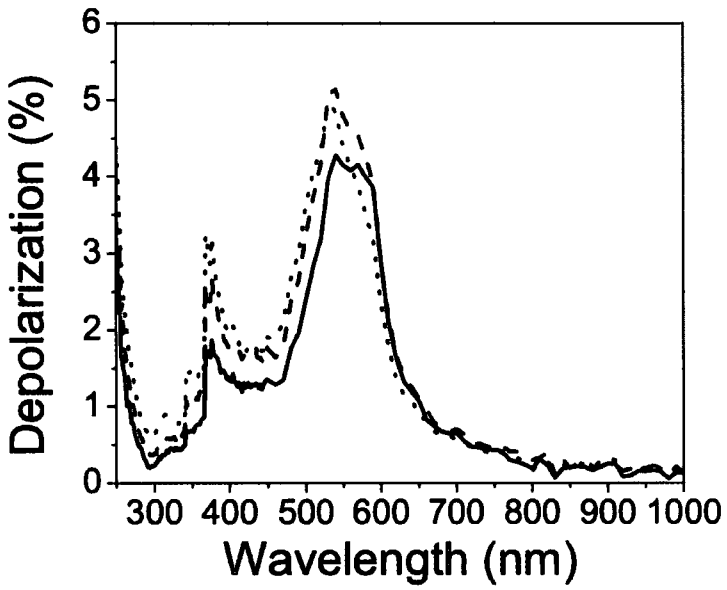

Figure 3.11: Depolarization in the ellipsometric data for a rubbed polyimide film on a silicon/silicon dioxide substrate. Angle of incidence: 60° (solid line), 65° (dashed line), 70° (dotted line).

Thirdly, it was not possible to find a single set of optical constants that would provide good fits for all the PI layers. This could also be due to the roughness/surface uniformity being different from film to film, or to slight differences in the fabrication procedure. Therefore, the optical constants were allowed to vary slightly from layer to layer within the parametric models.

3.5.2 *Unaligned polyfluorene films*

The PF was represented by a uniaxial layer of unknown thickness. The optic axis of this layer was set normal to the surface. Figure 3.12 shows a typical layer structure and Figure 3.13 shows the direction of the optic axis. An initial guess to the thickness was made from previous measurements on film thicknesses using an Tencor Alphastep profilometer.

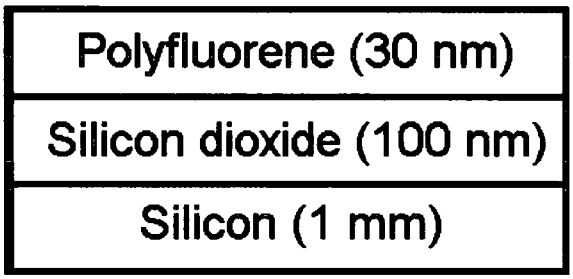

Figure 3.12: Typical layer structure for an unaligned PF sample

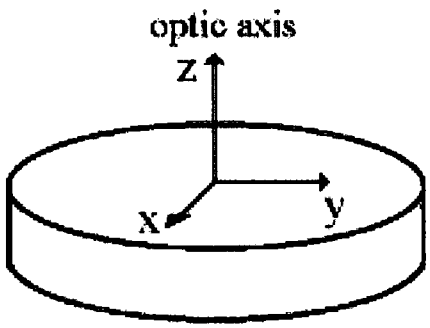

Figure 3.13: The direction of the optic axis in an unaligned PF film. The optic axis is perpendicular to the film surface. Directions x and y, parallel to the surface of the film, are arbitrary and identical

The fitting procedure was as follows. Firstly, the spectroscopic range was restricted to wavelengths above 600 nm. The absorption edge of PF is at approximately 450 nm, so in the range we were initially considering, the absorption coefficient could be confidently set to zero, reducing the number of parameters involved in the fitting. The

refractive indices n_x and n_z of this layer were then described by parametric functions of wavelength:

$$n(\lambda) = A + \frac{B}{\lambda^2} + \frac{C}{\lambda^4} \tag{3.47}$$

This is Cauchy's equation. A, B and C are variable parameters. A is the value that this refractive index will tend towards at long wavelengths, while B and C provide dispersion. The layer thickness was also set as a variable parameter. The data from the films were then fitted simultaneously using this model, subject to the constraint that the optical constants of all PF layers were identical. The thicknesses of the layers, however, were allowed to be independent.

Excellent fits to the data were achieved using this approach. Film thicknesses were found to be reasonable close to each other. A mean value of 460 ± 30 Å was found. The next step was to extend the range to the absorbing region. Having found the film thickness and the optical constants above 600 nm, these values could now be fixed. The procedure for finding the refractive index and absorption coefficient in the remaining region was as follows. The optical constants for the x- and z-directions were fitted independently, point-by-point. This means that at each data point, the optical constants themselves are varied to find the values that give the best fit to the data. This approach usually yields a very close fit to the data, but the resulting optical constants are typically not smooth functions of wavelength and may exhibit some artefacts. This point-by-point fit is therefore only used to obtain a first approximation. To find more realistic optical constants, we need to replace these by parametric functions of wavelength.

An effective method of doing this is now described. The optical constants obtained from the point by point fit are converted to real and imaginary dielectric constants. A new layer is built using a parametric function for its dielectric constants. This function will have several variable parameters in it, which are then fit to match as closely as possible the imaginary dielectric constant of the point by point fit. For polyfluorene, the

function we use is a sum of several Gaussian functions, with their amplitude, width and centre as variable parameters.

$$\varepsilon_2 = \sum_i A_i e^{-\left(\frac{E-E_i}{B_i}\right)^2} + A_i e^{-\left(\frac{E+E_i}{B_i}\right)^2} \tag{3.48}$$

Since the real and imaginary dielectric constants are linked via the Kramers-Krönig relationship, finding the imaginary part also provides us with the real part, except for a single parameter for the long-wavelength offset which is easily found.

Through this method, we can find smooth optical constants which provide good fits to the ellipsometric data. These optical constants are parametric functions of wavelength. Improvements to the optical constants can be achieved by fitting the data again, allowing the parameters in these functions to vary. The optical constants will remain smooth and realistic. Although the point-by-point fit generally achieves a lower mean square error, it is felt that these smooth optical constants are more physical and preferable.

Figure 3.14 shows the anisotropic absorption coefficients found by ellipsometry. The anisotropic refractive indices of polyfluorene are shown in Figure 3.15. This figure also shows the absorption coefficient calculated from direct measurements on an unaligned film on quartz, made using an absorption spectrometer. To calculate absorption coefficient from the optical density, knowledge of the film thickness is required. The thickness here was 388 Å, as determined by X-ray reflectivity measurements. It is seen that the results from direct measurement match those from ellipsometry very closely. The main difference is an apparent absorption tail for the direct measurement, which may be due to scattering from the sample. This would indicate that ellipsometry is a superior technique for finding absorption coefficient.

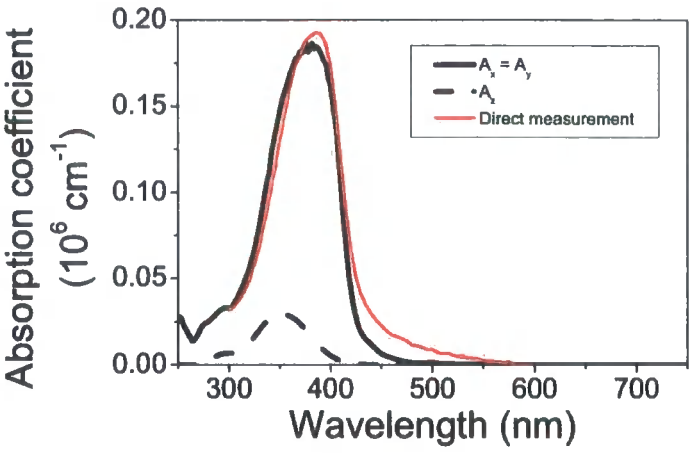

Figure 3.14: Anisotropic absorption coefficients for an unaligned PF film, found by ellipsometry (black lines). The solid line is the absorption coefficient for light with its electric vector in parallel to the surface of the film. The dashed line is the absorption coefficient for light with its electric vector perpendicular to the surface of the film. The red line is the absorption measured via a direct transmission measurement.

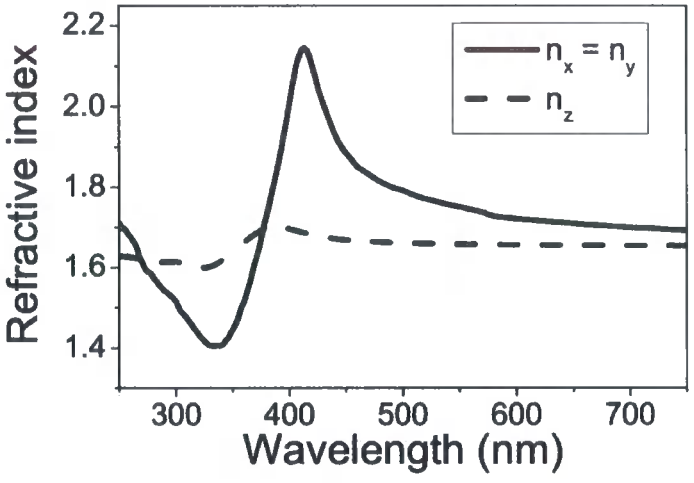

Figure 3.15: Anisotropic refractive indices for an unaligned PF film, found by ellipsometry. The solid line is the refractive index for light with its electric vector in parallel to the surface of the film. The dashed line is the refractive index for light with its electric vector perpendicular to the surface of the film.

Samples of the ellipsometric data for one unaligned film are shown in Figure 3.16, together with the fits achieved using this model. The sample had a layer structure of Si:SiO_2:PF with thicknesses of 1 mm, 45 nm, 50 nm respectively. Qualitatively, the fit

is excellent, and at most wavelengths the generated and experimental data match very well quantitatively too. At peaks and troughs in the data there are differences of a few percent, though as it is generally difficult to fit these extreme points in ellipsometric data this is not cause for concern.

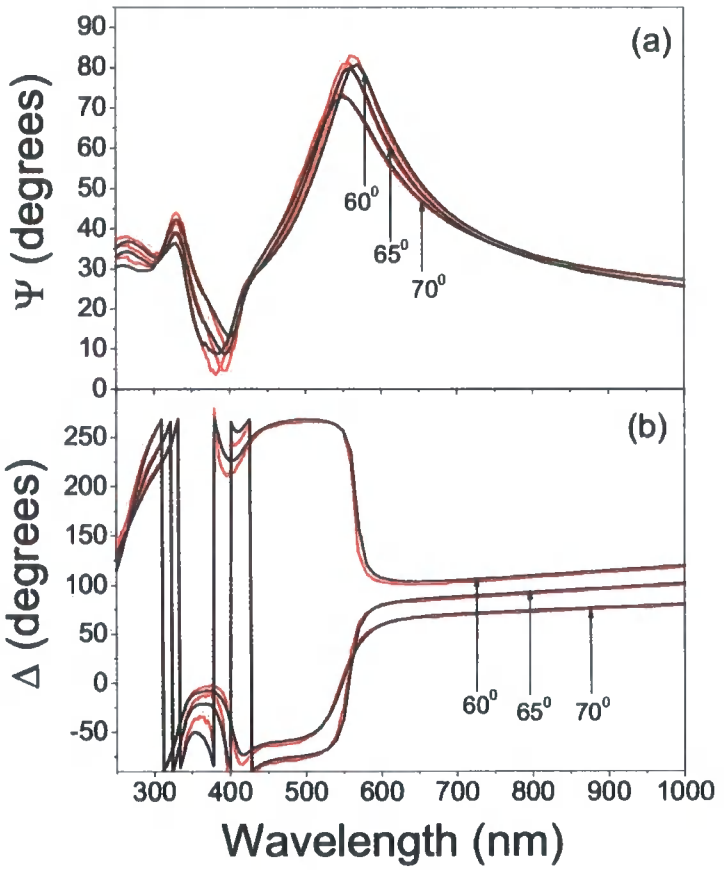

Figure 3.16: Ellipsometric data for an unaligned PF sample (black lines) and fits from the model (red lines)

3.5.3 *Aligned polyfluorene films*

The analysis of these layers was essentially the same as for the unaligned PF films. The main difference was that for the aligned films, the direction of the optic axis was set to be in the plane of the film, in the same direction as the rubbing of the polyimide. Figure 3.17 shows a typical layer structure for the aligned samples and Figure 3.18 shows the

direction of the optic axis. The optical constants found are shown in Figure 3.19 and Figure 3.20.

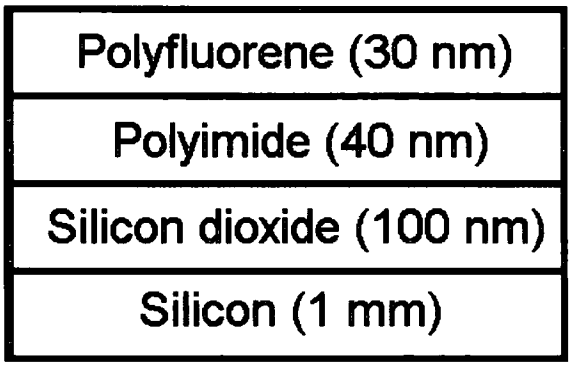

Figure 3.17: Typical layer structure for an aligned PF sample

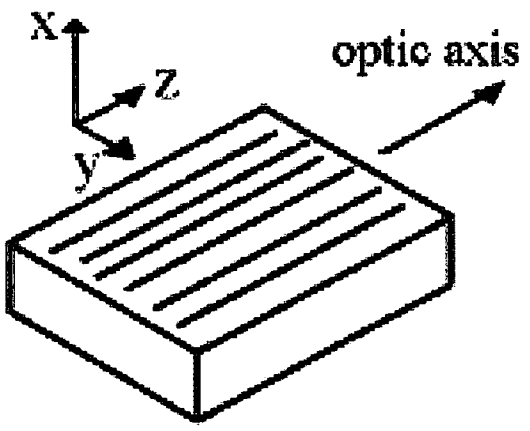

Figure 3.18: Direction of the optic axis for an aligned PF sample. The rubbing is along the z-direction.

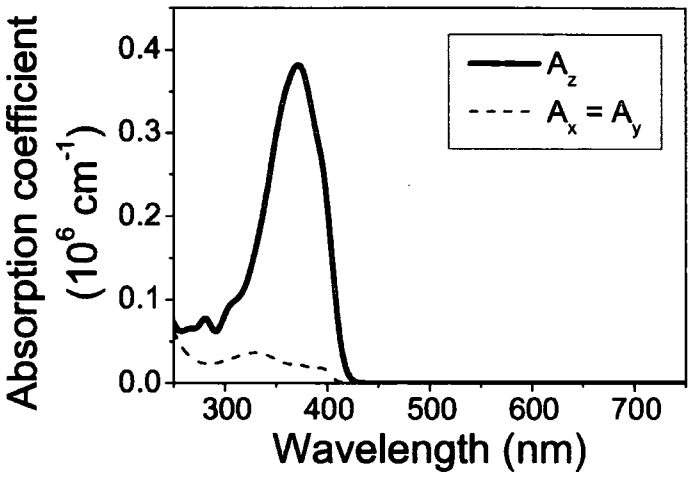

Figure 3.19: Anisotropic absorption coefficients for an aligned PF film, found by ellipsometry. The solid line is the absorption coefficient for light with its electric vector parallel to the rubbing direction. The dashed line is the absorption coefficient for light with its electric vector perpendicular to the rubbing direction.

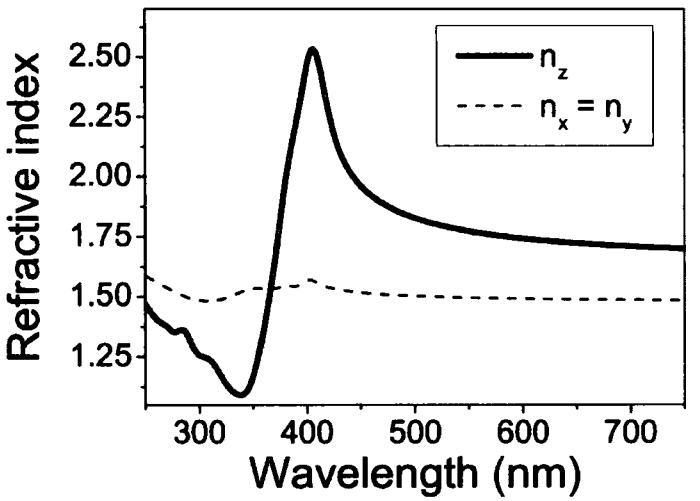

Figure 3.20: Anisotropic refractive indices for an aligned PF film, found by ellipsometry. The solid line is the refractive index for light with its electric vector parallel to the rubbing direction. The dashed line is the refractive index for light with its electric vector perpendicular to the rubbing direction.

Examples of the ellipsometric data for an aligned film are shown in Figure 3.22, together with the fits achieved. The sample had a layer structure of Si:SiO_2:PI:PF with thicknesses of 1 mm, 87 nm, 33 nm and 51 nm respectively. Depolarization in the signal was mostly low, though there were peaks of a few percent around 400 nm and 800 nm, rising up to depolarization of up to 10 % at short wavelengths where the emission from the ellipsometer's lamp is weak. A typical depolarization signal is shown in Figure 3.21.

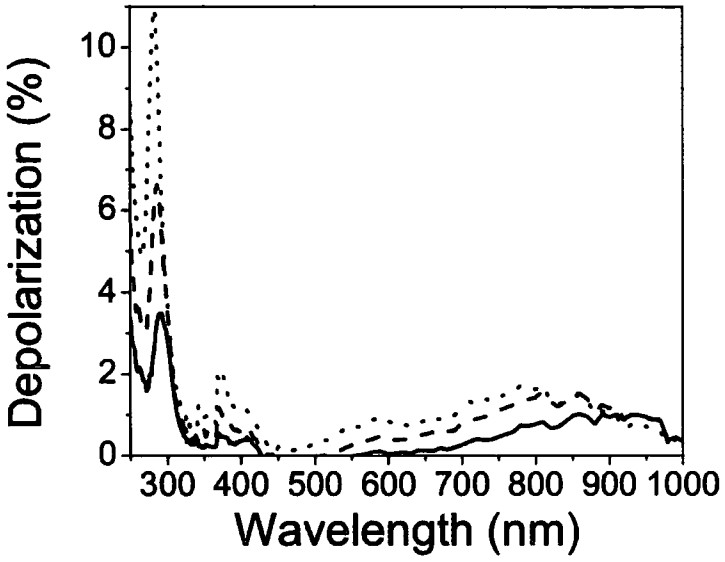

Figure 3.21: Depolarization in the ellipsometric data for an aligned PF sample. Angle of incidence: 55° (solid line), 60° (dashed line), 65° (dotted line).

Qualitatively, the generated data fits the experimental data very well. At extreme points in the data, e.g., the peaks and troughs in ψ, there are differences of up to a few percent. However, it is generally difficult to fit these extreme points in ellipsometric data and given the multilayer structure of the samples, the probable roughness of the PI layers and the fact that the PF optical constants were constrained to fit seven samples simultaneously, these differences do not seem unreasonable. This shows that the PF layers can be sufficiently described by a uniaxial system with these optical constants.

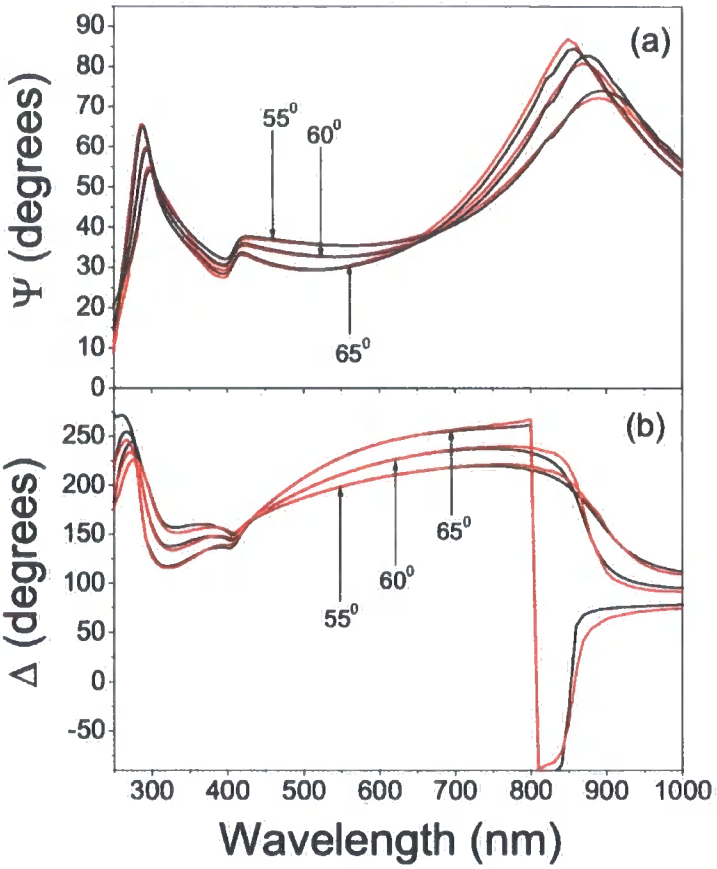

Figure 3.22: Ellipsometric data for an aligned PF sample (black lines) and fits from the model (red lines)

Direct measurements of the anisotropic absorption coefficients of aligned PF were made on aligned films on rubbed PI/ITO glass. These absorption spectra are shown in Figure 3.23. In calculating these spectra, transmission measurements were made on the samples and on bare substrates. Optical density was then calculated using the relation:

$$E = -\log\left(\frac{T'}{T^o}\right) \tag{3.49}$$

E is the optical density, T' is the transmission through the sample and T^o is the transmission through the bare substrate. This relation cannot yield the correct values since at short wavelengths, there is absorption from the substrate, and at long

wavelength much scattering. This results in apparently negative values for the absorbance at short wavelengths and non-zero baseline at long wavelengths. However, it is still evident that the spectra are similar to those found from the ellipsometric measurements.

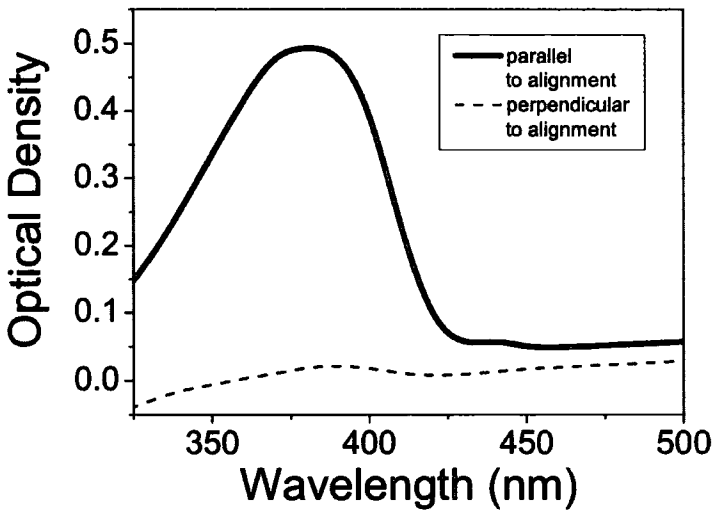

Figure 3.23: Optical density spectra for an aligned PF film on a rubbed PI/ITO/glass substrate, found by transmission measurements.

Polarized fluorescence measurements were made on aligned films deposited on silicon/silicon dioxide/PI. This was done to provide additional evidence that our films were indeed well aligned. Samples were excited with unpolarized light. The intensity of the emission polarized parallel and perpendicular to the film alignment was measured and corrected for instrument response. Results are shown in Figure 3.24. The ratio of the intensity of light emitted parallel to the alignment to that emitted perpendicularly is approximately 8:1. This confirms the high alignment of the films.

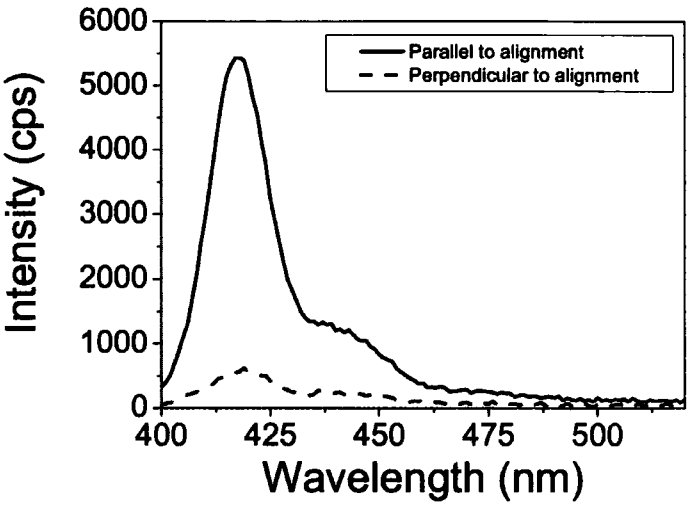

Figure 3.24: Polarized fluorescence spectra for an aligned PF film on a rubbed PI/silicon dioxide/silicon substrate. Sample was excited with unpolarized light and emission measured polarized parallel and perpendicular to the alignment direction.

3.6 Discussion

Table 1 summarizes the values of the optical constants at specific wavelengths. Considering the absorption coefficient first, it is seen that $\alpha_{x,\ unaligned}$ (absorption in the x-direction, perpendicular to the optic axis) is much higher than $\alpha_{z,\ unaligned}$ (absorption in the z-direction, parallel to the optic axis). The situation is reversed in the aligned films.

film orientation	n_x (peak)	n_z (peak)	n_x (λ= 1000 nm)	n_z (λ = 1000 nm)	α_x (cm^{-1}) (peak)	α_z (cm^{-1}) (peak)
unaligned	2.15	1.70	1.67	1.65	186560	29268
aligned	1.58	2.53	1.48	1.67	36000	382350

Table 1: Anisotropic optical constants at particular spectral positions for the unaligned and aligned PF films.

This can be explained as follows. In an unaligned film, the chains arrange themselves in a planar structure, with the planes parallel to the surface of the film.[153] Some radial alignment has been observed in polymer films, but the level of this alignment is low.[154] Therefore, light polarized in the z-direction has its electric field vector perpendicular to the polymer backbone. In the x- direction (i.e. in the plane of the film), there is a distribution of chain directions, and the electric vector may be at a range of angles to the polymer backbone. There will certainly be light which is polarized in the direction along the chain. Since the transition dipole of a conjugated polymer is expected to have a large component lying along the backbone, this will result in strong absorption for light polarized in the plane. For light polarized in the z- direction, absorption will be weak due to the small component of the transition dipole perpendicular to the chain.

In an aligned film, the chains are oriented in the rubbing direction. This is the z-direction. Light polarized along this direction will have its electric vector along the chain backbone, and hence there will be strong absorption in this direction. Light polarized in the x- or y-directions will have its electric field perpendicular to the chains, hence there will be weak absorption. This is the same situation as for light polarized in the plane in unaligned films, which is why the absorption coefficient values are so similar.

The arrangement of the chains in unaligned and aligned films is illustrated in Figure 3.25.

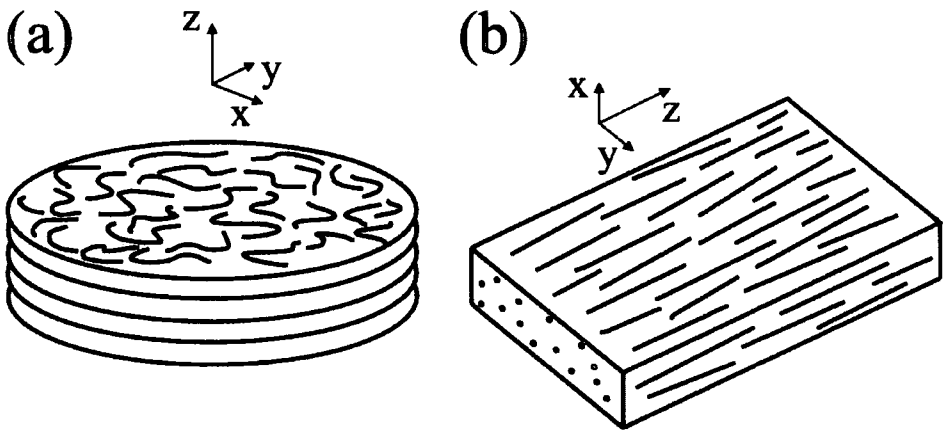

Figure 3.25: Arrangement of the chains in (a) unaligned films and (b) aligned films.

Although $\alpha_{z,\ unaligned}$ takes much the same value as $\alpha_{x,\ aligned}$, we see that $\alpha_{z,\ aligned}$ is significantly higher than $\alpha_{x,\ unaligned}$. The reason for this is that in an aligned film, light polarized in the extraordinary direction sees chains that are all oriented in the same way. All the chains have a strong transition dipole in the same direction as the electric vector. In an unaligned film, as stated before, light polarized in the ordinary direction sees a range of chain directions. The transition dipoles will not all be in the same direction as the electric vector; there will be a range of angles between the two. Therefore, the mean strength of the transition will be lower. For light polarized at an angle θ to a transition dipole moment, the strength of the transition is proportional to $\cos^2 \theta$. The mean value of $\cos^2 \theta$ over the range 0-90 degrees is 0.5. It is interesting to note that this closely matches the results presented here, since the peak value of $\alpha_{x,\ unaligned}$ is approximately half that of $\alpha_{z,\ aligned}$.

This behaviour is mirrored in the refractive index. Both unaligned and aligned films have a refractive index in one direction which is low and weakly dispersive, whilst in the other direction it is high and strongly dispersive. In both cases, it is high and strongly dispersive when the electric vector of the light has a component along the chain backbone i.e. in the direction of the transition dipole moment. This is the extraordinary direction for the aligned film and the ordinary direction for the unaligned film. The peak of the refractive index in the extraordinary direction for the aligned film is higher than that in the ordinary direction for the unaligned film, again reflecting the alignment of the transition dipole moments. Also, the unaligned film has a much lower birefringence at long wavelengths than the aligned film, which reflects its more amorphous nature.

We note similar work in this area. Zen et al have previously applied the Kramers-Kronig relations to polarized absorption spectra of aligned PF films, to estimate the dispersion of the refractive indices.[155] In the spectral range of the main PF absorption, similar values were found to those reported here.

Tammer et al have previously reported a higher ordinary refractive index and larger birefringence for amorphous polyfluorene films.[112] Their values for peak refractive index were approximately 5 % higher than those in this work, and the birefringence at long wavelength approximately twice as large. These findings were for a much higher

molecular weight polymer than was used here. We suggest that this result is due to longer chains being constrained by their rigidity to lie in plane, while it is easier for shorter polyfluorene chains to point out of the plane.

3.7 Conclusions

The optical constants of unaligned and aligned polyfluorene films have been found by spectroscopic ellipsometry. Both kinds of film exhibit uniaxial anisotropy, but with the optic axis in different directions – normal to the surface in unaligned films, and parallel to the alignment direction in aligned films. The absorption coefficient for light polarized in the alignment direction in these films is twice as high as that for light incident on unaligned films. This is because the direction of the transition dipole moment is along the chain backbone. In unaligned films there will be a distribution of these directions, and so the average transition strength in any direction will be less than for the aligned case, where the dipole moments all point approximately the same way. For light polarized perpendicular to the alignment direction in aligned films or out of plane in unaligned films, the absorption coefficient is small and the refractive index is low and weakly dispersive. The results from this chapter will be employed in the subsequent chapters of this thesis. It is also hoped that this information will be useful in the design of polarized polymer light emitting devices.

Chapter 4: Energy transfer in polyfluorene films

4.1 Introduction

The colour of emission from a polymer film may be conveniently altered by addition of a suitable dopant molecule. Energy transfer between the polymer and the dopant results in red-shifted emission, as the dopant emission will be at a lower energy than that of the polymer. Such donor-acceptor systems may be useful in fabricating organic LEDs with a range of emission colours – saturated red, green and blue emission are required for a full-colour display. Understanding of the energy transfer processes will be useful for the optimization of such devices. Addition of dopants may be looked at in another way – they can be thought of as fluorescent probe molecules, allowing investigation into the transport of excitations within the polymer layer.

This chapter describes experiments performed on polyfluorene films doped with a red dye, tetraphenyl porphyrin. The films were optically excited and fluorescence measured in steady-state. The results were analysed using the theory of Förster resonant energy transfer, modified to take excitation energy migration into account.

4.1.1 Förster transfer

The theory of fluorescence resonance energy transfer (FRET)[156] was developed by Professor Theodor Förster, who published his first paper on the subject in 1946. FRET is transfer of excited state energy from an initially excited donor molecule to an acceptor. Energy transfer occurs without the appearance of a photon. Instead, it is the result of long range dipole-dipole interactions. The efficiency of FRET is usually described in terms of the Förster radius. This is the donor-acceptor separation at which the probability of FRET is equal to the probability of de-excitation by any other pathway e.g. radiative and/or non-radiative decay. Therefore, when a donor and

acceptor are separated by the Förster radius, the rate of FRET is equal to the fluorescence decay rate of the donor.

The Förster radius can be calculated theoretically by the following equation:

$$R_0^6 = \frac{9000\kappa^2 \ln 10}{128\pi^5 n^4 N_{AV}} \varphi_{FL} \int_0^\infty \frac{f_D(v)\varepsilon_A(v)}{v^4} dv \qquad (4.1)$$

Here, φ_{FL} is the quantum yield of fluorescence of the donor, n is the refractive index of the medium, $f_D(v)$ is the normalised emission spectra of the donor, $\varepsilon_A(v)$ is the molar absorption coefficient of the acceptor. κ^2 is a configurational term to take into account the relative orientation of the transition dipole moments of the donor and acceptor.

$$\kappa^2 = \left(\cos\theta_T - 3\cos\theta_D \cos\theta_A\right)^2 \qquad (4.2)$$

where θ_T is the angle between the donor and acceptor transition dipole moments, θ_D is the angle between the donor transition dipole moment and the direction vector connecting the two molecules, and θ_A is the angle between the acceptor transition dipole moment and the same direction vector. κ^2 can take a value between 0 and 4. For a large, randomly oriented distribution of donor-acceptor pairs, the mean value is 2/3.

Since FRET takes place via a dipole-dipole mechanism, only transitions between states of the same multiplicity may occur i.e. only singlet-singlet or triplet-triplet transitions are allowed.

In Förster's derivation of equation (4.1), the refractive index was taken outside the integral because it was assumed to be independent of frequency. This is definitely not the case for conjugated polymers, which feature highly dispersive refractive indices. This is shown in Figure 4.1. (see Chapter 3 for details on how the anisotropic refractive indices were measured)

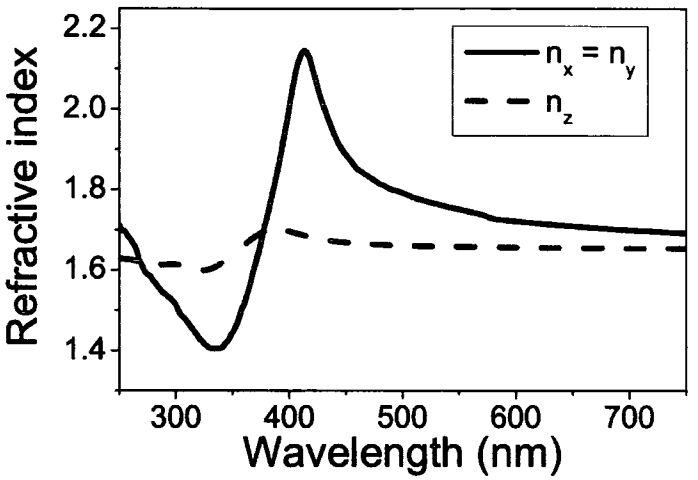

Figure 4.1: Anisotropic refractive indices of an unaligned polyfluorene film

To take this into account, a modified form of equation (4.1) is proposed, in which the refractive index appears inside the integral:

$$R_0^6 = \frac{9000\kappa^2 \ln 10}{128\pi^5 N_{AV}} \varphi_{FL} \int_0^\infty \frac{f_D(\nu)\varepsilon_A(\nu)}{n^4 \nu^4} d\nu \tag{4.3}$$

The rate of FRET can be expressed in terms of R_0, the separation R between the donor and acceptor and the fluorescence lifetime of the donor:

$$k_{FRET} = \frac{1}{\tau_D}\left(\frac{R_0}{R}\right)^6 \tag{4.4}$$

FRET also modifies the time-dependence of the donor emission. FRET is dispersive, due to the fact that transfer takes place first between donor and acceptor pairs with smaller separations. Hence, as time increases, the mean donor-acceptor separation also increases and the rate of energy transfer goes down. For pulsed excitation, the donor emission intensity decay takes the form of a stretched exponential:

$$I_D(t) = I_D^0 \exp\left[\frac{-t}{\tau_D} - 2\gamma\left(\frac{t}{\tau_D}\right)^{1/2}\right] \tag{4.5}$$

with $\gamma = C/C_0$, where:

$$C_0 = \frac{3000}{2\pi^{3/2} N_A R_0^6} \tag{4.6}$$

where τ_D is the donor fluorescence lifetime and C is the acceptor concentration. The critical concentration C_0 is defined as the acceptor concentration at which a sphere of radius R_0 contains one acceptor molecule.

4.2.1 Förster transfer applied to conjugated polymer systems

The theory of Förster transfer has often been used to describe energy transfer in systems of conjugated polymer films incorporating dopant molecules. It has been applied in various ways, sometimes with adaptations in attempts to take non-ideal conditions into account.

Even when ideal Förster transfer has been assumed, good agreement between theory and experiment has been found. Steady-state measurements have been used to find values for the Förster radius in a number of systems. The experimental values are reasonably close to the theoretical values predicted by equation (4.1). Several methods of finding the Förster radius by steady-state measurements have been employed. For example, Virgili *et al* investigated a system of PFO doped with TPP.[114] A value for the Förster radius was found by finding the dopant concentration at which the ratio of the PFO and TPP emissions matched the ratio of their quantum yields. This gave a Förster radius of 5.4 nm, slightly larger than the value of 4.8 nm expected from equation (4.1). This was attributed to other factors increasing the distance over which energy transfer can take place, for example exciton migration.

Ideal Förster transfer has also been used to analyse time-resolved data. This is generally done by fitting the donor fluorescence decay to the decay expected according to equation (4.5). The fit parameter is usually the critical concentration, which is a

function of the Förster radius. The actual concentration can be calculated from the weight concentration and molecular weight of the dopant molecules. Again, the Förster radii calculated by this method are reasonably close to the those predicted. For example, Lemmer *et al* looked at a system of PPPV doped with DCM.[157] Time resolved measurements were made on the PPPV decay as a function of DCM concentration, at low temperature. The decays were fit according to equation (4.5), taking into account the non-exponential decay of a pristine PPPV sample (because of defects). The only fit parameter was the relative concentration and thus the Förster radius. Excellent fits to the data were achieved and used to extract a value of 4.5 nm for the Förster radius, larger than the theoretical value of 3.8 nm. They suggested the discrepancy may be due to exciton delocalisation and migration, mentioning that most of this migration takes place on a ps to sub-ps timescale. It was also found that at room temperature, the decays became exponential, suggesting that the long-range energy transfer steps had been eliminated.

Other time-resolved measurement techniques have also been used. Cerullo *et al* looked at Förster transfer in films of TPP-doped PFO, using femtosecond pump-probe spectroscopy.[158] This technique monitors the state population. Pure PFO films shows photobleaching and stimulated emission below about 480 nm, and photoinduced absorption above this wavelength. Photoinduced absorption means that an excited state is absorbing – the first singlet state here. The lifetime of this state was monitored and seen to decrease for higher pulse intensities, due to bimolecular annihilation processes. In a 1.5 % w/w doped film, a positive differential transmission at 450 nm became negative after about 1 ps. This is due to the photoinduced absorption of the TPP excited state. At 420 nm, the signal showed photobleaching of the TPP Soret band. At 820 nm, the signal showed decay of the PF population. The signal at 820 nm was monitored for a range of dopant concentrations and the lifetime seen to decrease as dopant concentration increased. These decays were analysed according to a Förster model and good fits were achieved, yielding a Förster radius of 4.8 nm. This value is in excellent agreement with theory.

From the above examples, it can be seen that experimental results are reasonably well described by Förster theory. The discrepancies between theory and experiment are

attributed to inadequacies in Förster theory when it comes to dealing with conjugated polymers. Excitons in conjugated polymers are not the point dipoles assumed by Förster, but are instead delocalised over several repeat units, thus having a size comparable to the Förster radius. Also, excitons may migrate through the polymer, either along or between chains, which is not considered at all by Förster theory. These features are consistent with experimental values larger than the theoretical predictions.

More sophisticated models have been developed with these inadequacies in mind. To show the presence of exciton migration, List *et al* investigated a system of m-LPPP doped with a macromolecule, RS19.[159] They performed steady-state measurements at low temperature and room temperature as a function of dopant concentration. As dopant concentration was increased, there was a blue-shift in the host spectra which they attributed to excitons being unable to migrate to the lowest energy sites before energy transfer took place. They found that their results deviated from the prediction of Förster theory. Alternative predictions were made by solving rate equations in the steady-state, incorporating a general energy transfer rate as a fit parameter. This model was more consistent with experiment, though it did not explicitly take diffusion into account. A value of 15 nm for the diffusion length in m-LPPP had previously been calculated, and they used this value to show that in their 2 % w/w doped system, excitons could migrate about 3.5 nm. The model was applied to temperature-dependent measurements and the transfer rate found to be thermally activated with an energy of 16.5 meV. This energy may correspond to vibrational modes of the polymer, which could provide the additional energy needed for excitons to hop to higher energy segments.

The presence of diffusion has also been demonstrated by experiments in the time domain. Herz *et al* investigated energy transfer in films of polyindenofluorene doped with covalently attached perylene.[87] They performed time-resolved site-selective measurements as a function of temperature. It was found that faster energy transfer took place when excitation was into the peak of the absorption, rather than the tail. The effects were more pronounced at low temperature than at room temperature. These results suggest a strong contribution of exciton migration to the energy transfer – excitons created in the tail are localised. At room temperature up-hill migration is

possible and site-selective excitation is prevented. They found an expression relating the time-dependent ratio of the intensity of the doped to undoped polymer emission to the time-dependent energy transfer rate. Looking at the time exponent of this transfer rate reveals the nature of the energy transfer – at long times (greater than 10 ps) it is shown to be consistent with Förster transfer. At short times it deviates from this behaviour. This is suggested to be due to either deviations from the point dipole approximation, or to diffusion reducing the time-dependence of Förster transfer. As a further note, these observations would explain why previous fluorescence decay measurements fitted the stretched exponential decay of Förster theory but gave larger values for the Förster radius than expected.

The issue of exciton delocalisation has also been considered recently. Its effects on energy transfer have been investigated via computational methods. Wong, Bagchi and Rossky made quantum chemical calculations to examine the energy transfer process between PF and TPP, and compared this to the Förster energy transfer analysis.[160] They found that at long donor-acceptor separations (about 100 Å) their results matched those of the Förster analysis. At short distances, there were large deviations and the energy transfer rate varied as R^{-2} as opposed to R^{-6}. Also, the relative orientation of the donor and acceptor transition dipole moments affected the energy transfer rate in a very different way to that predicted by Förster. At long distances, the two approaches were very similar. It was also found that energy transfer could occur between 'dark states' with low oscillator strengths, contrary to the predictions of Förster. The differences arise because the point dipole approximation does not apply at donor-acceptor separations comparable to the size of the transition dipole density of the donor/acceptor. A value of between 4.0 and 4.5 nm was suggested for the Förster radius.

Similar results were obtained from calculations by Beljonne *et al.*[161] They contrasted the Förster point dipole model with a distributed monopole approach which took into account the spatial extent of the wave function along conjugated monomers. Significant differences were found for rates calculated using the two descriptions for conditions of nearest neighbour transfer, indicating that at those guest-host separations simple models based on Förster's theory are no longer applicable.

4.2 The Förster radius for PF and TPP

The emission spectrum of PF and the absorption and emission spectra of TPP are shown in Figure 4.2. It can be seen that there is a good spectral overlap between the PF emission and TPP absorption. According to equation (4.1) there should therefore be efficient FRET in this system. It was desired to compare the Förster radius predicted by this equation to that found experimentally.

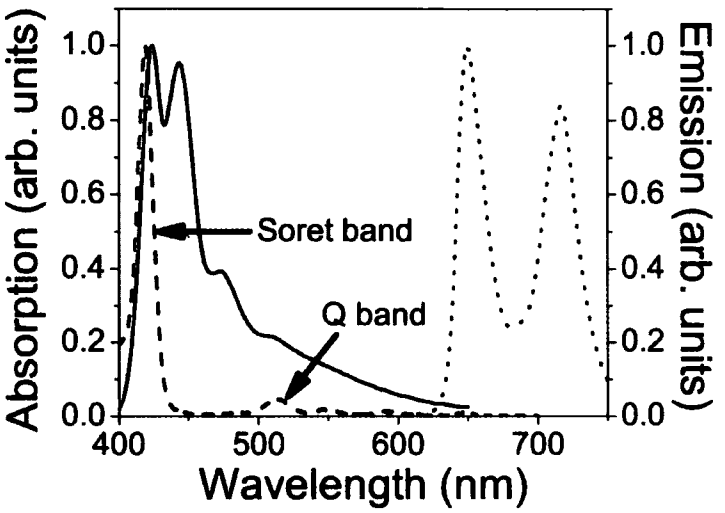

Figure 4.2: Polyfluorene emission spectrum (solid line), TPP absorption (dashed line) and emission spectra (dotted line), with TPP absorption bands labelled.

4.1.1 Experimental procedure

The polyfluorene used was poly(9,9-diethylhexylfluorene) PF2/6 (M_n = 147000 and M_w = 260000). PF2/6 and varying amounts of TPP were first separately dissolved in toluene. These PF2/6 and TPP solutions were then mixed together to obtain final solutions of 10mg/ml PF2/6, doped with 0, 0.1, 0.2, 0.4, 0.8 and 1.6% TPP by weight. Doped and undoped PF2/6 films were obtained by spin-coating these solutions onto Spectrosil discs, at 2500 rpm. This gave films of 75 ± 3nm thickness, as measured on a

Tencor Alphastep profilometer. Film thickness showed no systematic variation with dopant concentration.

Steady state emission spectra were measured using an integrating sphere inside a Fluoromax-3 spectrofluorimeter. The films were excited at 350nm, as PF2/6 absorbs strongly here but direct excitation of the TPP is avoided. The emission spectra were corrected for background and instrument response.

The photoluminescence quantum yield of this PF was found following the method of Pålsson and Monkman.[162] Its fluorescence decay lifetime was found from time-resolved measurements performed by K.S. Wong at Hong Kong University of Science and Technology, using a Ti-Sapphire laser as the excitation source and a streak camera as the detection system.

4.2.1 Results and analysis

Figure 4.3 shows the emission spectra of the PF-TPP films, without any normalisation. It is obvious that the amount of energy transfer increases with increasing dopant concentration. The intensity of the PF emission decreases as that of the TPP increases. It was desired to use this data to calculate the energy transfer rate at each dopant concentration. To find the Förster radius, the absolute rate of resonant transfer must be calculated and compared with the fluorescence decay rate of the PF. The PF was found to have a lifetime of 180 ps and a quantum yield of 0.3. Using these parameters, a PF fluorescence decay rate of 0.0055 ps^{-1} can be calculated.

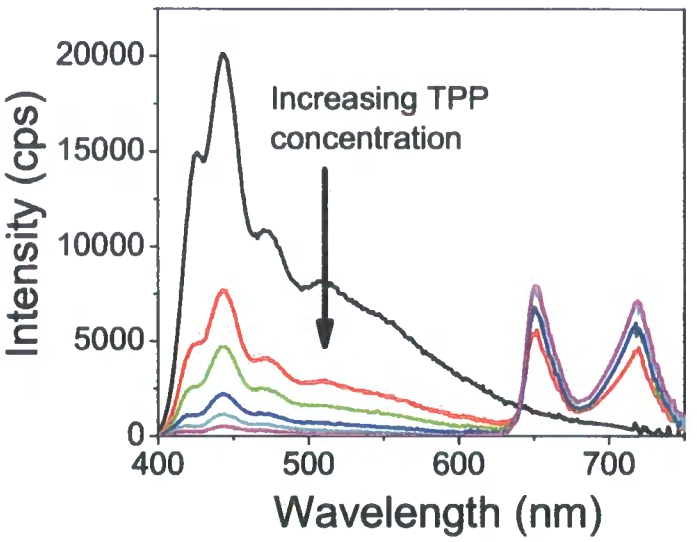

Figure 4.3: Emission spectra from a series of TPP-doped PF films.

To calculate the energy transfer rate at each dopant concentration, a simple rate equations model was employed. In the steady state, the rate equations for the populations of the ground and excited states of the polymer and dopant are as follows:

$$\frac{d[D^*]}{dt} = G - (k_{DR} + k_{DNR} + k_T[A])[D^*] \tag{4.7}$$

$$\frac{d[D]}{dt} = -G + (k_{DR} + k_{DNR} + k_T[A])[D^*] \tag{4.8}$$

$$\frac{d[A^*]}{dt} = k_T[D^*][A] - (k_{AR} + k_{ANR})[A^*] \tag{4.9}$$

$$\frac{d[A]}{dt} = -k_T[D^*][A] + (k_{AR} + k_{ANR})[A^*] \tag{4.10}$$

where G is the generation rate of excitons in the polymer, $[D]$, $[D^*]$ are the numbers of donors (polymers) in the ground and excited states, $[A]$, $[A^*]$ are the numbers of

acceptors (dopants) in the ground and excited states. k_{DR}, k_{DNR} are the radiative and non-radiative decay rates of the donor, and k_{AR}, k_{ANR} are the radiative and non-radiative decay rates of the acceptor (in ps^{-1}). k_T is the non-radiative energy transfer rate (per dopant ps^{-1}). Radiative energy transfer was neglected. This scheme is shown in Figure 4.4.

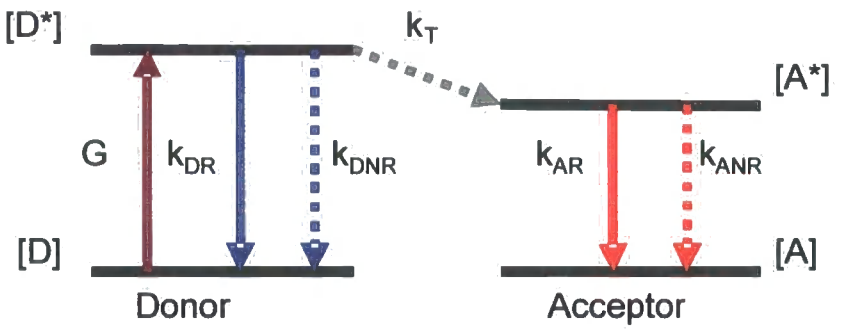

Figure 4.4: Scheme for the population and decay of and energy transfer between donor/acceptor excited states

The intensity of the emission from the polymer (in photons per unit time) is:

$$I_D = \left(\frac{d[D^*]}{dt}\right)_{emission} = k_{DR}[D^*] \tag{4.11}$$

and from the dopant:

$$I_A = \left(\frac{d[A^*]}{dt}\right)_{emission} = k_{AR}[A^*] \tag{4.12}$$

These intensities were the two quantities that could be directly measured in this experiment. In the steady state, equations (4.7) to (4.10) can be solved to give:

$$\frac{I_A}{I_D} = \frac{k_T.[A].\varphi_{QY}^{TPP}}{K_{DR}} \tag{4.13}$$

Figure 4.5 shows the energy transfer rates found by fitting this ratio to the energy transfer rate at each dopant concentration. The energy transfer rate is equal to the natural decay rate of the PF at a dopant concentration of 0.37 % by weight.

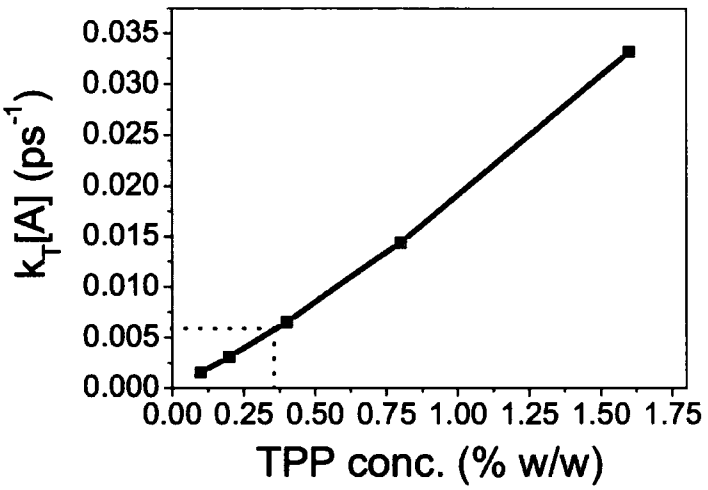

Figure 4.5: Rate of energy transfer between PF and TPP as a function of TPP concentration, calculated by solving steady-state rate equations

It is assumed that the TPP molecules are evenly distributed in a "cubic lattice" inside the polymer. The density of the PF was taken to be 1 g/cm^3. Therefore, at this dopant concentration, the molecules would have a separation of 67 Å. This separation is not the Förster radius; it is the distance between dopant molecules. At most, a polymer molecule could be $a_0/\sqrt{3}$ away from a dopant – a distance of 39 Å. This value is taken as the energy transfer distance.

Equation (4.1) predicts a value of 44 Å for the Förster radius. If the dispersive refractive index is taken into account, as in equation (4.3) then a value of 37 Å is predicted. Note that taking the dispersive refractive index into account does not make a large difference to the predicted Förster radius. Our experimental value lies between the

two values and is reasonably close to other values reported for the same system, as discussed above.

Both here and in previous work by other authors noted above, this approach gives reasonable values for the Förster radius in spite of its deficiencies. This may be due to the fact that it centres around finding the dopant concentration at which the amount of energy transfer is equal to the level of fluorescence decay of the host. This concentration is rather high and therefore the effect of exciton migration would be much diminished.

4.3 Further investigations into the validity of Förster theory

It was shown in the previous section that the experimental value for the Förster radius was close to the theoretical values predicted by equations (4.1) and (4.3). However, as discussed earlier, it is believed that FRET is inadequate to explain energy transfer in conjugated polymer systems for two important reasons.

Firstly, in Förster theory the excitons are approximated as point dipoles. This is hardly the case here as excitons are expected to be delocalised over several polymer repeat units, up to 10 nm in length. Secondly, exciton migration is expected to occur through the polymer, which could significantly increase the distance excitons can travel to reach a dopant molecule. The energy transfer is temperature dependent which is at odds with Förster transfer but thus provide evidence for exciton migration.

With this in mind, the following experiment was performed. PF films were fabricated containing a wide range of TPP concentrations. The PF was excited and the acceptor fluorescence measured at low temperature and at room temperature. Assuming that the exciton migration process is thermally activated, one might expect that at low temperature there would be little migration and so Förster transfer would dominate. At very low dopant concentrations therefore, energy transfer to the dopants might be frozen out at low temperature and only be seen at room temperature when the excitons may migrate first. At least, this experiment should be able to show how much further excitons can travel at room temperature than at low temperature.

4.1.1 Theoretical background

Although these experiments involved steady-state fluorescence measurements, it is necessary for the subsequent analysis for us to first return to the effect of FRET on the fluorescence decay profile of the donor. This was given by equations (4.5) and (4.6) above, with the donor fluorescence seen to become a stretched exponential in the presence of acceptors. These equations did not take into account exciton motion. This will now be considered.

Many attempts to address the effects of diffusion in donor-acceptor systems have been made over the last few decades. It is a complicated problem which does not in general have an exact analytical solution. Instead, approximations have to be made and the equations solved in certain limits. Interpolations may then be performed to find a general solution. Yokota and Tanimoto[163] performed an analysis using a Padé approximant method.[164] They found that the donor emission intensity decay should be further modified as follows:

$$I_D(t) = I_D^0 \exp\left[\frac{-t}{\tau_D} - 2B\gamma\left(\frac{t}{\tau_D}\right)^{1/2}\right] \tag{4.14}$$

$$B = \left(\frac{1+10.87x+15.5x^2}{1+8.743x}\right)^{3/4} \tag{4.15}$$

$$x = D\alpha^{-1/3}t^{2/3} \tag{4.16}$$

$$\alpha = R_0^6 / \tau_D \tag{4.17}$$

where D is the diffusion coefficient.

Equation (4.14) predicts the *donor* fluorescence decay in response to a *delta-function* impulse. We wish to predict the *acceptor* fluorescence in *steady-state* as a function of acceptor concentration. To this end, we first find the steady-state donor fluorescence by convoluting equation (4.14) with a step function for each value of C.

Then, the energy transferred to an acceptor at concentration C will be proportional to the difference between the donor fluorescence in a pure sample and that in the doped sample:

$$F_{acceptor} \propto F_{donor}^{pure} - F_{donor}^{doped} \tag{4.18}$$

A comment needs to be made on this method of convoluting solutions for individual delta functions. The response is actually non-linear due to the filling up of nearest neighbours, as mentioned earlier. Therefore, one might not expect our approach to be valid. However, we believe it represents a close approximation to the actual solution for the following reasons: there exists an analytical solution for the steady-state donor fluorescence in the absence of diffusion i.e. for D = 0. This is given by[165]:

$$\frac{F_{donor}^{doped}}{F_{donor}^{pure}} = 1 - \sqrt{\pi}\gamma \exp\left(\gamma^2\right)\left[1 - \mathrm{erf}\left(\gamma\right)\right] \tag{4.19}$$

Comparing the predictions of this equation with those from our model for D = 0, we find almost identical results. This can be seen in Figure 4.13 below. No similar analytical solution exists predicting steady-state fluorescence in the presence of diffusion. However, diffusion is expected to diminish the effect of the filling up of the nearest neighbours, given that it increases the distance that the excitons can travel: the density of acceptors a distance R from a donor increases as R^2. Therefore since the model here gives a good match to the analytical solution in the absence of diffusion it must be expected to yield at least as good matches in the presence of diffusion. It is also noted that Gösele, Hauser, Klein and Frey[166] investigated exciton diffusion and found similar expressions to Yokota and Tanimoto. In their paper, they noted that the formulae found could be extended to acceptor fluorescence and to any shape of excitation by simple linear convolution.

The critical concentration for this system was calculated as follows. The PF density was taken to be 1 g/cm^3. Dopant concentrations are measured in % w/w, therefore the mass of dopant per volume can be calculated. The molecular weight of TPP is 614, so

the dopant concentration in molecules/cm^3 can be found. R_0 is taken as 4.25 nm (from the quantum chemical calculations of Wong, Bagchi and Rossky), and the volume of a sphere of this radius calculated. Thus, the critical concentration of one acceptor per "Förster sphere" is found at a weight concentration of 0.57 %. From this we can now calculate concentration in units of critical concentration for all the samples.

4.2.1 Experimental procedure

The PF used in this experiment was poly (9,9-diethylhexyl fluorene). (M_n = 7600 and M_w = 15000). This is a low molecular weight PF. Films were prepared by spin-coating PF from a 10 mg/ml solution, with a solvent of three parts toluene to one part chloroform. This mixture was used to prevent crystallization. For making doped samples, solutions were prepared by mixing a PF solution with TPP solutions in appropriate concentrations. Films of the following concentrations were fabricated: 0 %, 0.001 %, 0.005 %, 0.01 %, 0.03 %, 0.05 %, 0.1 %, 0.5 %, 1 %, 1.5 %, 2 % and 4 % w/w. For measuring the photoluminescence quantum yield (PLQY) of TPP, a film of TPP in an inert Zeonex matrix was fabricated. TPP and Zeonex were dissolved in chloroform, at a Zeonex concentration of 50 mg/ml, and a TPP:Zeonex weight ratio of 1:2000.

The fluorescence lifetime of a pure PF film was found using a time-correlated single photon counting system, as described in Chapter 2.

Steady-state photoluminescence measurements were made using a Jobin-Yvon Fluoromax spectrofluorimeter. For the temperature-dependent measurements, samples were mounted in a closed-cycle helium cryostat. Here, samples were excited through the substrate and emission collected from the front-face at an angle of 45°. It was desired to record total luminescence over all angles, and to this end the spectra for all samples were also measured using an integrating sphere. These spectra were compared to those found using the cryostat. A correction factor was found so that spectra measured at any temperature in the cryostat could be rescaled to find the spectra as if it were measured in the integrating sphere. Both emission and excitation spectra were recorded. For the emission spectra, samples were excited at 380 nm, at the peak of the

PF absorption. For the excitation spectra, emission was recorded at two wavelengths – 440 nm (the peak of the PF emission) and 650 nm (the peak of the TPP emission). The excitation light had a bandwidth of 1.5 nm.

The room temperature PLQY of TPP was measured by mounting the TPP-Zeonex film in the integrating sphere. The film was then mounted in the cryostat and emission intensity measured as a function of temperature. The results were then scaled according to the room temperature PLQY to calculate a temperature-dependent PLQY for TPP.

4.3.1 Results and analysis

The decay of the PF fluorescence in the TCSPC experiment is shown in Figure 4.6. The best fit was achieved with a bi-exponential decay. It is typical for polymer films to exhibit non-exponential decay due to energy transfer to defects.[167] For the purpose of our analysis however, a single decay time is required. The PF fluorescence decay could be well approximated by a single decay time of 280 ps.

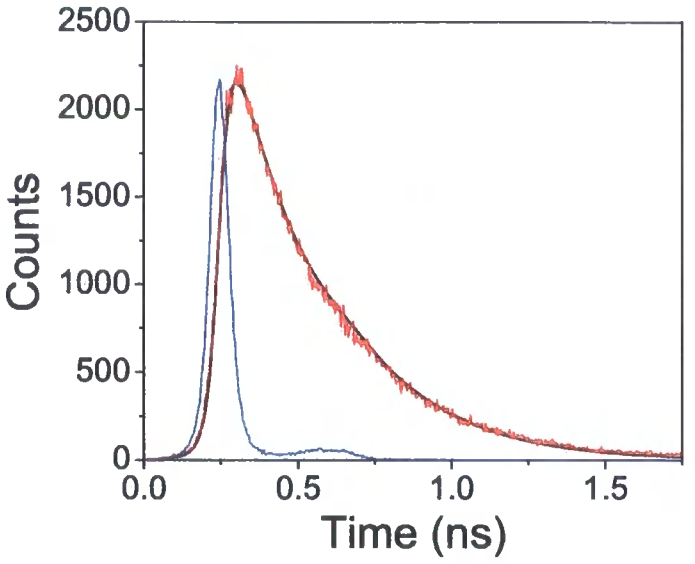

Figure 4.6: Laser pulse profile (blue line), PF fluorescence decay at 440 nm (red line) and convolution of an exponential decay, lifetime 280 ps, with the laser pulse (black line)

The TPP was found to have a room temperature PLQY of 0.08. This is slightly lower than values reported in the literature and may be due to some scattering off the sample in the integrating sphere. It is unlikely to be due to molecular aggregation since such a low concentration of TPP was present in the TPP-Zeonex film. The absolute value is in any case unimportant here – it is the temperature dependence that is of consequence. The intensity of the TPP emission was found to decrease linearly as temperature was increased. This is shown in Figure 4.7. It was assumed here that that TPP absorption spectrum is independent of temperature. If this is not the case then the TPP PLQY is not directly proportional to emission intensity. This would not, however, affect the subsequent analysis.

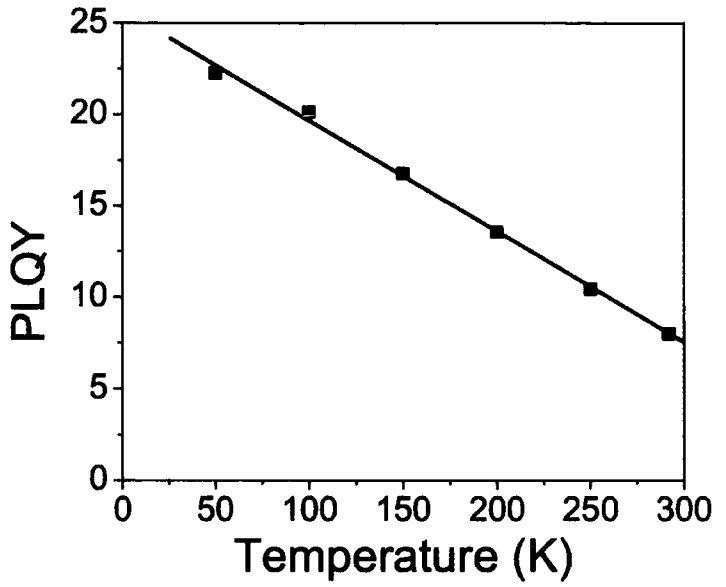

Figure 4.7: Photoluminescence quantum yield of TPP in a Zeonex matrix, as a function of temperature

Emission spectra from the 0.05 % w/w doped sample were measured from 15 K to 300 K. Figure 4.8 shows the integrated TPP emission from this sample as a function of temperature. The emission has been scaled according to the temperature dependent PLQY of Figure 4.7 such that it represents the amount of energy transferred to the dopant from the polymer. The TPP emission appears to be thermally activated, rising quickly with temperature above ~150 K. Below this, it is basically independent of temperature. This implies that at low temperature, the excitons' motion is not thermally assisted.

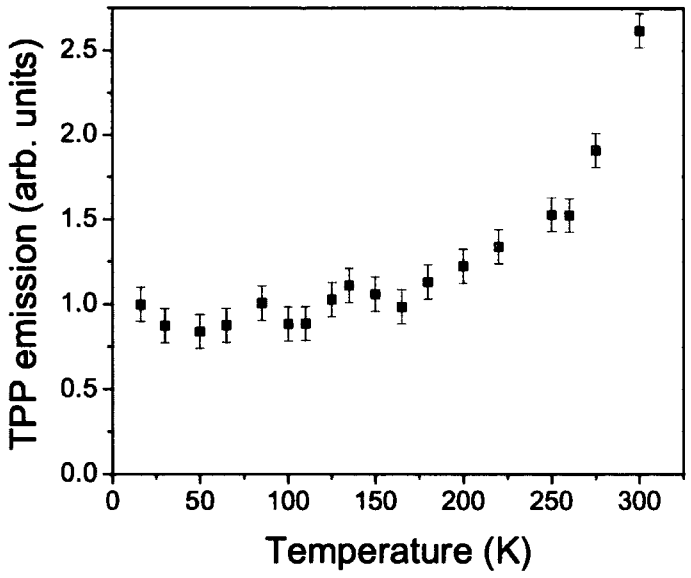

Figure 4.8: Intensity of TPP emission from a 0.05 % w/w TPP-doped PF film, where the PF was excited, as a function of temperature

It should be noted that equation (4.1) states that the Förster radius is proportional to the PLQY of the donor. The PLQY is dependent upon temperature, decreasing as temperature increases. Therefore, one might expect that the Förster radius is also temperature dependent and that this might be responsible for the results observed in Figure 4.8. This is not the case for several reasons. Firstly, if PLQY decreases as temperature increases, then so does the Förster radius. This would mean that energy transfer would become *less* efficient at higher temperatures. This is not observed. Also, the origin of the temperature dependence needs to be considered. It is believed to be a result of migration to keto defect sites, where the PL is quenched.[142] The PLQY in equation (4.1) is the intrinsic PLQY, in the absence of energy transfer to acceptors, and is therefore expected to be independent of temperature.

Figure 4.9 to Figure 4.12 show examples of the emission spectra from PF samples containing a range of TPP concentrations at low temperature and room temperature.

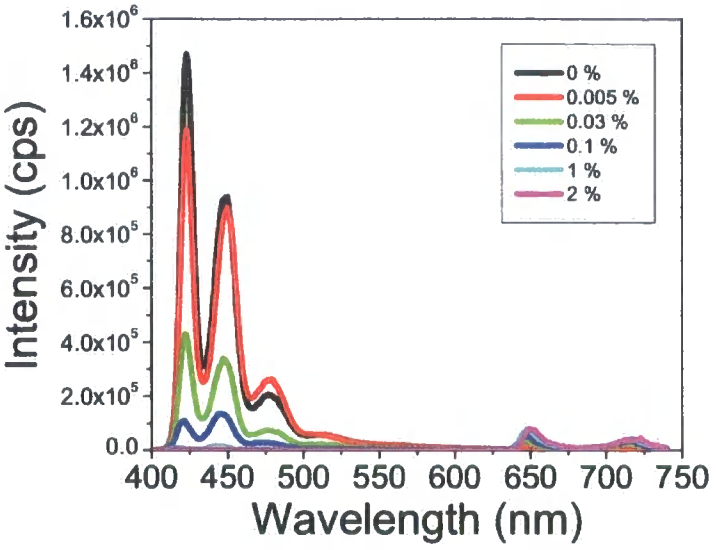

Figure 4.9: Low T (15 K) emission spectra from a series of TPP-doped PF films

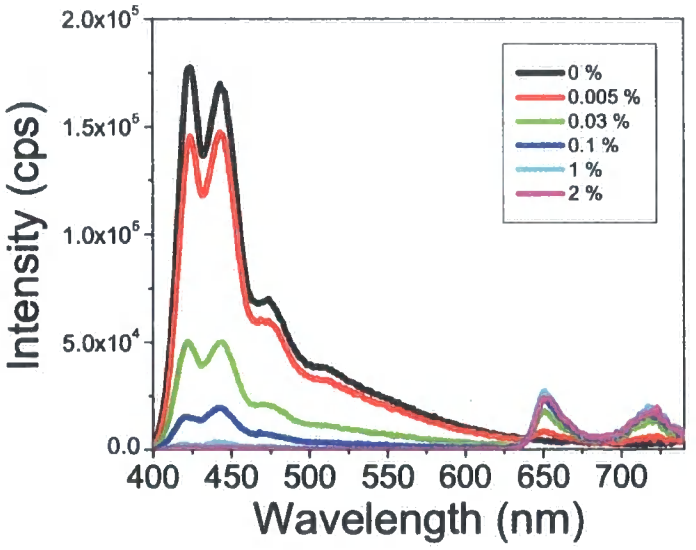

Figure 4.10: Room T emission spectra from a series of TPP-doped PF films

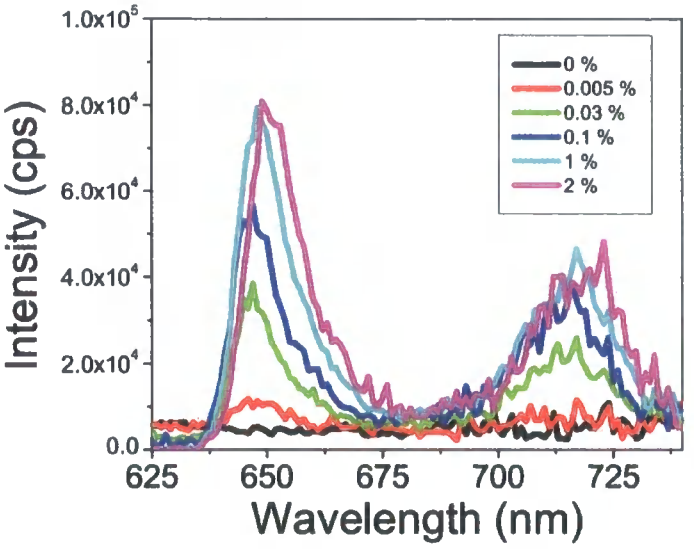

Figure 4.11: Low T (15 K) TPP emission spectra from a series of TPP-doped films

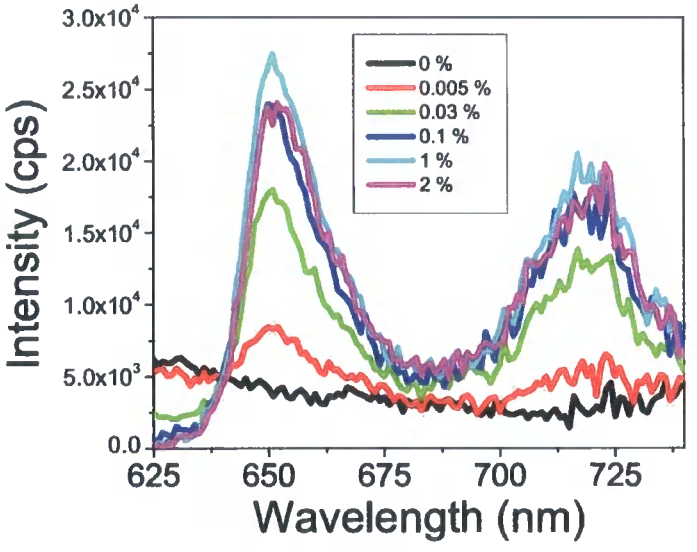

Figure 4.12: Room T TPP emission spectra from a series of TPP-doped films

These results were used to find the TPP intensity as a function of dopant concentration at low temperature and room temperature. As can be seen in Figure 4.11 and Figure 4.12, the tail of the PF emission overlaps somewhat with the TPP emission.

This is obviously more important at low dopant concentrations and it was necessary to deconvolute the two components. This was done by normalising all the spectra to the 0-1 PF emission peak. The spectrum from the pure PF sample was then subtracted from the spectra of the doped samples. The spectra were then returned to their original scale, with the result that only the dopant emission remained.

Figure 4.13 shows the integrated TPP emission intensity versus dopant separation. Dopant separation was calculated from concentration by assuming the dopants to be arranged in a simple cubic lattice. (This figure is essentially a plot of dopant emission versus dopant concentration; it is not a plot of energy transfer efficiency versus donor-acceptor separation) The emission is normalised to the emission of the 1.5 % w/w sample. Above this concentration, TPP emission actually decreases, which may be due to aggregation of the dopant molecules.

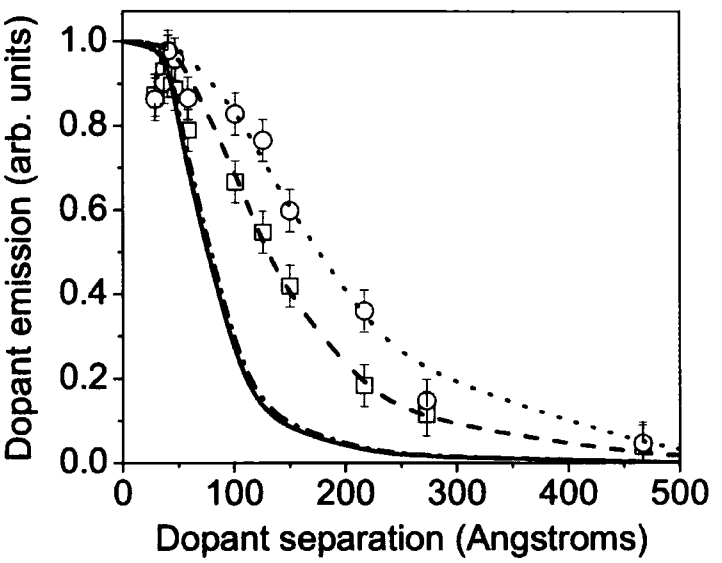

Figure 4.13: TPP emission intensity as a function of dopant separation in a series of TPP-doped PF films. Squares show emission intensity at low T. Circles show emission intensity at room T. The solid line, dashed line and dotted lines show fits to the data from the Yokota-Tanimoto model incorporating exciton diffusion, for diffusion coefficients of 0 nm^2/ps, 0.43 nm^2/ps and 1.44 nm^2/ps respectively. The dash-dot line is the prediction for steady-state acceptor fluorescence according to normal Förster theory

Three lines calculated using equations (4.14) to (4.18) are also shown on the plot. Each line was calculated for different values of D. The solid line is for D = 0 nm^2/ps, i.e. pure Förster transfer with no exciton diffusion. This line differs greatly from the experimental data, showing that the transfer process cannot be Förster transfer alone. Also shown (dash-dot line) is the prediction for steady-state acceptor fluorescence according to equation (4.19). As mentioned earlier, this is very close to the fit predicted by our model for D = 0 nm^2/ps. The dotted line and the dashed lines are best fits to the low temperature and room temperature data, with D as the only variable parameter. D values of 0.43 +/- 0.15 nm^2/ps and 1.44 +/- 0.25 nm^2/ps were found respectively. The PF fluorescence lifetime was 280 ps, so using the relation $x_{diff} = (D_0 \tau)^{0.5}$ gives us a low temperature diffusion length of 11 +/- 2 nm and a room temperature diffusion length of 20 +/- 2 nm.

This tells us several things. Obviously, it confirms that excitons are more mobile at room temperature than at low temperature. However, even at low temperature, the excitons are not completely immobilized. The non-zero diffusion at low temperature may be due to the fact that the molecules were excited at 380 nm (3.27 eV), some way above the absorption band edge of the PF. One model of exciton migration describes diffusion taking place in an inhomogeneously-broadened density of states (DOS).[51,168] An exciton is created with an initial energy dependent upon the excitation energy, then undergoes downhill migration through the DOS. This can observed as a red-shift in the emission with time. The transport is dispersive, as there are fewer and fewer sites of lower energy for the exciton to migrate to. At elevated temperatures, the molecular vibrations cause segmental site disorder, promoting uphill hopping and reducing the irreversibility of the migration process. Previously, a localisation energy of 2.93 eV (424 nm) has been found in PF – excitation below this energy results in the creation of trapped excitons, as there are no sites of lower energy within range to which they can hop.

Figure 4.14 shows the TPP emission as a function of excitation energy for one of the samples: 0.001 % w/w. No differences can be seen for excitation over the entire wavelength range i.e. no effects due to a localisation energy were observed. There are several possible explanations for this. Firstly, the optical density of the PF is extremely

low at wavelengths corresponding to energies below the localisation energy. Steady-state experiments performed using a commercial spectrofluorimeter may be unlikely to reveal such effects. Secondly, the absorption of the TPP itself is in the same location as the localisation energy of the PF. This could obscure the results here.

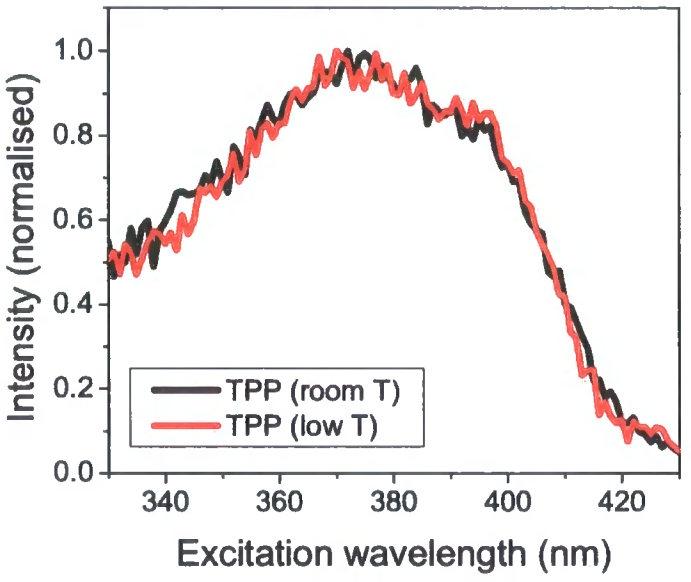

Figure 4.14: Excitation profile of a 0.001 % w/w TPP-doped PF film at low T and room T. Emission was measured at 650 nm.

Another note to make with reference to the migration of excitons through the density of states is that the red-shift in the emission will result in a change in the overlap between the PF emission and TPP absorption. This in turn will result in a time-dependent Förster radius. This might be expected to make the use the steady-state PL measurements to resolve the exciton dynamics inaccurate. Meskers et al found that in the most extreme case there is a red-shift in the PL spectra of approximately 0.05 eV at low temperature and 0.04 eV at room temperature.[51] The effect of this on the theoretical Förster radius was calculated using a red-shifted PF photoluminescence spectra in equation 1. It was found that at low temperature, R_0 decreases by less than 4 Å and at room temperature by less than 3 Å. New diffusion lengths were calculated using these adjusted values in

our model, to evaluate the effect of a variable Förster radius. Diffusion lengths of 12.2 nm at low temperature and 21.6 nm at room temperature were found.

These values were calculated using the most extreme change in Förster radius and yet they are both still within the error of our previous measurements. Obviously, the effect will not be as large as this - the relaxation takes place over the exciton lifetime and for much of this time the red-shift will be smaller. Therefore, relaxation and red-shift does not significantly affect the calculated values of diffusion length here.

The non-zero diffusion at low temperature is therefore attributed to migration to PF segments of lower energy. It is worth noting that the low temperature diffusion length of 11 nm is not much larger than the persistence length of PF – approximately 7 nm.[72] The conjugation length has also been estimated by Klaerner and Miller just over 8 nm.[73] The non-zero diffusion length may be a representation of the delocalisation of the exciton.

These results should also be discussed with relation to the observation of Herz et al[87] that the energy transfer rate is time-dependent, that diffusion may take place within the first 10 ps and after that time the energy transfer tends to that of Förster transfer. The analysis presented here assumes a time-independent energy transfer rate which is therefore inconsistent with their findings. The two approaches cannot be perfectly reconciled and given that information is lost in steady-state measurements, one would have to yield to the more accurate time-domain measurements. What does this mean for the model here? It describes the data well and so may still have some validity. One possibility is that the diffusion is averaged out in this model, and that diffusion lengths found are reasonably accurate even is the diffusion coefficient is not. It is also conceivable that the model is applicable in the low and room temperature limits; at low temperature the diffusion coefficient may represent delocalisation of the exciton, while at elevated temperatures thermally-activated hopping means diffusion still occurs.

4.4 Conclusions

Performing steady-state fluorescence measurements on doped conjugated polymer films at room temperature and analysing the results with a simple rate equations model yields a value for the Förster radius close to that predicted by theory and quantum

chemical calculations. As a first approximation to describing the energy transfer process, this is a reasonable approach. However, it neglects important factors and is therefore insufficient. It has been shown here that the energy transfer process is definitely not Förster transfer alone, even at low temperatures where exciton energy migration might be expected to be frozen out.

Proper analysis of the energy transfer process requires taking the exciton migration into account. This has been performed here following the model of Yokota and Tanimoto, who derived an expression to predict donor fluorescence decay in the presence of an acceptor when diffusion takes place. This expression was modified to predict acceptor fluorescence in steady state such that it could be applied to our results. At room temperature, an average migration distance of 20 +/- 2 nm was found. At low temperature, the migration distance was found to be 11 +/- 2 nm. This non-zero diffusion coefficient is likely due to the polymer being excited above the localisation energy, or it may be a representation of the fact that the exciton is delocalised over a polymer segment.

Chapter 5: Fluorescence anisotropy of polyfluorene films

5.1 Introduction

This chapter is about measurements of fluorescence polarization anisotropy of polyfluorene films. Unaligned and aligned, pure and doped films were investigated. Polarization anisotropy measurements provide another way to investigate energy transfer processes in these systems. Firstly, the polarization of light emitted by a molecule is parallel to its transition dipole moment, which in polyfluorene lies approximately along the chain. Energy transfer to chains lying in different directions will result in emission of light of a different polarization. Hence, the depolarization of the fluorescence signal is related to exciton migration. Secondly, Förster transfer to dopant molecules depends on the relative orientation of the transition dipole moments of the donor and acceptor. Polarization anisotropy measurements on doped systems might therefore yield some information about this orientation.

Besides processes on the molecular level influencing the polarization of the emission, optical effects – in particular the transmission of light at material boundaries – also play a part. This needs to be considered for proper analysis of fluorescence anisotropy data.

This chapter is structured as follows. The basic theory of polarization anisotropy is first presented. Then, the results from Chapter 3 are used to investigate changes in polarization at film surfaces and the effect on anisotropy measurements. This is followed by a description of some of the characteristics of fluorescence anisotropy of pure unaligned and aligned films. Finally, fluorescence anisotropy measurements of doped polyfluorene films are presented and discussed.

5.2 Background

The theory outlined in this background has been taken from several textbooks, which are listed in the references.[56,169,170] It is presented here to provide a framework for the interpretation of the experiments.

5.2.1 *Transition dipole moments*

The absorption of polarized light by a molecule depends on its orientation. The simplest quantity describing this dependence is a vector defining a direction within the molecule. A complete description requires tensors of higher rank, but a vector is adequate here. This vector is called the transition dipole moment. The strength of absorption of polarized light by a molecule is proportional to $\cos^2\theta$, where θ is the angle between the transition dipole moment and the electric vector of the light.

In conjugated polymers, it is expected that the electric transition dipole lies generally along the chain backbone. It was shown in Chapter 3 that aligned films of polyfluorene exhibit strongest absorption along the orientation direction. However, Raman anisotropy measurements on aligned polyfluorene films have shown that the transition dipole moment does have an off-axis component.[171]

The light emitted by a molecule is also polarized. The direction depends upon the emission transition dipole moment, which may or may not lie along the same direction as the absorption transition dipole moment.

5.2.2 *Absorption dichroism*

Absorption dichroism measurements have already been presented in Chapter 3 of this thesis. They provide a straightforward way of assessing the degree of alignment of a sample. Basically, a normal absorption measurement is made but the incident light is polarized parallel and perpendicular to the orientation direction of the sample. The dichroism is the ratio of the absorption coefficients:

$$D = \frac{A_{\parallel}}{A_{\perp}} \tag{5.1}$$

In an unaligned sample of course, the dichroism will be zero.

5.2.3 *Fluorescence anisotropy*

Fluorescence anisotropy measurements provide more information than absorption anisotropy because two light beams are involved. In a general fluorescence anisotropy experiment, the procedure is as follows. A polarizer (the excitation polarizer) is placed between the light source and the sample. Thus the sample is excited with polarized light. A second polarizer (the emission polarizer) is placed between the sample and the detector. This is used to polarize the emission parallel and perpendicular to the excitation polarization. The intensity of the emission in each configuration is measured and a quantity called the anisotropy calculated via:

$$R = \frac{I_{\parallel} - I_{\perp}}{I_{\parallel} + 2I_{\perp}} \tag{5.2}$$

In most fluorescence experiments, an L-configuration is used. That is, the excitation and emission beams are at right angles in the horizontal plane. This is illustrated in Figure 5.1.

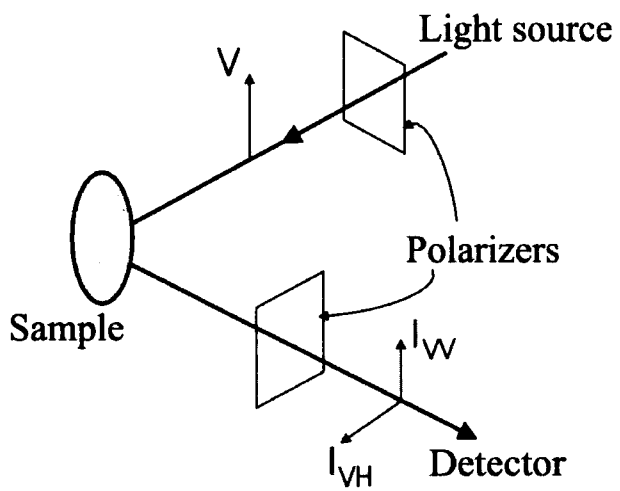

Figure 5.1: Labelling of polarization components in an L-configuration fluorescence experiment.

The z-axis is parallel to the vertical direction, and R can also be written:

$$R = \frac{I_{VV} - I_{VH}}{I_{VV} + 2I_{VH}} \tag{5.3}$$

This notation of polarization according to whether the light is polarized vertically or horizontally will be used throughout this chapter.

It can be shown mathematically that for an unoriented sample, R can only take values between -0.2 and 0.4. If a molecule has its absorption dipole moment at an angle θ to the electric vector of the excitation light, then the probability of absorption is proportional to $\cos^2 \theta$. Hence, polarized light creates an anisotropic angular distribution of excited molecules even in an isotropic sample. This is called *photoselection.* Similarly, when a molecule has its emission dipole moment lying at an angle φ to the emission polarizer, the intensity of the measured emission is proportional to $\cos^2 \varphi$.

If the absorption and emission transition dipole moments lie along the same direction, the fluorescence anisotropy takes its maximum value of 0.4. Any difference between the two directions results in depolarization of the signal and a decrease in R. A completely depolarized signal has R = 0 and no difference between the intensities of the vertically and horizontally polarized light.

Factors which lead to depolarization include rotation of molecules in a solution, an intrinsic difference between the direction of the absorption and emission dipole moments in a molecule (the fundamental anisotropy) and energy transfer to other molecules.

5.2.4 *Measurement of fluorescence anisotropy*

Measurement of fluorescence anisotropy in solution is reasonably straightforward. In films however, the L-configuration presents a problem. The film must be set at some angle to the excitation and emission light paths. In this situation, the transmission of the light across the film-air boundary is dependent on the polarization of the light: light

with its electric vector vertical, parallel to the film surface (s-polarized light, TE mode) experiences a different transmission coefficient to horizontally polarized light which has its electric vector in the plane of incidence (p-polarized light, TM mode). The transmission coefficients depend on the angle of incidence and the refractive index of the film. Hence, the measured anisotropy will in general differ from the actual anisotropy.

A method of overcoming this problem is to place the film between glass prisms which have the same refractive index as the film at appropriate wavelengths. However, it is not possible to obtain spectra like this and there are situations in which it is impractical to use such a set-up e.g. in a cryostat. Later in this chapter, we examine the possibility of using the refractive index data from Chapter 3 to correct for these optical effects.

5.2.5 *Samples with a preferred orientation*

When the molecules in a sample have a preferred orientation, for example in aligned polyfluorene films, the anisotropy measurements and their interpretation become more complex. To begin with, there is an additional parameter – the orientation of the film. Secondly, the anisotropy no longer has an upper limit of 0.4 but may take any value up to 1. How anisotropy data relates to the structure of the film is not trivial, as the angular distribution of the molecules may take many forms. One approach to obtaining information on the degree of orientation has been employed by Schartel et al.[172] They performed anisotropy measurements on aligned polyfluorene films and analysed the results using a Legendre expansion method.[173,174] Briefly, the idea is that the angular distribution may be related to a polynomial expansion according to:

$$N(\theta) = \sum_l \alpha_l P_l(\cos\theta) \tag{5.4}$$

$$\alpha_l = (1/2\pi)\left[(2l+1)/2\right]\left\langle P_l(\cos\theta)\right\rangle \tag{5.5}$$

$P_l \cos\theta$ are Legendre polynomials and $\langle P_l \cos\theta \rangle$ is the mean value of $P_l \cos\theta$ averaged over the distribution. This mean value is abbreviated as $\langle P_l \rangle$. Assuming that the two opposite directions along a chain axis are equivalent, then α_l is non-zero only for even l.

The parameters $\langle P_2 \rangle$ and $\langle P_4 \rangle$ can be related to experimental observables I_{VVV}, I_{VVH}, I_{HVV}, I_{HVH}, I_{HHV}. These are fluorescence intensity measurements with the first subscript describing film orientation, the second describing the position of the excitation polarizer and the third describing the position of the emission polarizer. $\langle P_2 \rangle$ may also be obtained from absorption dichroism measurements. To fully describe the angular distribution, higher order terms $\langle P_6 \rangle$ and above are necessary. Unfortunately these may not be obtained through fluorescence measurements. However, the relationship between $\langle P_2 \rangle$ and $\langle P_4 \rangle$ can be compared with predictions of the most likely angular distribution.[175]

5.3 Fluorescence anisotropy values from steady-state measurements: corrections for optical effects

The problem with performing steady-state fluorescence anisotropy measurements on films in a commercial spectrofluorimeter is that the excitation and emission paths are at an angle to the film surface normal. This is because of the L-configuration in most spectrofluorimeters. This is a problem because the transmission of polarized light at boundaries depends upon the polarization of light i.e. whether the light is p- or s-polarized. In films of the type measured here the situation is further complicated by the anisotropic optical constants of the films. The apparent values of fluorescence anisotropy will therefore depend upon the angle of incidence of the incident beam.

It was desired to find some correction, such that the polarized light intensity in the film at the film boundary could be calculated. The anisotropic optical constants for both aligned and unaligned films were calculated in Chapter 3. By using these optical

constants in the Fresnel equations for transmission of s- and p-polarized light, it should be possible to find this correction for any angle of incidence.

The Fresnel equations are:

$$t_s = \frac{2\cos\theta_i}{\cos\theta_i + \sqrt{n_s^{\,2} - \sin^2\theta_i}} \tag{5.6}$$

$$t_p = \frac{2n_p\cos\theta_i}{n_p^{\,2}\cos\theta_i + \sqrt{n_p^{\,2} - \sin^2\theta_i}} \tag{5.7}$$

t_s and t_p are the Fresnel transmission coefficients for s- and p-polarized light respectively. n_s and n_p are the refractive indices for s- and p-polarized light respectively. θ_i is the angle of incidence.

The actual power transmitted is related to the transmission coefficients above by the following relation:

$$T = n\left(\frac{\cos\theta_t}{\cos\theta_i}\right)t^2 \tag{5.8}$$

It is a function of angle and refractive index because the cross-sectional area and speed of the beam change on transmission across the boundary.

For light which is not polarized along the ordinary direction, the refractive index will be a function of angle of incidence according to:

$$n = \frac{1}{\sqrt{\frac{\cos^2\phi}{n_o} + \frac{\sin^2\phi}{n_e}}} \tag{5.9}$$

where ϕ is the angle between the light beam and the optic axis, n_o is the refractive index for an ordinary beam and n_e the refractive index for an extraordinary beam.

Corrections were calculated for both aligned and unaligned films. The procedure for calculating this expression was as follows. Firstly, the path that the light takes has to be calculated. This is shown in Figure 5.2.

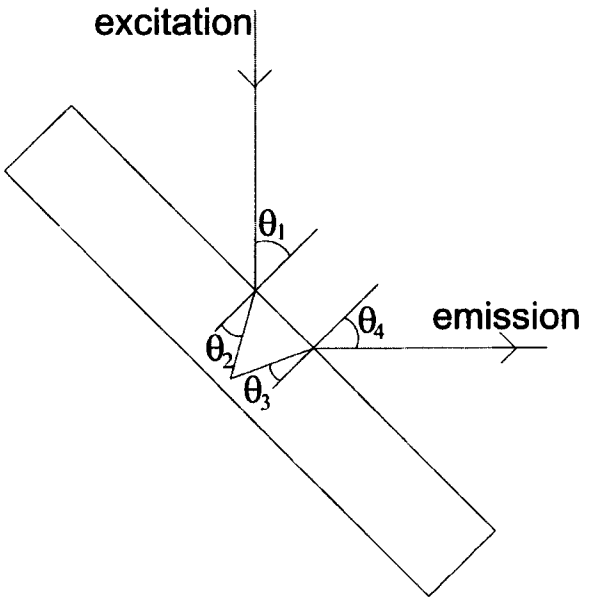

Figure 5.2: Light path through a thin film in the L-configuration, showing refraction as the light enters the film, and the necessary angle of incidence as the light leaves the film

θ_1 is the angle of incidence of the beam travelling from air into the film. θ_2 is the subsequent angle of refraction. Light is absorbed in and then emitted from the film. To be incident on the detector, the sum of θ_1 and θ_4 must be 90°. θ_3 is the angle of incidence of the emitted light travelling from the film to air that results in the required angle of refraction θ_4.

Finding this path should be straightforward since the refractive indices of the film are known. However, if the light is not polarized along the ordinary direction of the film, then the refractive index will depend upon the direction in which the light is travelling. In turn, this direction will depend upon the refractive index of the material. In this situation, the direction and refractive index were found by an iterative process.

The direction was estimated first, and the refractive index for this direction calculated. This refractive index was then used to calculate the direction at which the light would have to be travelling to reach the detector. If this did not match the estimated direction, then the direction would be altered slightly and the calculations repeated. This would be done until the direction and refractive index were mutually consistent.

Once the angles and refractive indices were known, the Fresnel transmission coefficients could be calculated. The aim was to find correction factors to take into account the different transmission of vertically and horizontally polarized light at the film-air boundary. This was done for excitation at 350 nm (refractive index at a minimum here), 380 nm (the peak of the PF absorption) and 410 nm (refractive index at a maximum here).

Before proceeding, it is noted that the figures in the following section of mostly illustrative of the need for correction of the emission spectra in polarized fluorescence anisotropy measurements. Interpretation of the data is complicated and briefly discussed.

5.3.1 *Unaligned films*

A coupling constant for transmission of vertically and horizontally polarized light was defined as follows:

$$I_{meas} = CI_{bnd} \tag{5.10}$$

where I_{meas} is the light intensity measured at the detector, C is the coupling constant and I_{bnd} is the light intensity at the film-air boundary. Since in the unaligned films, samples were excited with vertically polarized light and the emission polarizer alternated between vertical and horizontal, coupling constants were found for configurations I_{VV} and I_{VH}. Further parameters were the excitation wavelength and incident angle of the excitation beam. Coupling constants are plotted in Figure 5.3 and Figure 5.4:

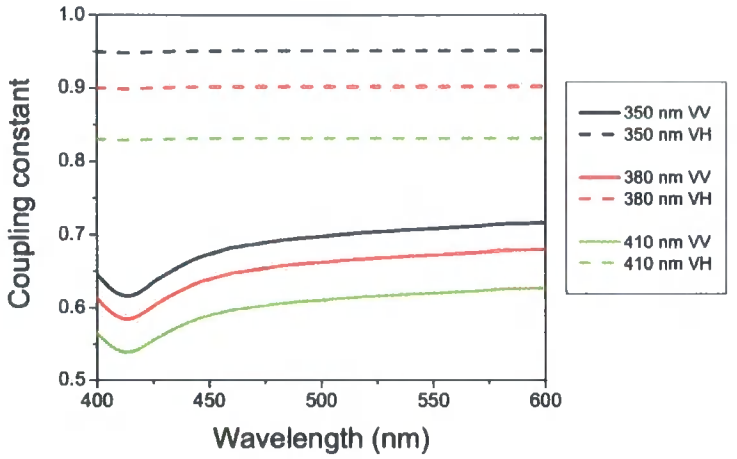

Figure 5.3: Coupling constants for polarization measurements of the emission from unaligned PF films, 30° angle of incidence, for three different excitation wavelengths

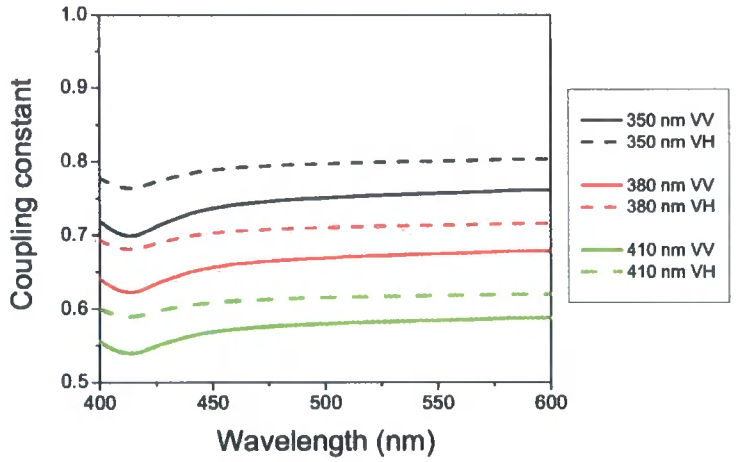

Figure 5.4: Coupling constants for polarization measurements of the emission from unaligned PF films, 60° angle of incidence, for three different excitation wavelengths

The plots above should allow us to calculate corrected spectra for different angles of incidence. This was tested for an unaligned film as follows. The sample was mounted in a sample holder that allowed adjustment of the angle of incidence of the excitation beam. The film was excited with vertically polarized light at 380 nm at angles of incidence of 30° and 60°, and the horizontally and vertically polarized components of

the emission measured. The plots above were then used to correct the spectra and recover polarized emission spectra in the film at the film boundary. This is shown in the figures below:

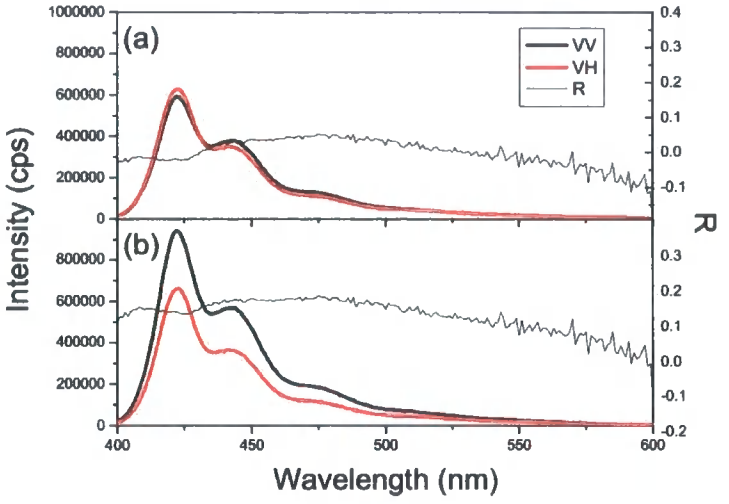

Figure 5.5: PF emission spectra, 30° angle of incidence (a) uncorrected and (b) corrected for out-coupling of different polarizations of light. The thin line shows the polarization anisotropy

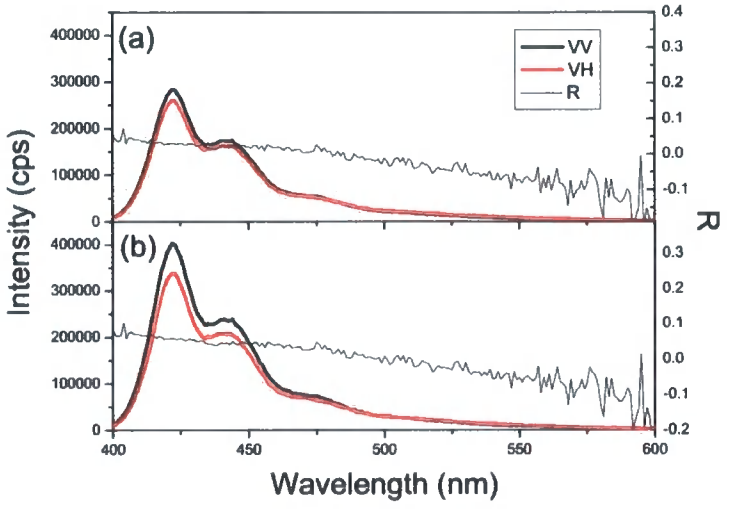

Figure 5.6: PF emission spectra, 60° angle of incidence (a) uncorrected and (b) corrected for out-coupling of different polarizations of light. The thin line shows the polarization anisotropy

In the figures above, prior to correction it appears as though the fluorescence is almost completely depolarized. After correction however, it is evident that in the film, the emission has significant fluorescence polarization anisotropy. This shows that despite exciton migration, the signal is still not completely depolarized.

One possible reason for this is to do with the L-configuration of the experiment and the angle of incidence of the excitation beam. It is seen that there are differences in fluorescence polarization ratio for different angles of incidence. This can be qualitatively explained according to the angular dependence of electric dipole radiation. It is well-known that dipoles do not emit along their axis. Let us first simplify the situation by assuming that all vertical polarized emission comes from polymer chains oriented vertically in the film. Conversely, assume that all horizontally polarized emission comes from polymer chains oriented horizontally in the film. If the film is rotated to vary the angle of incidence, this will not affect the emission from the vertically-oriented chains (at least inside the film; the effect of transmission at the film boundary has been taken into account above). However, as angle of incidence is decreased, the angle that the horizontal chains make with the direction of the detector becomes more acute. The axis of the dipole moment becomes closer to being parallel with the detector direction and as such the emission along this direction becomes weaker.

5.3.2 *Aligned films*

Out-coupling plots were made for the following configurations: VVV, VVH, HVV, HVH, HHV. The first letter designates the whether the chain alignment direction is horizontal or vertical, the second letter designates the excitation polarization and the third letter designates the emission polarizer position. These five particular configurations were chosen because they are necessary and sufficient for describing the alignment of a film in terms of the Legendre polynomials, as described earlier.

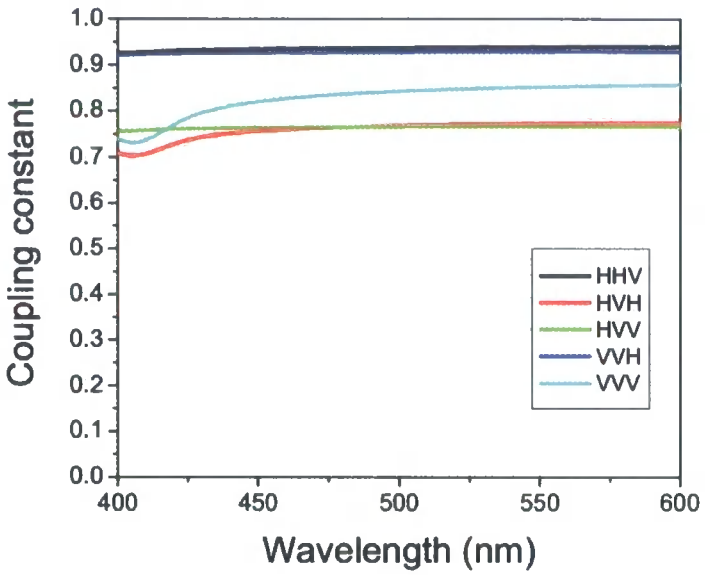

Figure 5.7: Coupling constants for different configurations of light polarization and film orientation, for an angle of incidence of 60° and an excitation wavelength of 350 nm

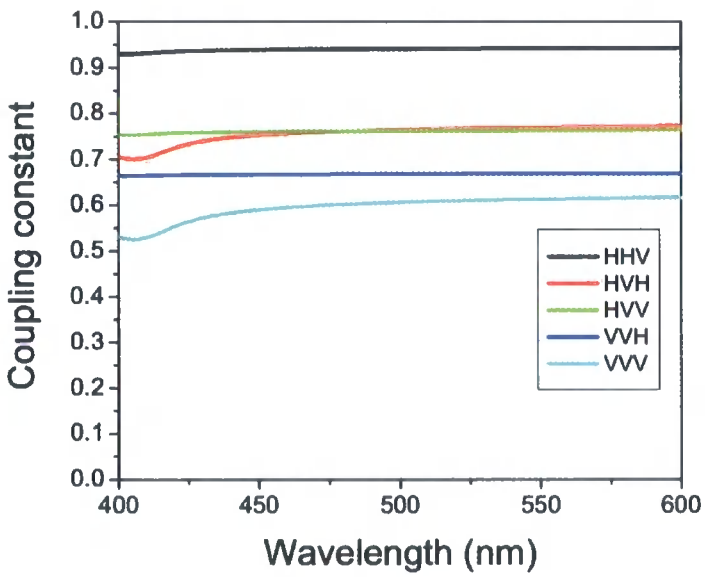

Figure 5.8: Coupling constants for different configurations of light polarization and film orientation, for an angle of incidence of 60° and an excitation wavelength of 380 nm

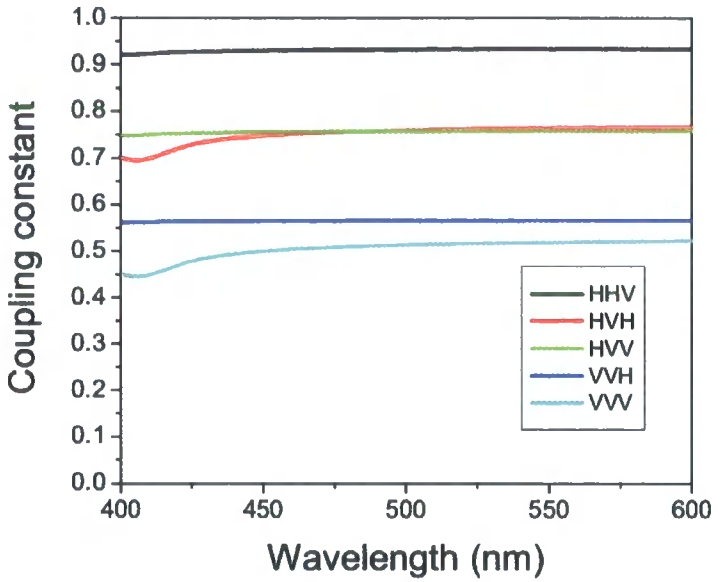

Figure 5.9: Coupling constants for different configurations of light polarization and film orientation, for an angle of incidence of 60° and an excitation wavelength of 410 nm

These coupling constants were used to correct the polarized fluorescence spectra of aligned films. This finds the emission intensity for polarized light in the film at the film boundary.

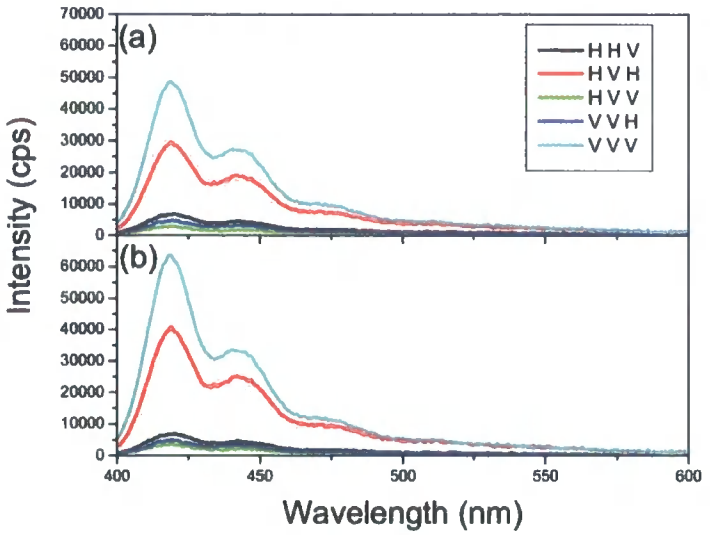

Figure 5.10: PF emission spectra, excitation at 350 nm, 60° angle of incidence (a) uncorrected and (b) corrected for out-coupling of different polarizations of light.

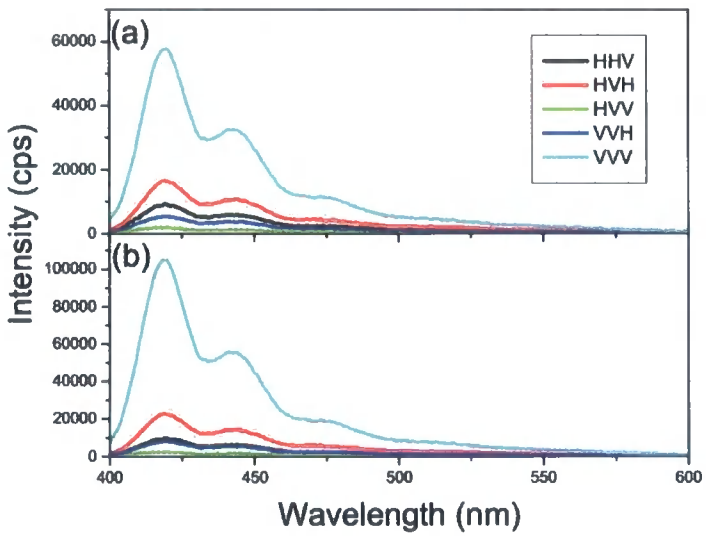

Figure 5.11: PF emission spectra, excitation at 380 nm, 60° angle of incidence (a) uncorrected and (b) corrected for out-coupling of different polarizations of light.

The choice of excitation wavelength greatly affects the observed and corrected emission profiles. The coupling constants for excitation at 350 nm are more similar

than those at other wavelengths, and thus less of a correction is needed. The other point is that the emission intensity for configuration HVH is observed to vary greatly for different excitation wavelengths. A possible reason for this is discussed in the next section.

It is possible that the corrected spectra above could be used to find the polarized emission profile from polyfluorene chains. However, this is beyond the limited scope of the work here.

5.4 Excitation profiles of aligned polyfluorene films

As an attempt to investigate excitation energy migration in aligned PF films, excitation profiles were made. These are fluorescence spectra in which the emission wavelength is held constant and the excitation wavelength varied. Excitation spectra were measured for an aligned film in the following configurations: VVV, VVH, HVV, HVH, HHV with the emission wavelength fixed at 442 nm. The results are shown in Figure 5.12.

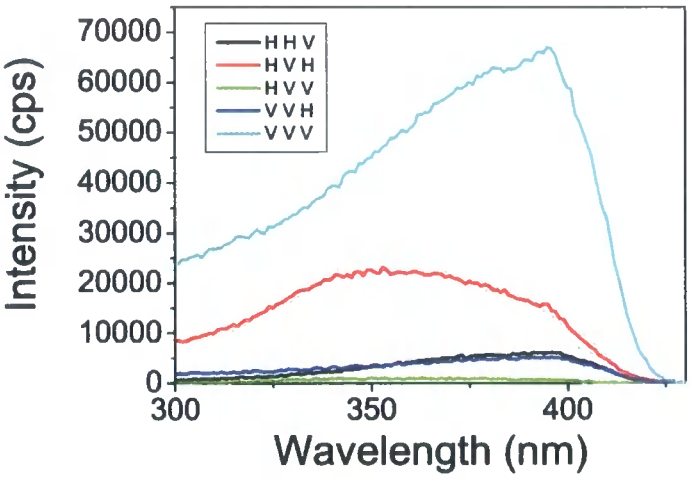

Figure 5.12: Excitation spectrum of an aligned PF film

For each of the configurations in which the film was excited parallel to its alignment direction, the excitation spectra are similar to the absorption spectra. This is not unusual, as the intensity of the emission will depend upon the number of photons

absorbed. (NB. The spike at 395 nm is due to an increase in the xenon arc lamp power at this wavelength) By this rationale, the excitation spectra for HVH and HVV are most interesting, being quite different to the others. The fluorescence peaks at a higher excitation energy and the shape is more symmetrical than the usual PF absorption spectra.

These results suggest some electronic transition perpendicular to the polymer backbone. Support for this comes from the absorption coefficients found from the ellipsometry measurements in Chapter 3. Comparing the absorption coefficients for the aligned and unaligned PF films, it can be seen that the absorption perpendicular to the backbone in aligned films is stronger at shorter wavelengths when compared to the unaligned films.

It is noted that exciting aligned films perpendicular to the orientation direction results in the usual PF emission spectrum. Therefore, if a different electronic transition exists here, then it does not give rise to emission. It could be that the state relaxes quickly to the state whose transition dipole moment lies parallel to the chain backbone.

5.5 Characteristics of the fluorescence anisotropy of unaligned and aligned PF films

5.5.1 *Temperature dependent measurements*

It was shown in Chapter 4 that excitons travel further at room temperature than at low temperature. Since exciton migration is associated with fluorescence depolarization, it was desired to see if this effect is measurable in steady-state measurements.

Steady-state measurements were performed in a Jobin-Yvon Fluoromax spectrofluorimeter, fitted with Glan-Thomson polarizers on the excitation and emission paths. The excitation was at 380 nm and the beam was vertically polarized. Sample emission was measured horizontally and vertically. The sample was mounted in a closed-cycle helium cryostat. Excitation was through the back of the sample, and the sample surface normal was at an angle of approximately 45° to the emission path.

Emission spectra were measured from 15 K – 300 K and the fluorescence anisotropy calculated at each temperature.

The experiment was repeated several times and the fluorescence anisotropy was found not to vary with temperature. This indicates that increased exciton motion at elevated temperatures does not increase the anisotropy further. From Chapter 4, the exciton diffusion length at low temperature for excitation at 380 nm is 11 nm. This distance is therefore sufficient for depolarization of the emission.

5.5.2 *Polarized TCSPC measurements on aligned and unaligned films*

Measurements of the time-resolved fluorescence anisotropy were made on aligned and unaligned PF films. The unaligned film was excited with vertically polarized light and the intensity of the horizontally and vertically polarized emission measured. The aligned films were measured in the same way, except that the alignment of the film provided an additional experimental parameter. The film was oriented both vertically and horizontally, with the excitation polarized vertically, and measurements made in both configurations. Results are shown in Figure 5.13, Figure 5.14 and Figure 5.15, with the calculated anisotropy plotted as a red line.

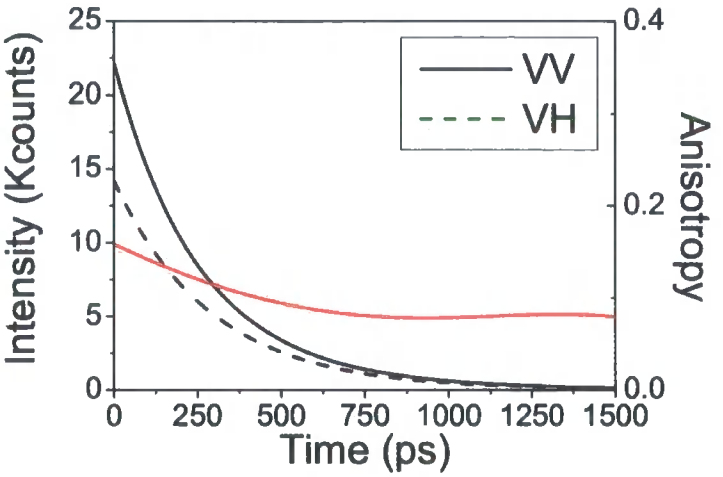

Figure 5.13: Emission from an unaligned film at 435 nm, polarized vertically and horizontally. Excitation was at 390 nm with vertically polarized light. The red line shows the calculated anisotropy.

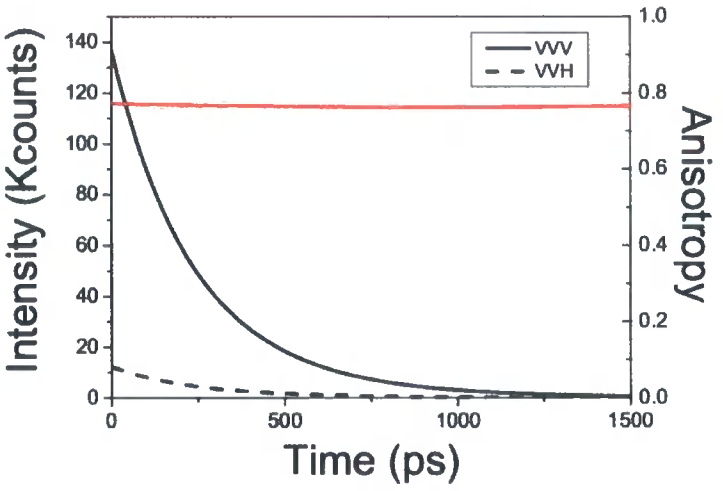

Figure 5.14: Emission from an aligned film at 435 nm, polarized vertically and horizontally. Excitation was at 390 nm with vertically polarized light, parallel to the film alignment direction. The red line shows the calculated anisotropy.

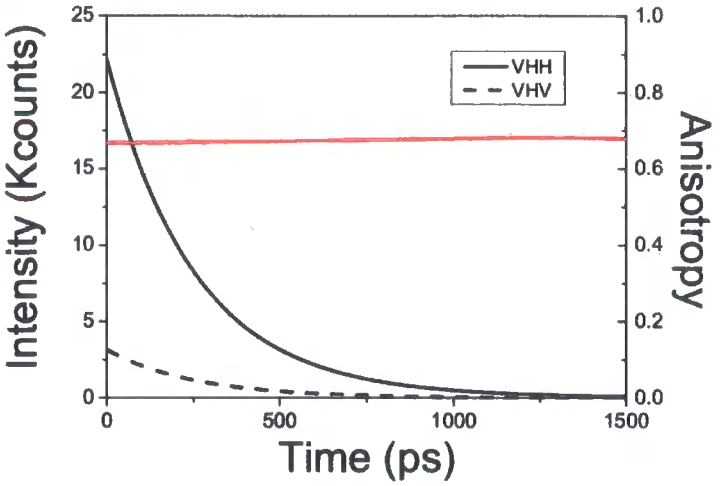

Figure 5.15: Emission from an aligned film at 435 nm, polarized vertically and horizontally. Excitation was at 390 nm with vertically polarized light, perpendicular to the film alignment direction. The red line shows the calculated anisotropy.

The decays above were found by deconvolution of the TCSPC data, according to bi-exponential fits: $I(t) = A_1 \exp(-t/\tau_1) + A_2 \exp(-t/\tau_2)$. The fit parameters are shown in Table 2.

Film configuration	τ_1 (ns)	τ_2 (ns)	A_1	A_2
unaligned - VV	0.24	0.44	17.99	3.65
unaligned - VH	0.29	1.48	15.06	0.09
aligned - VVV	0.21	0.34	95.41	41.62
aligned - VVH	0.21	0.33	7.95	4.55
aligned - VHH	0.25	0.60	21.54	0.60
aligned - VHV	0.25	0.75	3.06	0.05

Table 2: Fit parameters for the deconvoluted TCSPC data

The data from the aligned films shows that the emission is highly polarized, with dichroic ratios of 11 and 7 for the vertical and horizontal configurations. The anisotropy is steady over the whole time range.

The data from the unaligned film is more interesting. It shows an apparent decrease in the anisotropy with time, levelling of at a value of about 0.08 after around 750 ps. Obviously, this is not an observation of depolarization via exciton migration, as this

occurs on a much faster timescale than the resolution of our apparatus. The fit parameters shown in the table may reveal the source of this anisotropy decrease.

Recall that polyfluorene chains consist of segments of unbroken conjugation and excitons are delocalised over these segments. Segments may be of different lengths. Shorter segments are higher energy sites and have longer fluorescence lifetimes. Longer segments are lower energy sites and have shorter fluorescence lifetimes.[176] Parallel emission appears to consist of a short decay time and a long decay time. Perpendicular emission mostly consists of a single, short decay time. This suggests that emission polarized parallel to the excitation comes from high energy and low energy sites, whereas perpendicular to the excitation, the emission is from low energy sites. Emission perpendicular to the excitation comes from excitons that must have travelled to rotate their dipole moment, lowering their energy in the process. The long lived, high energy component of the parallel emission may come from excitons which haven't moved, because they are trapped.

These measurements also provide the opportunity to calculate the steady state fluorescence anisotropy from an unaligned PF film. This is difficult to calculate in a spectrofluorimeter due to the 90° angle between the excitation and emission beams, meaning that the film must be excited at some angle to its surface normal. The different transmission of p- and s-polarized light at its surface will affect the observed fluorescence anisotropy. This is discussed earlier in this chapter. However, here the emission is measured along the direction of the surface normal and such effects will not occur. The steady-state fluorescence anisotropy can be calculated from time-resolved data by the following relation:

$$R = \frac{\int_0^\infty I(t)R(t)dt}{\int_0^\infty I(t)dt} \tag{5.11}$$

A value of 0.12 arises. This is definitely non-zero, indicating that the emission is not completely depolarized in the film, despite the efficient exciton migration taking place. It is noted that a value of 0.1 for the fluorescence anisotropy for PF in dilute, viscous

solution at room temperature has been found experimentally.[177] This is similar to the value found here and would suggest that the excitons in these films are purely intrachain in nature.

To investigate whether the observed anisotropy was merely an artefact of the experimental set-up, the measurements were repeated with different excitation polarizations. The excitation was polarized vertically and at 45° with emission measured at three wavelengths. For vertical excitation, the high anisotropy values were again seen. For 45° excitation, the anisotropy is very close to zero. This is what one expects, as this light with this polarization should create vertically and horizontally excited chain populations in equal numbers. The residual anisotropy is most likely due to the fact that the excitation beam was at an angle of incidence of approximately 45°, meaning that the horizontally polarized component of the light would be transmitted differently to the vertically polarized component.

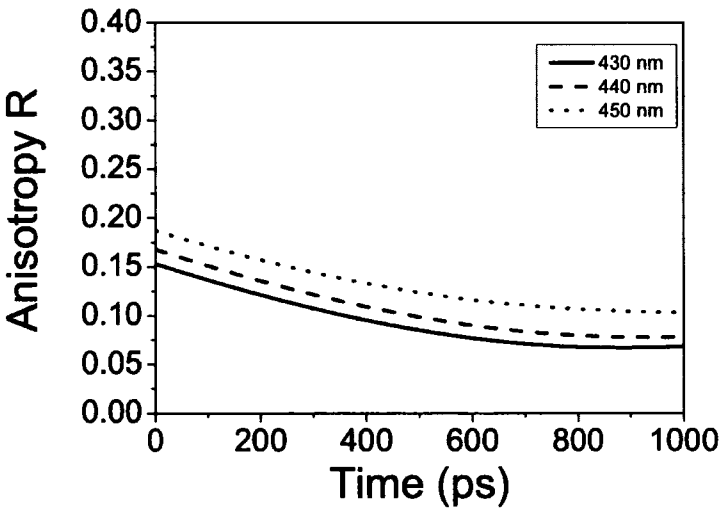

Figure 5.16: Anisotropy decays at three wavelengths, for excitation of an unaligned PF film with vertically polarized light

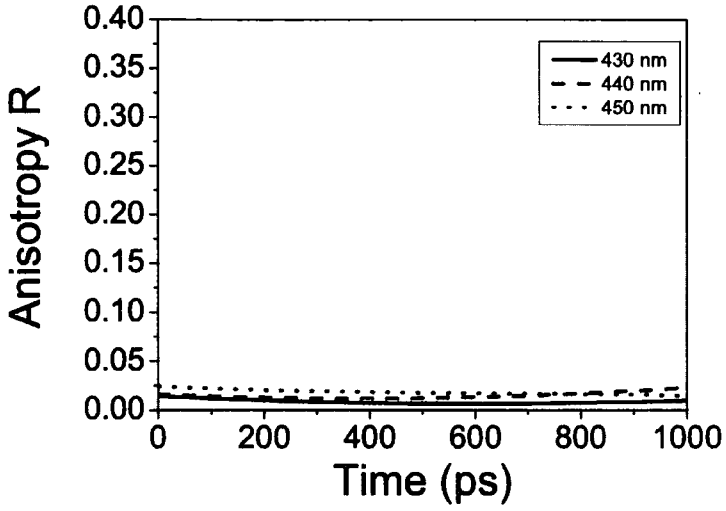

Figure 5.17: Anisotropy decays at three wavelengths, for excitation of an unaligned PF film with light passed through a polarizer at 45 degrees to the vertical.

As a final point, it is noted that the value found here for the fluorescence anisotropy of PF films found from front-face collected time-resolved measurements is higher than the value one would expect from extrapolating the L-configuration steady-state measurements to equivalent front-face collection (i.e. extrapolating to an incident angle of 90°). This would suggest that unfortunately our corrections of the data are not adequate to overcome the uncertainties in the steady-state measurements.

5.6 Energy transfer in unaligned and aligned PF films containing dopant molecules

Our intention here was to combine energy transfer and film alignment, to investigate the possibility of making films that provide polarized emission with a range of colours. The dopant molecules used were tetraphenyl porphyrin (TPP), a planar, red-emitting dye, and 4-(dicyanomethylene)-2-methyl-6-(p-dimethylaminostyryl)-4H-pyran (DCM), a more linear dye with emits with an orange colour. The transition dipole moment of TPP is mostly in-plane, whilst the DCM is expected to have its transition dipole moment along its long axis. For polarized emission to occur, the population of

excited molecules must have a suitable orientation distribution. We intend to show how such a population may come about.

5.6.1 *Experimental*

The polyfluorene used was poly(9,9-diethylhexyl fluorene) (M_n = 7600, M_w = 15000). This is a low molecular weight polyfluorene of approximately 20 repeat units, and is especially suitable for alignment.

Aligned and unaligned PF films were made, with various degrees of doping. Films were spin-coated from PF solutions of 10 mg/ml at 2500 rpm, and contained the following weight fractions of dopant: 0.05 %, 0.5 %, 5 % TPP, and 0.025 %, 0.25 %, 2.5 % DCM. As the molecular weight of a TPP molecule is about twice that of a DCM molecule, these weight fractions correspond to approximately equal molar concentrations for each dopant. The solvent was a mixture of toluene and chloroform in the ratio 3:1. This mixture was used to prevent crystallization in the films. Unaligned films were prepared by spin-coating on Spectrosil discs. Aligned films were prepared by spin-coating on rubbed polyimide substrates followed by heating at 80°C for 10 minutes in an argon atmosphere.

Absorption measurements were made using a J.A. Woollam Co. VASE ellipsometer, set up in the transmission mode. This allowed easy acquisition of polarized absorption spectra. Steady state fluorescence measurements were made using a Jobin-Yvon Fluoromax spectrofluorimeter, fitted with Glan-Thomson polarizers. Fluorescence spectra were corrected as appropriate for the polarization response of the instrument. Film spectra were recorded in an L-format, with the emission measured at right angles to the direction of the excitation beam. The angle of incidence of the excitation beam on the films was 60 degrees. Films were excited with unpolarized light, while the intensity of the emission was measured through a polarizer set vertically or horizontally. When aligned films were measured, their alignment direction was set normal to the plane of incidence i.e. parallel to the vertical direction of the emission polarizer. As described in Chapter 2, the excitation beam is only weakly polarized. Therefore, anisotropy in the emission would mostly result from the film structure rather

than photo-selection. Time resolved fluorescence measurements were performed using a time-correlated single photon counting (TCSPC) system, described earlier.

5.6.2 *Results and analysis*

The absorption spectra of the unaligned films matched the usual PF absorption spectra. Addition of the dopant molecules did not affect the spectra, except in the case of the 5 % w/w TPP doped sample, where the Soret band of the TPP absorption could be clearly seen. Polarized absorption spectra of the aligned films are shown in Figure 5.18 and Figure 5.19 Since the alignment substrates are absorbing below ~ 400 nm and the absorption spectra of the polymer perpendicular to its alignment is low, background subtraction is difficult here. All films showed good alignment, with dichroic ratios of approximately 10. There was no correlation between doping concentration and degree of alignment. Again, the DCM absorption could not be observed in any of the samples, and TPP absorption could only be seen in the heavily doped sample. Unlike the polyfluorene absorption, the TPP absorption does not show any dichroism, and therefore we can say that the TPP molecules exhibit no preferential alignment. Since the DCM absorption cannot be seen, these absorption measurements tell nothing about any alignment of these molecules.

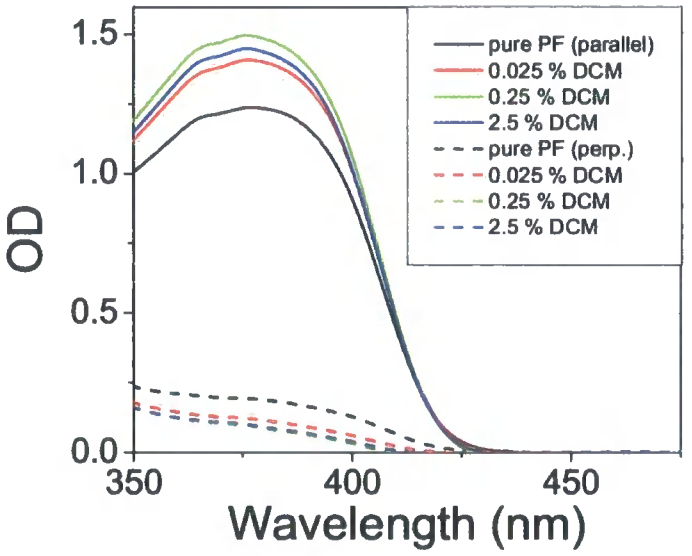

Figure 5.18: Absorption spectra of aligned PF films, doped with DCM, measured for light polarised perpendicular (solid line) and parallel (dashed line) to alignment direction.

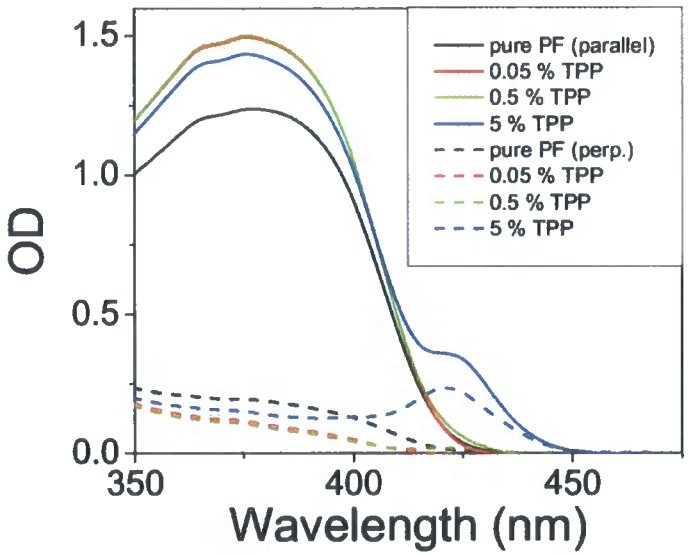

Figure 5.19: Absorption spectra of aligned PF films, doped with TPP, measured for light polarised perpendicular (solid line) and parallel (dashed line) to alignment direction.

Samples of the fluorescence spectra of the unaligned films are shown in Figure 5.20. The ratio of dopant emission to polymer emission increased with increasing dopant fractions, which is only to be expected; as the distance between an excited polymer and an unexcited dopant decreases, the probability of Förster energy transfer increases. In all cases, both the polymer host and dopant guest emission are almost completely unpolarized. Again, this is to be expected since they were excited with unpolarized light. Any residual anisotropy is due to either or to the partial polarization of the excitation beam, or the fact that emission was not collected normal to the film surface, and so the Fresnel transmission coefficients for differently polarised light will be different.

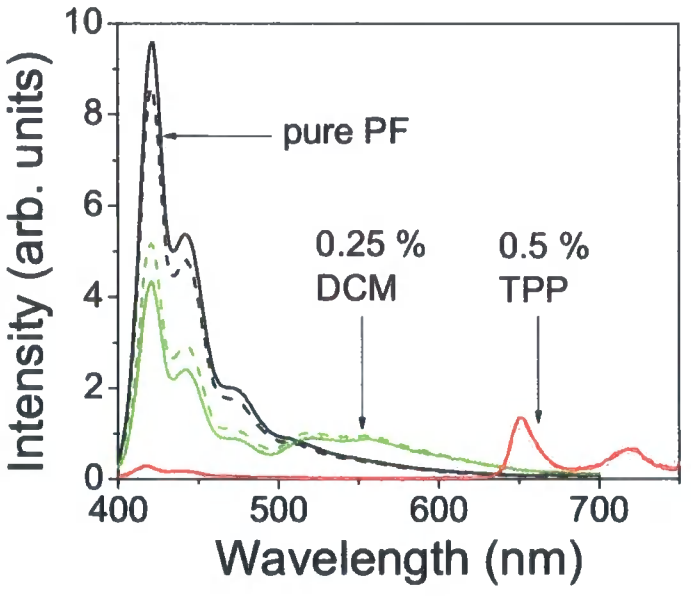

Figure 5.20: Steady-state fluorescence measurements of unaligned PF films, excited with unpolarized light. Films are labelled according to their doping type. Emission was measured through polarizers set vertically (solid lines) and horizontally (dashed lines).

More interesting are the results for polarised fluorescence from the aligned films, shown in Figure 5.21 and Figure 5.22. The polymer emission in each case is highly polarised, with a ratio of vertical to horizontal emission of around 10. The TPP emission for all dopant concentrations was almost completely depolarised. DCM emission could not be seen at the lowest concentration, due to only a small amount of

energy transfer. Unexpectedly, DCM emission could not be seen at the highest concentration either. This may be due to some phase separation during the alignment process, forming DCM aggregates with low fluorescence quantum yield. However, the DCM emission at 0.25 % w/w shows some anisotropy. Since the DCM emission overlaps with the tail of the PF emission, it is necessary to deconvolute the spectra in order to properly inspect the DCM anisotropy. This was done by subtracting a suitably normalised pure PF emission spectrum, to leave only the dopant emission. The result is plotted in the inset of Figure 5.22 and shows that the dopant emission has a dichroic ratio of approximately 3.

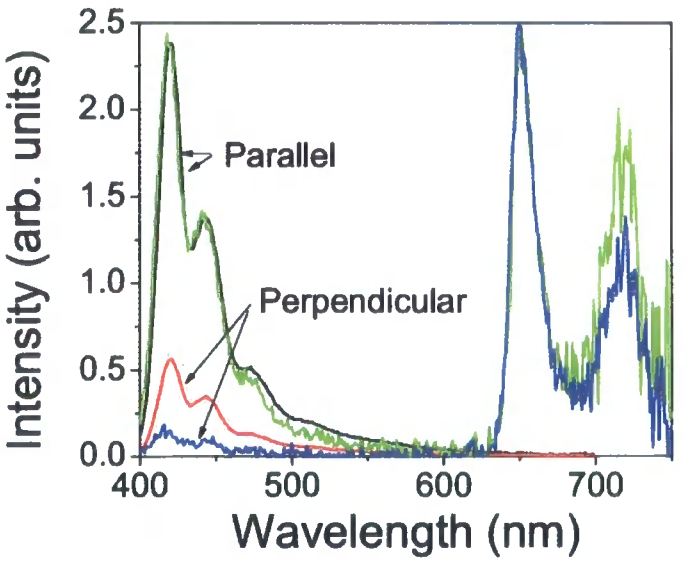

Figure 5.21: Steady state fluorescence measurements of a pure, aligned PF film (black and red lines) and an aligned PF film doped with 0.5 % w/w TPP (green and blue lines), excited with unpolarized light. Emission was measured polarized parallel or perpendicular to the excitation as labelled on the figure. The PF emission is well polarised in each case, but the TPP emission is completely unpolarized.

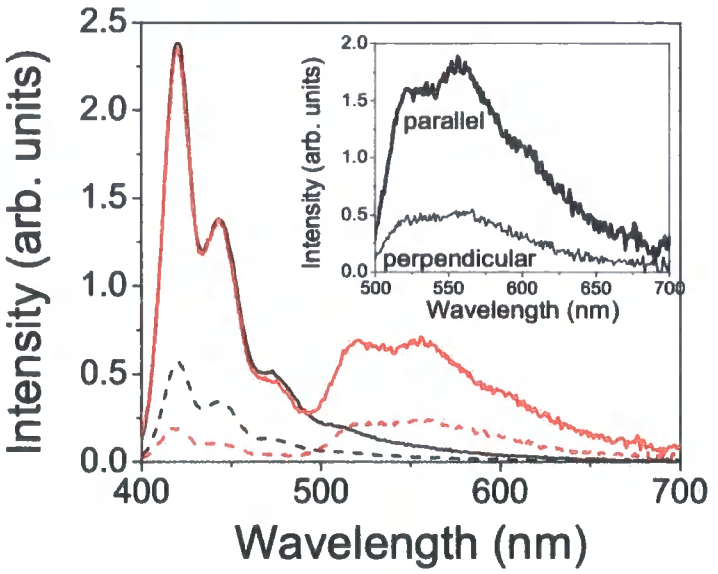

Figure 5.22: Steady state fluorescence measurements of a pure, aligned PF films (black lines) and an aligned PF film doped with 0.25 % w/w DCM (red lines), excited with unpolarized light, with emission measured polarised parallel (solid lines) and perpendicular (dashed lines) to the alignment direction. The PF emission is well polarised in each case. The inset shows the deconvoluted DCM emission, which exhibits a reasonable degree of polarisation.

TCSPC measurements were made on the aligned and unaligned 0.25 % w/w DCM-doped films. Samples were excited with vertically polarised light and emission measured parallel and perpendicular to this excitation. When aligned films were used, the excitation direction was set parallel to the alignment direction. Since the lifetimes of the fluorescence decays are not long compared to the width of the excitation pulse, it would necessary to perform a deconvolution to obtain decay lifetimes. However, here we are interested more in making qualitative comparisons rather than quantitative ones, so the raw decay curves will suffice.

For the doped, aligned sample, the dichroic ratio of the PF emission was approximately 16, while for the DCM emission it was approximately 4. Since the emission is collected normal to the film surface, this shows that the DCM emission is indeed polarised, and that the observed polarisation is not due to different transmission coefficients for s- and p-polarised light at the film boundary. Indeed, the dichroic ratio

here is higher than for the L-configuration steady state measurement. However, this may be due to the fact that the samples were excited parallel to the alignment direction, rather than with unpolarized light as in the steady state measurements.

Comparing the lifetime of the PF in the pure and doped samples, it was seen that the lifetimes in the doped samples was shorter. This is to be expected, as energy transfer to the dopant opens up another non-radiative decay path. An interesting point to note is that the lifetime of the PF is shorter in the aligned doped samples than in the unaligned doped samples. This is true for the PF fluorescence measured polarised both parallel and perpendicular to the excitation polarisation and is shown in Figure 5.24. This difference is not simply due to the alignment process, since undoped films exhibit almost identical lifetimes whether aligned or not. One explanation would be that energy transfer is promoted in the aligned films, due to an orientation of the PF and the DCM. Recalling the expression for Förster radius from Chapter 4:

$$R_0^6 = \frac{9000\kappa^2 \ln 10}{128\pi^5 n^4 N_{AV}} \varphi_{FL} \int_0^\infty \frac{f_D(v)\varepsilon_A(v)}{v^4} dv \tag{5.12}$$

$$\kappa^2 = \left(\cos\theta_T - 3\cos\theta_D \cos\theta_A\right)^2 \tag{5.13}$$

where θ_T is the angle between the donor and acceptor transition dipole moments, θ_D is the angle between the donor transition dipole moment and the direction vector connecting the two molecules, and θ_A is the angle between the acceptor transition dipole moment and the same direction vector. κ^2 may take a value between 0 and 4. $\kappa^2 = 0$ if the transition dipole moments are perpendicular to one another. For a given direction vector, κ^2 is maximized for parallel transition dipole moments. Examples of κ^2 values and the corresponding orientation factors are shown in Figure 5.23.

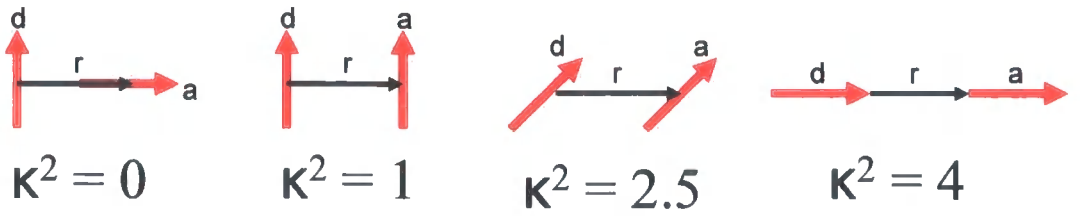

Figure 5.23: Examples of κ^2 values for various transition dipole and direction orientations

For a random distribution of relative orientations, $\kappa^2 = 2/3$. Hence, an improved orientation factor requires more transition dipole moments that are closer to being parallel. This in turn requires the long axis of the DCM molecules to be aligned parallel to the polymer backbone. Since both the horizontal and vertical components of the emission are affected equally, this suggests that in the aligned film, the DCM molecules align themselves with the PF.

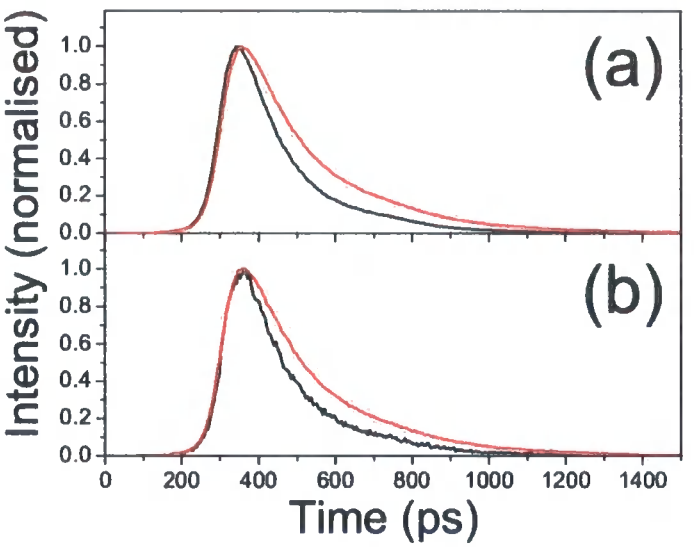

Figure 5.24: Raw PF fluorescence decay curves from aligned (black line) and unaligned (red line) 0.25 % w/w DCM-doped PF films, measured at 420 nm. Figure (a) shows the decay measured parallel to the film alignment, figure (b) shows the decay measured perpendicular to the film alignment.

5.7 Conclusions

A variety of experiments have been described in this chapter, and several conclusions can be drawn.

Correction factors taking into account the effects of refraction on polarized emission spectra have been calculated and applied. It was shown that refraction can greatly affect these spectra and that the effect depends significantly on excitation wavelength and incident angle.

It has been shown that the excitation spectra of aligned polyfluorene films differs greatly depending on whether the films are excited with light polarized parallel or perpendicular to the chain orientation.

The fluorescence polarization anisotropy of unaligned films has been shown to be independent of temperature. This indicates that even in the absence of thermally activated hopping, excitons migrate far enough to depolarize the fluorescence. Fluorescence anisotropy calculations made using TCSPC data and front face emission found a fluorescence anisotropy of 0.12. This shows that the emission is not completely depolarized. These TCSPC measurements also suggested that some excitons are trapped immediately after excitation. This could be the origin of the residual anisotropy.

Finally, aligned polyfluorene films were doped with molecular dyes. Orange polarized luminescence from DCM was observed. It was shown that the DCM molecules align themselves at least partially with the polymer chains. The polarization ratio was low and certainly not sufficient for use in a device. However, it has been shown that doping aligned films with energy transfer molecules is a possible method of achieving polarized fluorescence with a range of colours. Other dopant molecules may prove more successful.

Chapter 6: Conclusions

This thesis has described investigations into the optical and energy transfer properties of polyfluorene films. The subjects described in each chapter are mostly independent of each other and as such they will be summarized individually.

Chapter 3 described the use of variable angle spectroscopic ellipsometry to find the optical constants of aligned and unaligned films of polyfluorene. The polyfluorene used was of low molecular weight and particularly suitable for alignment. To analyse the ellipsometric data, optical models describing the samples in terms of their physical parameters were built. These models were used to generate data which could be matched to the experimental data very well. Since the models could be fit to several samples simultaneously, this indicates that they accurately described the properties of these films. Both aligned and unaligned films were found to exhibit uniaxial anisotropy. The unaligned films had their optical axis normal to the film surface and was optically negative. There was large absorption and dispersion of the refractive index perpendicular to the optical axis and small absorption and dispersion of the refractive index parallel to it. The aligned films had their optical axis oriented in plane, parallel to the rubbing direction and was optically positive. There was large absorption and dispersion of the refractive index parallel to the optical axis and small absorption and dispersion of the refractive index perpendicular to it.

The magnitude of the absorption coefficients of these films differs. In aligned films, light polarized in the alignment direction experiences absorption twice as high as light incident on unaligned films. This is because the direction of the transition dipole moment is along the chain backbone. In unaligned films there will be a distribution of these directions, and so the average transition strength in any direction will be less than for the aligned case, where the dipole moments all point approximately the same way.

The values found for the unaligned films are similar to those previously found by ellipsometry for a polyfluorene of higher molecular weight. However, the higher molecular weight polymer exhibited larger birefringence and slightly higher values for the refractive index. It is speculated that this may be due to longer chains being

constrained by their rigidity to lie in plane, while it is easier for shorter polyfluorene chains to point out of the plane. The optical constants of aligned polyfluorene films have not been measured before by ellipsometry. The values found here compare well with those found by other workers who measured the absorption coefficients by transmission measurements and applied the Kramers-Krönig relations to find the refractive indices.

The results from this chapter were used in the analysis of results presented later in the thesis. In particular, refractive index values were used in calculations of the Förster radius. Also, the refractive indices were used in calculations of the Fresnel transmission coefficients in the section of fluorescence anisotropy. Moreover, knowledge of the optical constants of polyfluorene presented here will be of use in the design of polarized polymer light emitting devices; the transmission of light at materials boundaries depends upon the refractive indices of the material and the polarization state of the light.

Chapter 4 described steady-state fluorescence measurements on polyfluorene films doped with a range of concentrations of tetraphenyl porphyrin. These provided a way to investigate the nature of the energy transfer processes within the polymer. The tetraphenyl porphyrin could be considered as a fluorescent probe molecule. It was shown that if the experiments are performed at room temperature and the results analysed with a simple rate equations model, then a value for the Förster radius close to that predicted by basic Förster theory can be found. However, there are inadequacies to this approach. Firstly, it assumes that the excitons are point dipoles which is not realistic given their delocalisation over a conjugation segment. Secondly, this approach does not take exciton migration into account. Quantum chemical calculations by other workers have shown that the exciton delocalisation does not greatly affect the predicted value for the Förster radius. However, measurements here and elsewhere have shown that the energy transfer in these systems is temperature dependent. This indicates that exciton migration does contribute and must be taken into account.

A more complete analysis was developed following the model of Yokota and Tanimoto, who derived an expression to predict donor fluorescence decay in the presence of an acceptor when diffusion takes place. This expression was modified to

predict acceptor fluorescence in steady state such that it could be applied to the results here. At room temperature, an average migration distance of 20 +/- 2 nm was found. At low temperature, the migration distance was found to be 11 +/- 2 nm. It is suggested that this non-zero diffusion coefficient is most likely due to the polymer being excited above the localisation energy. Downhill migration to low energy segments may therefore still play a role. Another possibility is that it may be a representation of the fact that the exciton is delocalised over a polymer segment.

It is noted that recently reported results have shown that in these systems, exciton migration takes place within 10 ps, and at times greater than this the energy transfer becomes Förster-like. This is at odds with the model presented here, which assumes uniform diffusion throughout the exciton lifetime. However, the analysis here fits the data well. It is suggested that the model averages out the diffusion and recovers reasonably accurate values for the exciton diffusion length. Another possibility is that it is applicable in the low and room temperature limits, with 'diffusion' at low temperature being due to exciton delocalisation while at room temperature, thermally-activated hopping means the excitons do not become immobile.

This work is significant in that exciton migration plays a fundamental part in the properties of polyfluorene. For example, migration to defect sites in the polyfluorene can reduce its photoluminescence quantum yield. Efficient operation of solar cells requires excitons to migrate to a heterojunction so that they may dissociate, and obviously this must occur within their lifetime. The emission from polymer LEDs comes from the decay of excitons formed by injected holes and electrons. It is clear then that exciton migration is of great importance in practical applications.

Chapter 5 aimed to provide further information on the energy transfer processes in polyfluorene via fluorescence anisotropy measurements. Firstly, the refractive indices found by ellipsometry were used to calculate correction factors, taking into account the effects of refraction on polarized emission spectra. It was shown that refraction can greatly affect the fluorescence anisotropy of these spectra and that the effect depends significantly on excitation wavelength and incident angle. Fluorescence anisotropy is also affected by the angle to the film at which emission is measured, a result of dipoles

not emitting parallel to their axis. This was confirmed qualitatively in these measurements.

It was also shown that the excitation spectra of aligned polyfluorene films differs greatly depending on whether the films are excited with light polarized parallel or perpendicular to the chain orientation. It was suggested that this may be due to an additional, higher energy electronic transition with its dipole moment perpendicular to the chain backbone.

The fluorescence polarization anisotropy of unaligned films was shown to be independent of temperature. This indicates that even in the absence of thermally activated hopping, excitons migrate far enough to depolarize the fluorescence. Fluorescence anisotropy calculations made using TCSPC data and front-face emission found a fluorescence anisotropy of 0.12. Hence, this emission is not completely depolarized. These measurements were also used to suggest that some excitons are trapped immediately after excitation. This could be the origin of the residual anisotropy.

Finally, the possibility of achieving polarized fluorescence with a range of colours by doping aligned films with energy transfer molecules was investigated. Orange polarized luminescence from aligned films containing DCM could be observed. It was shown that the DCM molecules align themselves at least partially with the polymer chains. The polarization ratio was low and certainly not sufficient for use in a device. However, it demonstrated that this method has some potential. Other dopant molecules might be more suitable than DCM for this purpose. It might be expected that more elongated molecules would result in higher polarization ratios, as supported by the observation that polarized emission was observed from the linear DCM dopants but not from planar TPP dopants.

In summary, this thesis has described aspects of polyfluorene that are not only fundamental properties of the material, but also of importance in its practical applications.

Publication List

Publications resulting from the work contained in this thesis:

Chapter 3:

'A comparison of the optical constants of aligned and unaligned thin polyfluorene films'

B. P. Lyons and A. P. Monkman

Journal of Applied Physics **96** (9), 4735-4741 (2004)

(contribution: performed all experiments and wrote manuscript)

Chapter 4:

'Study of the energy transfer processes in polyfluorene doped with tetraphenyl porphyrin'

B. P. Lyons, K. S. Wong and A. P. Monkman

Journal of Chemical Physics **118** (10), 4707-4711 (2003)

(contribution: performed most of the experiments and wrote manuscript)

'The role of exciton diffusion in energy transfer between polyfluorene and tetraphenyl porphyrin'

B. P. Lyons and A. P. Monkman

Physical Review B **71**, 235201 (2005)

(contribution: performed all experiments and wrote manuscript)

Chapter 5:

'Orientation of dopant molecules in thin polyfluorene films'

B. P. Lyons and A. P. Monkman

SPIE Proceedings Vol. 5519 p235 (2004)

(contribution: performed all experiments and wrote manuscript)

Publications from work not contained in this thesis:

'Influence of molecular weight on the surface morphology of aligned, branched side-chain polyfluorene'
M. A. Knaapila et al.
Advanced Functional Materials **15** (9), 1517-1522 (2005)
(contribution: fabricated samples and performed spectroscopic measurements)

'Influence of molecular weight on the phase behaviour and structure formation of branched side-chain hairy-rod polyfluorene in bulk phase'
M. A. Knaapila et al.
Physical Review E **71**, 041802 (2005)
(contribution: fabricated samples and performed spectroscopic measurements)

'The influence of the molecular weight on the thermotropic alignment and self-organized structure formation of branched side chain hairy-rod polyfluorene in thin films'
M. A. Knaapila et al.
Macromolecules **38** (7), 2744-2753 (2005)
(contribution: fabricated samples and performed spectroscopic measurements)

'The influence of molecular weight on self-organization, uniaxial alignment and surface morphology of hairy-rodlike polyfluorene in thin films'
M. A. Knaapila et al.
Journal of Physical Chemistry B **108** (30), 10711-10720 (2004)
(contribution: fabricated samples and performed spectroscopic measurements)

'X-ray diffraction studies of multiple orientation in poly(9,9-bis(2-ethylhexyl)fluorene-2,7-diyl) thin films'
M. A. Knaapila et al.
Journal of Physical Chemistry B **107** (45), 12425-12430 (2003)
(contribution: fabricated samples and performed spectroscopic measurements)

'New pyrimidine- and fluorene-containing oligo(arylene)s: synthesis, crystal structures, optoelectronic properties and a theoretical study'
G. Hughes et al.
Organic and Biomolecular Chemistry **1** (17), 3069-3077 (2003)
(contribution: fabricated and tested organic light-emitting devices using novel material)

References

1 C. K. Chiang, C. R. Fincher, Y. W. Park, A. J. Heeger, H. Shirakawa, E. J. Louis, S. C. Gau, and A. G. Macdiarmid, Physical Review Letters **39** (17), 1098 (1977).

2 J. H. Burroughes, D. D. C. Bradley, A. R. Brown, R. N. Marks, K. Mackay, R. H. Friend, P. L. Burn, and A. B. Holmes, Nature **347**, 539 (1990).

3 H. A. Al Attar, A. P. Monkman, M. Tavasli, S. Bettington, and M. R. Bryce, Applied Physics Letters **86** (12), art. no. (2005).

4 S. Beaupre and M. Leclerc, Advanced Functional Materials **12** (3), 192 (2002).

5 Y. Cao, I. D. Parker, G. Yu, C. Zhang, and A. J. Heeger, Nature **397** (6718), 414 (1999).

6 X. Gong, D. Moses, A. J. Heeger, and S. Xiao, Journal of Physical Chemistry B **108** (25), 8601 (2004).

7 R. W. T. Higgins, A. P. Monkman, H. G. Nothofer, and U. Scherf, Applied Physics Letters **79** (6), 857 (2001).

8 A. Kambili and A. B. Walker, Physical Review B **6301** (1), art. no. (2001).

9 A. P. Kulkarni and S. A. Jenekhe, Macromolecules **36** (14), 5285 (2003).

10 L. C. Lin, H. F. Meng, J. T. Shy, S. F. Horng, L. S. Yu, C. H. Chen, H. H. Liaw, C. C. Huang, K. Y. Peng, and S. A. Chen, Physical Review Letters **90** (3), art. no. (2003).

11 T. Miteva, A. Meisel, W. Knoll, H. G. Nothofer, U. Scherf, D. C. Muller, K. Meerholz, A. Yasuda, and D. Neher, Advanced Materials **13** (8), 565 (2001).

12 L. C. Palilis, D. G. Lidzey, M. Redecker, D. D. C. Bradley, M. Inbasekaran, E. P. Woo, and W. W. Wu, Synthetic Metals **121** (1-3), 1729 (2001).

13 N. K. Patel, S. Cina, and J. H. Burroughes, Ieee Journal of Selected Topics in Quantum Electronics **8** (2), 346 (2002).

14 D. Braun and A. J. Heeger, Applied Physics Letters **58** (18), 1982 (1991).

15 W. U. Huynh, J. J. Dittmer, and A. P. Alivisatos, Science **295** (5564), 2425 (2002).

16 O. Inganäs, M. Svensson, F. Zhang, A. Gadisa, N. K. Persson, X. Wang, and M. R. Andersson, Applied Physics a-Materials Science & Processing **79** (1), 31 (2004).

17 R. Pacios, D. D. C. Bradley, J. Nelson, and C. J. Brabec, Synthetic Metals **137** (1-3), 1469 (2003).

18 N. K. Persson, H. Arwin, and O. Inganäs, Journal of Applied Physics **97** (3), art. no. (2005).

19 N. K. Persson, M. Schubert, and O. Inganäs, Solar Energy Materials and Solar Cells **83** (2-3), 169 (2004).

20 P. Peumans, A. Yakimov, and S. R. Forrest, Journal of Applied Physics **93** (7), 3693 (2003).

21 M. Svensson, F. Zhang, O. Inganäs, and M. R. Andersson, Synthetic Metals **135** (1-3), 137 (2003).

[22] M. Svensson, F. L. Zhang, S. C. Veenstra, W. J. H. Verhees, J. C. Hummelen, J. M. Kroon, O. Inganäs, and M. R. Andersson, Advanced Materials **15** (12), 988 (2003).

[23] X. J. Wang, E. Perzon, J. L. Delgado, P. de la Cruz, F. L. Zhang, F. Langa, M. Andersson, and O. Inganäs, Applied Physics Letters **85** (21), 5081 (2004).

[24] T. Yohannes, F. Zhang, A. Svensson, J. C. Hummelen, M. R. Andersson, and O. Inganäs, Thin Solid Films **449** (1-2), 152 (2004).

[25] F. L. Zhang, A. Gadisa, O. Inganäs, M. Svensson, and M. R. Andersson, Applied Physics Letters **84** (19), 3906 (2004).

[26] M. Ahles, A. Hepp, R. Schmechel, and H. von Seggern, Applied Physics Letters **84** (3), 428 (2004).

[27] A. Salleo and R. A. Street, Journal of Applied Physics **94** (1), 471 (2003).

[28] H. Sirringhaus, N. Tessler, and R. H. Friend, Science **280** (5370), 1741 (1998).

[29] H. Sirringhaus, R. J. Wilson, R. H. Friend, M. Inbasekaran, W. Wu, E. P. Woo, M. Grell, and D. D. C. Bradley, Applied Physics Letters **77** (3), 406 (2000).

[30] R. A. Street, A. Salleo, M. Chabinyc, and K. Paul, Journal of Non-Crystalline Solids **338-40**, 607 (2004).

[31] V. G. Kozlov, V. Bulovic, P. E. Burrows, M. Baldo, V. B. Khalfin, G. Parthasarathy, S. R. Forrest, Y. You, and M. E. Thompson, Journal of Applied Physics **84** (8), 4096 (1998).

[32] V. G. Kozlov, G. Parthasarathy, P. E. Burrows, S. R. Forrest, Y. You, and M. E. Thompson, Applied Physics Letters **72** (2), 144 (1998).

[33] M. Theander, T. Granlund, D. M. Johanson, A. Ruseckas, V. Sundstrom, M. R. Andersson, and O. Inganäs, Advanced Materials **13** (5), 323 (2001).

[34] T. Virgili, D. G. Lidzey, M. Grell, D. D. C. Bradley, S. Stagira, M. Zavelani-Rossi, and S. De Silvestri, Applied Physics Letters **80** (22), 4088 (2002).

[35] V. N. Bliznyuk, S. A. Carter, J. C. Scott, G. Klarner, R. D. Miller, and D. C. Miller, Macromolecules **32** (2), 361 (1999).

[36] A. S. Dhoot and N. C. Greenham, Advanced Materials **14** (24), 1834 (2002).

[37] M. K. Fung, S. L. Lai, S. W. Tong, M. Y. Chan, C. S. Lee, S. T. Lee, W. W. Wu, M. Inbasekaran, and J. J. O'Brien, Applied Physics Letters **81** (8), 1497 (2002).

[38] S. Sinha, C. Rothe, R. Guntner, U. Scherf, and A. P. Monkman, Physical Review Letters **90** (12), art. no. (2003).

[39] M. J. Banach, R. H. Friend, and H. Sirringhaus, Macromolecules **37**, 6079 (2004).

[40] M. J. Banach, R. H. Friend, and H. Sirringhaus, Macromolecules **36** (8), 2838 (2003).

[41] M. Grell, W. Knoll, D. Lupo, A. Meisel, T. Miteva, D. Neher, H. G. Nothofer, U. Scherf, and A. Yasuda, Advanced Materials **11** (8), 671 (1999).

[42] M. Knaapila, K. Kisko, B. P. Lyons, R. Stepanyan, J. P. Foreman, O. H. Seeck, U. Vainio, L. O. Pålsson, R. Serimaa, M. Torkkeli, and A. P. Monkman, Journal of Physical Chemistry B **108** (30), 10711 (2004).

[43] M. Knaapila, R. Stepanyan, B. P. Lyons, M. Torkkeli, T. P. A. Hase, R. Serimaa, R. Guentner, O. H. Seeck, U. Scherf, and A. P. Monkman, Macromolecules **38**, 2744 (2005).

[44] B. P. Lyons and A. P. Monkman, Journal of Applied Physics **96** (9), 4735 (2004).

[45] T. Miteva, A. Meisel, M. Grell, H. G. Nothofer, D. Lupo, A. Yasuda, W. Knoll, L. Kloppenburg, U. H. F. Bunz, U. Scherf, and D. Neher, Synthetic Metals **111**, 173 (2000).

[46] K. S. Whitehead, M. Grell, D. D. C. Bradley, M. Jandke, and P. Strohriegl, Applied Physics Letters **76** (20), 2946 (2000).

[47] A. L. T. Khan, M. J. Banach, and A. Kohler, Synthetic Metals **139** (3), 905 (2003).

[48] A. L. T. Khan, P. Sreearunothai, L. M. Herz, M. J. Banach, and A. Kohler, Physical Review B **69** (8), art. no. (2004).

[49] R. Schroeder, B. Ullrich, W. Graupner, and U. Scherf, Journal of Physics-Condensed Matter **13** (16), L313 (2001).

[50] C. Rothe and A. P. Monkman, Physical Review B **68** (7), 075208 (2003).

[51] S. C. J. Meskers, J. Hubner, M. Oestreich, and H. Bassler, Journal of Physical Chemistry B **105** (38), 9139 (2001).

[52] S. C. J. Meskers, J. Hubner, M. Oestreich, and H. Bassler, Chemical Physics Letters **339** (3-4), 223 (2001).

[53] A. P. Sutton, *Electronic Structure of Materials*, 1st ed. (Clarendon Press, Oxford, 1996).

[54] C. H. J. Wells, *Introduction to Molecular Photochemistry*, 1st ed. (Chapman and Hall, London, 1972).

[55] J. B. Birks, *Photophysics of Aromatic Molecules*, 1st ed. (Wiley-Interscience, 1970).

[56] J. R. Lakowicz, *Principles of Fluorescence Spectroscopy*, 2nd ed. (Kluwer Academic/Plenum Publishers, 1999).

[57] N. C. Greenham and D. Richards, *Optoelectronics Lecture Course*. (Natural Sciences Tripos; Part III Physics, University of Cambridge, 2000).

[58] O. Narwark, S. C. J. Meskers, R. Peetz, E. Thorn-Csanyi, and H. Bassler, Chemical Physics **294** (1), 1 (2003).

[59] *Primary Photoexcitations In Conjugated Polymers: Molecular Exciton versus Semiconductor Band Model*, edited by N. S. Sariciftci (World Scientific, 1997).

[60] W. P. Su, J. R. Schrieffer, and A. J. Heeger, Physical Review B **22** (4), 2099 (1980).

[61] W. P. Su, J. R. Schrieffer, and A. J. Heeger, Physical Review Letters **42** (25), 1698 (1979).

[62] C. H. Lee, G. Yu, D. Moses, and A. J. Heeger, Physical Review B **49** (4), 2396 (1994).

[63] N. S. Sariciftci, L. Smilowitz, A. J. Heeger, and F. Wudl, Science **258** (5087), 1474 (1992).

[64] J. M. Leng, S. Jeglinski, X. Wei, R. E. Benner, Z. V. Vardeny, F. Guo, and S. Mazumdar, Physical Review Letters **72** (1), 156 (1994).

[65] P. G. Dacosta and E. M. Conwell, Physical Review B **48** (3), 1993 (1993).

[66] H. Bassler, M. Gailberger, R. F. Mahrt, J. M. Oberski, and G. Weiser, Synthetic Metals **49** (1-3), 341 (1992).

[67] H. Bassler, in *Primary Photoexcitations In Conjugated Polymers: Molecular Exciton versus Semiconductor Band Model*, edited by N. S. Sariciftci (World Scientific, 1997), pp. 51.

[68] S. Kishino, Y. Ueno, K. Ochiai, M. Rikukawa, K. Sanui, T. Kobayashi, H. Kunugita, and K. Ema, Physical Review B **58** (20), R13430 (1998).

[69] T. L. Porter, D. Minore, and D. Zhang, Journal of Physical Chemistry **99** (35), 13213 (1995).

[70] S. N. Yaliraki and R. J. Silbey, Journal of Chemical Physics **104** (4), 1245 (1996).

[71] W. J. D. Beenken and T. Pullerits, Journal of Physical Chemistry B **108** (20), 6164 (2004).

[72] G. Fytas, H. G. Nothofer, U. Scherf, D. Vlassopoulos, and G. Meier, Macromolecules **35** (2), 481 (2002).

[73] G. Klaerner and R. D. Miller, Macromolecules **31** (6), 2007 (1998).

[74] H. Meier, U. Stalmach, and H. Kolshorn, Acta Polymerica **48** (9), 379 (1997).

[75] Z. G. Soos, M. H. Hennessy, and D. Mukhopadhyay, in *Primary Photoexcitations in Conjugated Polymers: Molecular Exciton versus Semiconductor Band Model*, edited by N. S. Sariciftci (World Scientific, 1997), pp. 1.

[76] M. Pope and C. E. Swenberg, *Electronic Processes in Organic Crystals and Polymers*, 2nd ed. (Oxford Science Publications, 2000).

[77] H. A. Mizes and E. M. Conwell, Physical Review Letters **70** (10), 1505 (1993).

[78] T. Virgili, G. Cerullo, L. Luer, G. Lanzani, C. Gadermaier, and D. D. C. Bradley, Physical Review Letters **90** (24) (2003).

[79] C. Zenz, W. Graupner, S. Tasch, G. Leising, K. Mullen, and U. Scherf, Applied Physics Letters **71** (18), 2566 (1997).

[80] J. Sturm, S. Tasch, A. Niko, G. Leising, E. Toussaere, J. Zyss, T. C. Kowalczyk, K. D. Singer, U. Scherf, and J. Huber, Thin Solid Films **298** (1-2), 138 (1997).

[81] K. Petritsch, W. Graupner, G. Leising, and U. Scherf, Synthetic Metals **84** (1-3), 625 (1997).

[82] A. J. Heeger, in *Primary Photoexcitations In Conjugated Polymers: Molecular Exciton versus Semiconductor Band Model*, edited by N. S. Sariciftci (World Scientific, 1997), pp. 20.

[83] R. Jankowiak and H. Bassler, Chemical Physics **79** (1), 57 (1983).

[84] G. Schonherr, R. Eiermann, H. Bassler, and M. Silver, Chemical Physics **52** (3), 287 (1980).

[85] R. Kersting, U. Lemmer, R. F. Mahrt, K. Leo, H. Kurz, H. Bassler, and E. O. Gobel, Physical Review Letters **70** (24), 3820 (1993).

[86] G. R. Hayes, I. D. W. Samuel, and R. T. Phillips, Physical Review B **52** (16), 569 (1995).

[87] L. M. Herz, C. Silva, A. C. Grimsdale, K. Mullen, and R. T. Phillips, Physical Review B **70**, 165207 (2004).

[88] R. Kersting, B. Mollay, M. Rusch, J. Wenisch, G. Leising, and H. F. Kauffmann, Journal of Chemical Physics **106** (7), 2850 (1997).

[89] D. Beljonne, Z. Shuai, J. Cornil, J. P. Calbert, and J. L. Bredas, Journal of Photochemistry and Photobiology a-Chemistry **144** (1), 57 (2001).

90 A. Kohler and J. Wilson, Organic Electronics **4** (2-3), 179 (2003).

91 Z. Shuai, D. Beljonne, R. J. Silbey, and J. L. Bredas, Physical Review Letters **84** (1), 131 (2000).

92 M. Wohlgenannt, X. M. Jiang, and Z. V. Vardeny, Physica B-Condensed Matter **338** (1-4), 318 (2003).

93 C. Yang, Z. V. Vardeny, A. Kohler, M. Wohlgenannt, M. K. Al-Suti, and M. S. Khan, Physical Review B **70** (24), art. no. (2004).

94 D. F. O'Brien, M. A. Baldo, M. E. Thompson, and S. R. Forrest, Applied Physics Letters **74** (3), 442 (1999).

95 M. A. Baldo, D. F. O'Brien, Y. You, A. Shoustikov, S. Sibley, M. E. Thompson, and S. R. Forrest, Nature **395** (6698), 151 (1998).

96 M. A. Baldo, M. E. Thompson, and S. R. Forrest, Nature **403** (6771), 750 (2000).

97 C. Adachi, M. A. Baldo, S. R. Forrest, S. Lamansky, M. E. Thompson, and R. C. Kwong, Applied Physics Letters **78** (11), 1622 (2001).

98 V. Cleave, G. Yahioglu, P. Le Barny, R. H. Friend, and N. Tessler, Advanced Materials **11** (4), 285 (1999).

99 M. Ariu, D. G. Lidzey, M. Sims, A. J. Cadby, P. A. Lane, and D. D. C. Bradley, Journal of Physics-Condensed Matter **14** (42), 9975 (2002).

100 A. J. Cadby, P. A. Lane, H. Mellor, S. J. Martin, M. Grell, C. Giebeler, D. D. C. Bradley, M. Wohlgenannt, C. An, and Z. V. Vardeny, Physical Review B **62** (23), 15604 (2000).

101 Y. Ohmori, M. Uchida, K. Muro, and K. Yoshino, Japanese Journal of Applied Physics **30**, 1941 (1991).

102 A. W. Grice, D. D. C. Bradley, M. T. Bernius, M. Inbasekaran, W. W. Wu, and E. P. Woo, Applied Physics Letters **73** (5), 629 (1998).

103 Q. B. Pei and Y. Yang, Journal of the American Chemical Society **118** (31), 7416 (1996).

104 W. L. Yu, J. Pei, W. Huang, and A. J. Heeger, Advanced Materials **12** (11), 828 (2000).

105 K. H. Weinfurtner, H. Fujikawa, S. Tokito, and Y. Taga, Applied Physics Letters **76** (18), 2502 (2000).

106 D. Bradley, Current Opinion In Solid State & Materials Science **1** (6), 789 (1996).

107 G. Vamvounis and S. Holdcroft, Advanced Materials **16** (8), 716 (2004).

108 Q. Peng, Z. Y. Lu, Y. Huang, M. G. Xie, S. H. Han, J. B. Peng, and Y. Cao, Macromolecules **37** (2), 260 (2004).

109 Q. Peng, Y. Huang, Z. Y. Lu, S. Y. Qin, M. G. Xie, W. X. Gao, J. B. Peng, and Y. Cao, Chinese Journal of Chemistry **22** (6), 599 (2004).

110 N. S. Cho, D. H. Hwang, B. J. Jung, E. Lim, J. Lee, and H. K. Shim, Macromolecules **37** (14), 5265 (2004).

111 A. M. Assaka, P. C. Rodrigues, A. R. M. de Oliveira, L. M. Ding, H. Bin, F. E. Karasz, and L. Akcelrud, Polymer **45** (21), 7071 (2004).

112 M. Tammer, R. W. T. Higgins, and A. P. Monkman, Journal of Applied Physics **91** (7), 4010 (2002).

[113] B. P. Lyons, K. S. Wong, and A. P. Monkman, Journal of Chemical Physics **118** (10), 4707 (2003).

[114] T. Virgili, D. G. Lidzey, and D. D. C. Bradley, Synthetic Metals **111**, 203 (2000).

[115] P. E. Keivanidis, S. Baluschev, T. Miteva, G. Nelles, U. Scherf, A. Yasuda, and G. Wegner, Advanced Materials **15** (24), 2095 (2003).

[116] G. L. Tu, Q. G. Zhou, Y. X. Cheng, L. X. Wang, D. G. Ma, X. B. Jing, and F. S. Wang, Applied Physics Letters **85** (12), 2172 (2004).

[117] C. Ego, D. Marsitzky, S. Becker, J. Y. Zhang, A. C. Grimsdale, K. Mullen, J. D. MacKenzie, C. Silva, and R. H. Friend, Journal of the American Chemical Society **125** (2), 437 (2003).

[118] A. J. Sandee, C. K. Williams, N. R. Evans, J. E. Davies, C. E. Boothby, A. Kohler, R. H. Friend, and A. B. Holmes, Journal of the American Chemical Society **126** (22), 7041 (2004).

[119] W. L. Yu, B. Liu, J. Pei, G. Zeng, and W. Huang, Chinese Journal of Polymer Science **19** (6), 603 (2001).

[120] J. H. Kim, P. Herguth, M. S. Kang, A. K. Y. Jen, Y. H. Tseng, and C. F. Shu, Applied Physics Letters **85** (7), 1116 (2004).

[121] G. K. Ho, H. F. Meng, S. C. Lin, S. F. Horng, C. S. Hsu, L. C. Chen, and S. M. Chang, Applied Physics Letters **85** (20), 4576 (2004).

[122] D. Vak, C. Chun, C. L. Lee, J. J. Kim, and D. Y. Kim, Journal of Materials Chemistry **14** (8), 1342 (2004).

[123] F. I. Wu, R. Dodda, K. Jakka, J. H. Huang, C. S. Hsu, and C. F. Shu, Polymer **45** (12), 4257 (2004).

[124] F. I. Wu, R. Dodda, D. S. Reddy, and C. F. Shu, Journal of Materials Chemistry **12** (10), 2893 (2002).

[125] J. Nelson, Current Opinion in Solid State & Materials Science **6** (1), 87 (2002).

[126] K. Yoshino, X. H. Yin, T. Akashi, K. Yoshimoto, S. Morita, and A. A. Zakhidov, Molecular Crystals and Liquid Crystals Science and Technology Section a-Molecular Crystals and Liquid Crystals **255**, 197 (1994).

[127] T. Kietzke, D. Neher, M. Kumke, R. Montenegro, K. Landfester, and U. Scherf, Macromolecules **37** (13), 4882 (2004).

[128] D. M. Russell, A. C. Arias, R. H. Friend, C. Silva, C. Ego, A. C. Grimsdale, and K. Mullen, Applied Physics Letters **80** (12), 2204 (2002).

[129] H. J. Snaith, A. C. Arias, A. C. Morteani, C. Silva, and R. H. Friend, Nano Letters **2** (12), 1353 (2002).

[130] H. J. Snaith, N. C. Greenham, and R. H. Friend, Advanced Materials **16** (18), 1640 (2004).

[131] T. Kietzke, D. Neher, K. Landfester, R. Montenegro, R. Guntner, and U. Scherf, Nature Materials **2** (6), 408 (2003).

[132] H. J. Snaith and R. H. Friend, Synthetic Metals **147** (1-3), 105 (2004).

[133] M. Grell, D. D. C. Bradley, M. Inbasekaran, and E. P. Woo, Advanced Materials **9** (10), 798 (1997).

[134] G. Lieser, M. Oda, T. Miteva, A. Meisel, H. G. Nothofer, U. Scherf, and D. Neher, Macromolecules **33** (12), 4490 (2000).

[135] M. Knaapila, B. P. Lyons, K. Kisko, J. P. Foreman, U. Vainio, M. Mihaylova, O. H. Seeck, L. O. Pålsson, R. Serimaa, M. Torkkeli, and A. P. Monkman, Journal of Physical Chemistry B **107** (45), 12425 (2003).

[136] J. I. Lee, G. Klaerner, and R. D. Miller, Synthetic Metals **101** (1-3), 126 (1999).

[137] M. Gaal, E. J. W. List, and U. Scherf, Macromolecules **36** (11), 4236 (2003).

[138] E. Zojer, A. Pogantsch, E. Hennebicq, D. Beljonne, J. L. Bredas, P. S. de Freitas, U. Scherf, and E. J. W. List, Journal of Chemical Physics **117** (14), 6794 (2002).

[139] E. J. W. List, R. Guentner, P. S. de Freitas, and U. Scherf, Advanced Materials **14** (5), 374 (2002).

[140] S. Panozzo, J. C. Vial, Y. Kervella, and O. Stephan, Journal of Applied Physics **92** (7), 3495 (2002).

[141] M. Sims, D. D. C. Bradley, M. Ariu, M. Koeberg, A. Asimakis, M. Grell, and D. G. Lidzey, Advanced Functional Materials **14** (8), 765 (2004).

[142] S. I. Hintschich, C. Rothe, S. Sinha, A. P. Monkman, P. S. de Freitas, and U. Scherf, Journal of Chemical Physics **119** (22), 12017 (2003).

[143] X. Gong, D. Moses, A. J. Heeger, and S. Xiao, Synthetic Metals **141** (1-2), 17 (2004).

[144] M. Fukuda, K. Sawada, and K. Yoshino, Journal of Polymer Science Part a-Polymer Chemistry **31** (10), 2465 (1993).

[145] W. Flack, D. Soong, A. Bell, and D. Hess, Journal of Applied Physics **56**, 1199 (1984).

[146] G. Striker, in *Deconvolution and Reconvolution of Analytical Systems*, edited by M. Bouchy (University Press, Nancy, 1982).

[147] M. Tammer and A. P. Monkman, Advanced Materials **14** (3), 210 (2002).

[148] N. C. Greenham and C. M. Ramsdale, Advanced Materials **14** (3), 212 (2002).

[149] J. A. Woollam, in *Wiley Encyclopedia of Electrical and Electronics Engineering*, edited by J. G. Weber (Wiley, New York, 2000).

[150] R. A. Craig, Journal of the Optical Society of America A - Optics Image Science and Vision **4** (6), 1092 (1987).

[151] C. Fluerara, M. Gartner, O. Buiu, R. Radoi, I. Cernica, P. Imperia, and S. Schrader, Surface Science **482**, 448 (2001).

[152] N. A. J. M. van Aerle, M. Barmentlo, and R. W. J. Hollering, Journal of Applied Physics **74** (5), 3111 (1993).

[153] D. McBranch, I. H. Campbell, D. L. Smith, and J. P. Ferraris, Applied Physics Letters **66** (10), 1175 (1995).

[154] C. W. Y. Law, K. S. Wong, Z. Yang, L. E. Horsburgh, and A. P. Monkman, Applied Physics Letters **76** (11), 1416 (2000).

[155] A. Zen, D. Neher, C. Bauer, U. Asawapirom, U. Scherf, R. Hagen, S. Kostromine, and R. F. Mahrt, Applied Physics Letters **80** (25), 4699 (2002).

[156] T. Forster, Discuss. Faraday Soc. **27**, 7 (1959).

[157] U. Lemmer, A. Ochse, M. Deussen, R. F. Mahrt, E. O. Gobel, H. Bassler, P. H. Bolivar, G. Wegmann, and H. Kurz, Synthetic Metals **78** (3), 289 (1996).

[158] G. Cerullo, S. Stagira, M. Zavelani-Rossi, S. De Silvestri, T. Virgili, D. G. Lidzey, and D. D. C. Bradley, Chemical Physics Letters **335** (1-2), 27 (2001).

159 E. J. W. List, C. Creely, G. Leising, N. Schulte, A. D. Schluter, U. Scherf, K. Mullen, and W. Graupner, Chemical Physics Letters **325**, 132 (2000).

160 K. F. Wong, B. Bagchi, and P. J. Rossky, Journal of Physical Chemistry A **108** (27), 5752 (2004).

161 D. Beljonne, G. Pourtois, C. Silva, E. Hennebicq, L. M. Herz, R. H. Friend, G. D. Scholes, S. Setayesh, K. Mullen, and J. L. Bredas, Proceedings of the National Academy of Sciences of the United States of America **99** (17), 10982 (2002).

162 L. O. Pålsson and A. P. Monkman, Advanced Materials **14** (10), 757 (2002).

163 M. Yokota and O. Tanimoto, Journal of the Physical Society of Japan **22** (3), 779 (1967).

164 G. A. Baker Jr., in *Advances in Theoretical Physics*, edited by K. A. Brueckner (Academic Press, New York, 1965), Vol. 1, pp. 1.

165 K. B. Eisenthal and S. Siegel, Journal of Chemical Physics **41** (3), 652 (1964).

166 U. Gösele, M. Hauser, U. K. A. Klein, and R. Frey, Chemical Physics Letters **34** (3), 519 (1975).

167 M. Yan, L. J. Rothberg, F. Papadimitrakopoulos, M. E. Galvin, and T. M. Miller, Physical Review Letters **73** (5), 744 (1994).

168 J. Sperling, C. Benesch, L. Kuna, R. Kauffmann, and F. Milota, Synthetic Metals **143** (3), 315 (2004).

169 F. L. Pedrotti and L. S. Pedrotti, *Introduction to Optics*, 2nd ed. (Prentice-Hall International, Inc., 1993).

170 E. W. Thulstrup and J. Michl, *Elementary Polarization Spectroscopy*, 1st ed. (VCH Publishers, 1989).

171 H. M. Liem, P. Etchegoin, K. S. Whitehead, and D. D. C. Bradley, Advanced Functional Materials **13** (1), 66 (2003).

172 B. Schartel, V. Wachtendorf, M. Grell, D. D. C. Bradley, and M. Hennecke, Physical Review B **60** (1), 277 (1999).

173 T. Damerau and M. Hennecke, Journal of Chemical Physics **103** (14), 6232 (1995).

174 C. R. Desper and I. Kimura, Journal of Applied Physics **38** (11), 4225 (1967).

175 D. I. Bower, Journal of Polymer science: Polymer Physics Edition **19**, 93 (1981).

176 Personal communications with F. B. Dias.

177 H. L. Vaughan, F. B. Dias, and A. P. Monkman, Journal of Chemical Physics **122**, 014902 (2005).